IN SITU POLARIZATION MODULATION INFRARED REFLECTION ABSORPTION SPECTROSCOPIC AND KINETIC INVESTIGATIONS OF HETEROGENEOUS CATALYTIC SYSTEMS

A Dissertation

by

YUN CAI

Submitted to the Office of Graduate Studies of
Texas A&M University
in partial fulfillment of the requirements for the degree of

DOCTOR OF PHILOSPHY

December 2008

Major Subject: Chemistry

IN SITU POLARIZATION MODULATION INFRARED REFLECTION ABSORPTION SPECTROSCOPIC AND KINETIC INVESTIGATIONS OF HETEROGENEOUS CATALYTIC SYSTEMS

A Dissertation

by

YUN CAI

Submitted to the Office of Graduate Studies of
Texas A&M University
in partial fulfillment of the requirements for the degree of

DOCTOR OF PHILOSOPHY

Approved by:

Chair of Committee,	D. Wayne Goodman
Committee Members,	Michael P. Rosynek
	Manuel P. Soriaga
	Yue Kuo
Head of Department,	David H. Russell

December 2008

Major Subject: Chemistry

ABSTRACT

In Situ Polarization Modulation Infrared Reflection Absorption Spectroscopic and Kinetic Investigations of Heterogeneous Catalytic Reactions. (December 2008)

Yun Cai, B.S.; M.S., Xiamen University, China

Chair of Advisory Committee: Dr. D. Wayne Goodman

A molecular-level understanding of a heterogeneous catalytic reaction is the key goal of heterogeneous catalysis. A surface science approach enables the realization of this goal. However, the working conditions (ultrahigh vacuum (UHV) conditions) of traditional surface science techniques restrict the investigations of heterogeneous catalysis system under industrial working conditions (atmospheric pressures). Polarization Modulation Infrared Reflection-Absorption Spectroscopy (PM-IRAS) can be operated in both UHV and atmospheric pressure conditions with a wide temperature span while providing high resolution (4 cm^{-1} is used in this dissertation) spectra. In this dissertation, PM-IRAS has been employed as a major technique to: 1) obtain both electronic and chemical information of catalysts from UHV to elevated pressure conditions; 2) explore reaction mechanisms by in situ monitoring surface species with concurrent kinetic measurements.

In this dissertation, NO adsorption and dissociation on Rh(111) have been studied. Our PM-IRAS spectra show a transition of NO adsorption on three-fold hollow sites to atop sites occurs at low temperatures (<275 K). NO dissociation is found to

account for this transition. The results indicated the dissociation of NO occurs well below the temperature previously reported.

Characterizations of highly catalytically active Au films have also been carried out. Electronic and chemical properties of (1 × 1)- and (1 × 3)-Au/TiO_x/Mo(112) films are investigated by PM-IRAS using CO as a probe molecule. The Au overlayers are found to be electron-rich and to have significantly different electronic properties compared with bulk Au. The exceptionally high catalytic activity of the Au bilayer structure is related to its unique electronic properties.

CO oxidation reactions on Rh, Pd, and Pt single crystals are explored from low CO pressures under steady-state conditions (less than 1×10^{-4} Torr) to high pressures (0.01-10 Torr) at various gaseous reactant compositions. Surface CO species are probed with in situ PM-IRAS to elucidate the surface phases under reaction conditions. These experimental results are used to correlate reaction kinetics and surface reactant species. It is evident that there is a continuum over the pressure range studied with respect to the reaction mechanism. The most active phase has been shown to be an oxygen-dominant surface. The formation of a subsurface oxygen layer is found to deactivate the reaction.

DEDICATION

To my parents, Jinzhao and Zhenyou. Thanks.

ACKNOWLEDGEMENTS

I would like to take this opportunity to express my deepest gratitude to a large group of people who have given me continuous support during my doctoral work and who have made this period of my life become a great experience. First of all, I would like to thank my advisor, Dr. D. Wayne Goodman, for providing a high-quality scientific environment, for his outstanding guidance and for his support and encouragement. I have been greatly inspired by his infectious enthusiasm and indefatigable passion for science. I am also grateful to my committee members, Dr. Michael P. Rosynek, Manuel P. Soriaga, and Dr. Yue Kuo, for their advice and support.

I also would like to thank all my group members, both past and present with whom I had the privilege to work with in the past five years. In particular, I would like to express my sincere appreciation to Dr. Mingshu Chen, a XMU alumnus and project partner, who has been a friend and mentor by giving me numerous valuable advice, helping me solve various technical problems, and sharing his scientific experience and vision; Dr. Emrah Ozensoy, my first project partner, who has opened the door of surface science for me and who helped me learn and understand various surface science techniques on PM-IRAS chamber with great patience; Dr. Qinglin Guo, whose big smile always reminds me to keep a positive attitude towards life, for generously sharing his experience both scientifically and personally; Dr. Feng Gao, an eight-month project partner, for the fruitful discussion and the constructive suggestions in scientific skills and writing; Dr. William T. Wallace, a seven-month project partner, for his great

collaboration and help in the paper writing; Dr. Sungsik Lee for his help in the LabVIEW programs writing and the modification of TPD box; Stephanus Axnanda for sharing delicious food and beautiful music; Kerrie Gath for inviting me to join WISE and having some cheerful girl talk; Amy Liu for her secretarial assistance and warm support. I would like to thank all the group members for their help and suggestions and for sharing happy moments together: beer times in Fitzwilly, afternoon bbqs in Edelweiss Park, buffet lunches in China King, and happy dinners in Buffalo Wild Wings, Cheddars, Pyro, etc.

In addition, I would like to thank a spectacular craftsman, Tony Montalbano, for not only helping me solve different instrumental problems, but for instructing me on the fundamentals of machining and the instrumental designs.

A special thanks goes to my parents for their endless patience and love and for their unconditional support and encouragement to pursue my interests.

Finally, I would like to thank my boyfriend, Yongxin, who has been a continuous support since we met and who has made my life much more joyful. I am also grateful to other friends who have made my stay in College Station enjoyable and given me pleasant memories that I will carry with me through my life.

TABLE OF CONTENTS

CHAPTER Page

LIST OF FIGURES

FIGURE Page

FIGURE Page

FIGURE Page

CHAPTER I

INTRODUCTION

Surface Science Studies on Heterogeneous Catalytic Systems

The primary goal in heterogeneous catalysis research is to obtain a molecular-level understanding of reaction mechanisms on catalysts via correlation between the structure and the activity/selectivity of the catalysts under reaction conditions. However, industrial high surface area supported catalysts are typically not suitable for molecular-level characterizations by conventional surface spectroscopic techniques. This is due to the complex nature of the structure, composition, particle size distribution, porosity, and impurities introduced from the wet-chemical preparation processes. Consequently, knowledge about the microscopic elementary processes of heterogeneous catalytic reactions is very limited. Because of the lack of molecular-level understanding, the design of industrial catalysts is still largely based on trial and error. To improve industrial catalyst designs, researchers study catalytic systems of reduced complexity in order to gain a more detailed understanding of the catalytic processes. One approach to reducing the complexity of the real catalytic systems and obtaining the fundamental understanding of catalytic processes is to use well-defined single crystals as model catalysts and to conduct reactions under clean, ultrahigh vacuum (UHV) conditions [1]. This methodology is often referred to as the *surface science approach*.

This dissertation follows the style and format of Surface Science.

In principle, it is possible for the enormously complicated catalytic processes on high surface area catalysts to be greatly simplified. The atomic-scale investigations of catalytic processes thus become approachable. Indeed, the development of surface science [2] has provided an enormous database on the fundamental understanding of heterogeneous catalysis, including adsorption, diffusion, dissociation and reaction of reactants, formation and desorption of products, etc.

In some cases, the knowledge obtained via surface science studies can be extrapolated directly to industrial reaction conditions. For example, kinetic investigations of CO oxidation on Rh, Pt, and Ir single crystals have shown that the reaction at high pressures follows the same rate law as that at low pressures (Fig. 1) [3]. Based on measurements at UHV conditions, density functional theory (DFT) calculations of ammonia synthesis at high pressures and temperatures have achieved an excellent agreement with the measurements on industrial Fe and Ru-based catalysts [4, 5]. In many other cases, however, the catalytic activity exhibits dramatic differences in UHV conditions and at atmospheric pressures. A prominent example is the CO oxidation on Ru catalysts. Ru catalysts display the lowest activity among platinum group metals toward CO oxidation reaction at UHV conditions, while showing the highest activity at elevated pressures in stoichiometric gas composition and relatively low temperatures [6]. The oxygen layer formed with the presence of high pressure oxygen, which cannot be formed under low pressure conditions, is believed to account for the dramatic increase in activity of Ru catalysts [6].

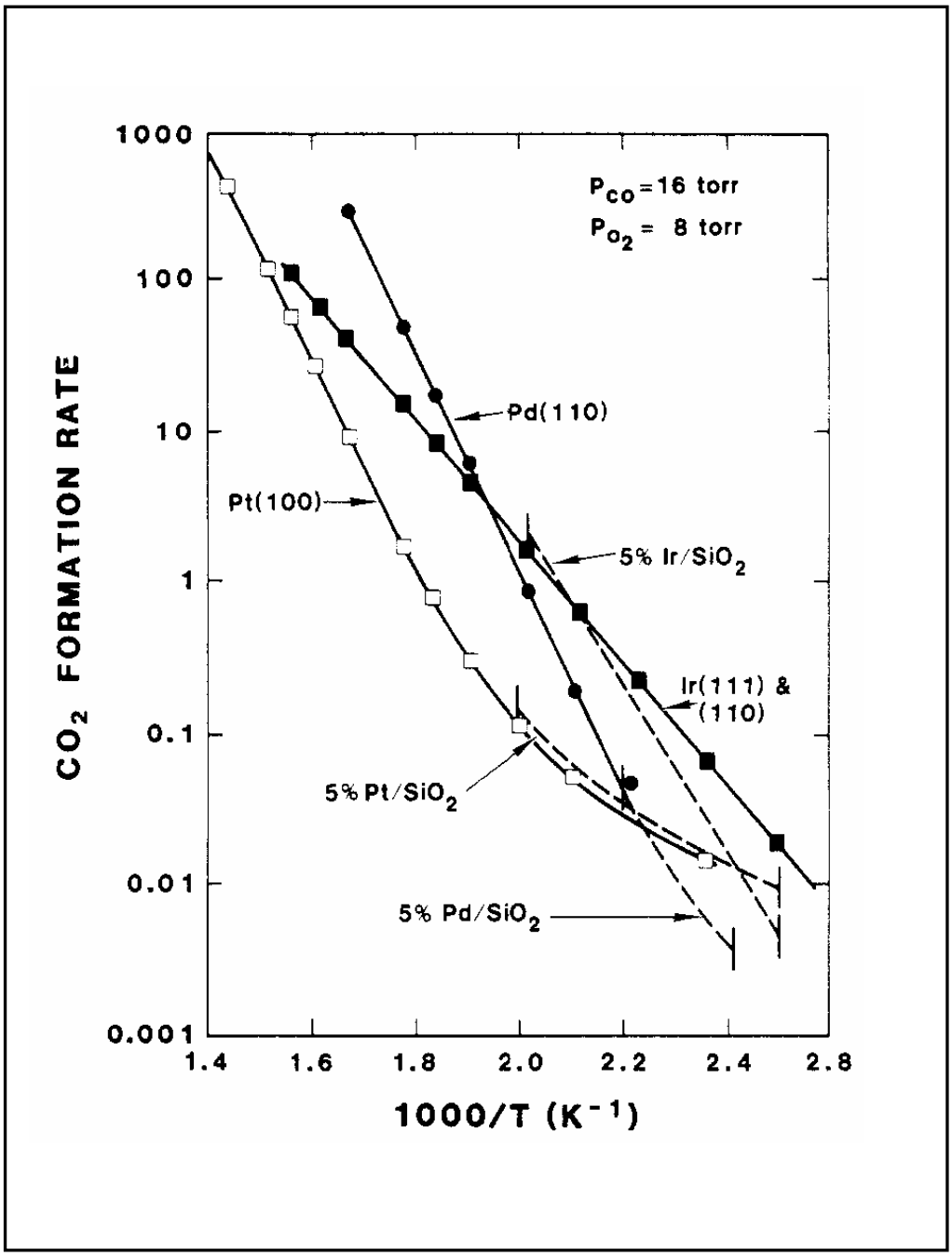

Fig. 1. CO_2 formation rate as a function of inverse temperature for single crystal and supported catalysts [3].

The differences in the typical reaction conditions between UHV studies and industrial operations invoke concerns about the so-called *pressure* and *material gaps*. The pressure gap refers to a more than ten orders of magnitude pressure difference between typical UHV-based experiments and industrial catalytic reactions. The materials gap refers to the difference between well-defined single crystals and highly-dispersed supported catalysts.

The most straightforward approach to "bridge" these gaps, especially the pressure gap, is to use surface sensitive techniques that are applicable both at UHV conditions and high pressures. During the past decades, several *in situ* surface characterization tools applicable at high pressures and temperatures have been developed successfully. Atom-resolved environmental transmission electron microscopy (ETEM) is currently capable of operating at 20 mbar [7-9]; modern X-ray synchrotron sources are powerful enough to provide beams that enable X-ray diffraction experiments (XRD) to monitor surface structures at pressures up to several bar [10]; X-ray photoemission spectroscopy (XPS) can work at pressures in the millibar range using differential pumping [11]; and high pressure scanning tunneling microscopy (HP-STM), first reported by Somorjai [12] and Besenbacher [13], can also operate at atmospheric pressures. Two optical-based techniques, namely sum frequency generation (SFG) vibrational spectroscopy [14-17] and polarization modulation infrared reflection and adsorption spectroscopy (PM-IRAS) [17-19] can be applied from UHV to atmospheric pressures, and are only surface sensitive.

In this dissertation, the power of PM-IRAS to investigate heterogeneous catalysis systems under both UHV and elevated pressure conditions is demonstrated. In particular, catalytic CO oxidation is investigated on Rh, Pd, and Pt single crystals over wide temperature and pressure ranges.

Catalytic CO Oxidation on Pt-group Metals

Catalytic oxidation of carbon monoxide on platinum group metals is ideal for fundamental studies because it comprises all basic steps of a heterogeneously catalyzed reaction, including adsorption (both associative and dissociative) of reactants, diffusion (migration) of surface species, combination of surface species, desorption of products, and regeneration of catalytic surfaces. It is one of the most extensively studied reactions, dating back to the classic work of Langmuir on Pt wires [3, 20, 21]. This reaction is also industrially significant. For example, the reaction contributes to air pollution control by removing CO from automobile exhausts. Another important practical application is the removal of trace amounts of CO from a large excess of hydrogen, which is also known as PROX (Preferential Oxidation), to purify hydrogen for photo exchange membrane fuel cells (PEMFCs). The results from CO oxidation investigations greatly assist studies of other reactions, for instance methane oxidation.

Reaction mechanisms of catalytic CO oxidation on Pt-group metals

The reaction mechanism, which describes the elementary steps of a reaction, is the key to understanding the reaction. For catalytic CO oxidation on Pt-group metals, the Langmuir-Hinshelwood (L-H) mechanism and the Eley –Rideal (E-R) mechanism have received the most attention. Recently, the Mars-van Krevelen Mechanism has been used to explain the reactions at high oxygen pressure conditions. However, among the proposed mechanisms, the L-H mechanism is the most widely accepted, and its validity is demonstrated in this dissertation. The following sections briefly describe these three mechanisms.

(a). Langmuir-Hinshelwood (L-H) mechanism

The Langmuir-Hinshelwood (L-H) mechanism describes a surface reaction involving adsorbed species, specifically CO and atomic oxygen. CO_2, the product, leaves the surface immediately following its formation [22]. The elementary steps involved in the L-H mechanism are illustrated as follows [20]:

$$CO_{(g)} \rightarrow CO_{(ads.)} \quad (1)$$

$$CO_{(ads.)} \rightarrow CO_{(g)} \quad (2)$$

$$O_{2(g)} \rightarrow 2O_{(ads.)} \quad (3)$$

$$O_{(ads.)} + CO_{(ads.)} \rightarrow CO_{2(g)} \quad (4)$$

Gas phase CO first adsorbs onto the metal surface (step (1)). Meanwhile, the adsorbed CO also desorbs from the surface (step (2)). Under steady-state conditions, these two steps are in equilibrium. Equation (3) describes the situation when O_2 dissociatively

adsorbs on the surface, which has been found to be true for Pt-group metal surfaces at temperatures higher than 200 K [23, 24]. The recombination and desorption of chemisorbed oxygen atoms generally occur at above 700 K, a higher temperature than the catalytic CO oxidation temperature. Therefore, these steps are not considered in the mechanism. CO_2 immediately desorbs from the surface after its formation, so that only gaseous CO_2 is involved in the L-H mechanism. For this mechanism, the reaction rate can be simply expressed as

$$r = k\,\theta_{CO}\,\theta_{O}. \qquad (5)$$

where r is the reaction rate; k is the rate constant; θ_{CO} and θ_O are coverages of CO and O on the surface, respectively. At different pressure, temperature, and gas compositions, the sticking probabilities of CO and O_2 vary, leading to different rate laws.

(b). Eley-Rideal (E-R) mechanism

The Eley-Rideal Mechanism does not require the adsorption of *both* reactants on the surface and can be described by the following equations:

$$CO_{(g)} + O_{(ads.)} \rightarrow CO_{2(g)} \qquad (6)$$

or,
$$CO_{(ads.)} + \tfrac{1}{2}\,O_{2(g)} \rightarrow CO_{2(g)} \qquad (7)$$

Equation (7) can be ruled out since adsorbed CO on a metal surface adopts an orientation such that C bonds with the surface while O points away from the surface. This leads to a situation in which carbon atom is protected from reacting with O_2. Moreover, experimental results have shown that no CO_2 formation is detected when gaseous oxygen is exposed to a CO-saturated surface [25]. Equation (6), however, has also been

shown as incorrect by the classic molecular beam experiments done by Ertl and coworkers, where the residence time of CO has been found to be nonzero [26].

(c). " Mars-van Krevelen mechanism"

In 1954, P. Mars and D.W. van Krevelen derived a rate expression that involves a surface redox mechanism, to describe rates of oxidation reactions on heterogeneous oxide catalysts [27]. The reaction mechanism can be described as follows:

I. reactant + oxidized catalyst → oxidation products + reduced catalyst

II. reduced catalyst + oxygen → oxidized catalyst

The key feature of this reaction mechanism is the involvement of lattice oxygen, in contrast with the chemisorbed oxygen species involved in the other two mechanisms.

CO oxidation at low pressures

In the investigations of catalytic CO oxidation, the study of CO and O co-adsorption on a surface and their mutual interactions are essential to the exploration of reaction mechanisms. This type of investigation is best done under well-controlled UHV conditions. Numerous studies have been performed in the past using this surface science approach. A comprehensive review on the studies of CO oxidation on platinum group metals under UHV conditions was undertaken by Engel and Ertl in 1979 [20]. The following three paragraphs present a short summary of their review.

At very low surface concentrations of $CO_{(ads.)}$ and $O_{(ads.)}$, reactants randomly distribute over the surface; the reaction rate follows perfectly the simple rate law r = k

θ_{CO} θ_O. With the increase of CO coverage, the repulsive interaction between adsorbed CO species forces the formation of various overlayer structures depending on coverage. On Pd(111), for example, both experimental and theoretical studies prove that $O_{(ads.)}$ species occupy three-fold hollow sites [28-30]. However, as the CO coverage increases to a certain value, for example $\theta_{CO} > 1/3$ ML, CO starts to populate hollow sites and thus hinders O_2 dissociation. The reaction is then inhibited (poisoned) by CO. As a consequence, if a surface is first saturated with CO, it becomes inert to oxygen and inactive. In contrast, if a surface is first saturated by oxygen, it will be able to adsorb a considerable amount of CO since CO tends to push O to form denser islands. This, in turn, creates an open space for CO adsorption. In this case, reactions occur along the boundaries of oxygen islands and CO islands. The same situation is also observed on the CO pre-covered surface but with a very low CO coverage.

The further adsorption of CO causes further compression of both domains. This results in weakened bonding of the adsorbed species with the metal surface and therefore greatly facilitates the reaction rate. A mixed phase of $CO_{(ads.)}$ and $O_{(ads.)}$ can also form at extremely high reactant coverages. In this case, the distance between $CO_{(ads.)}$ and $O_{(ads.)}$ is shortened, giving rise to an alteration of electronic states of CO evidenced by UPS [28] and IR [31, 32] studies. This mixed phase configuration is highly active and CO_2 can be formed well below room temperature [28]. However, it is proposed that this highly mixed phase will never form under steady-state conditions [20].

On a CO-dominated surface, the reaction rate is determined by the desorption rate of CO, since O_2 can only adsorb on surface sites created by CO desorption. This

leads to negative first-order dependence in CO partial pressure, positive first-order dependence in oxygen partial pressure, and approximately zero-order dependence in the total pressure. On an O-dominated surface, on the other hand, the reaction is first order dependent on CO partial pressure and independent of the O_2 partial pressure.

CO oxidation at high pressures: is there a pressure gap?

Studies on heterogeneous catalytic systems using the high pressure surface sensitive techniques yielded important results previously unknown. SFG and PM-IRAS studies regarding high pressure CO adsorption on Pd(111) [19, 33-35], Pt(110) [36], Pt(111) [16, 36], and Rh(111) [12] showed identical adsorption structures as those at low pressures, i.e., no new high-pressure CO species was found. The only exception appears to be a high-pressure SFG study on Pt(111) done by the Somorjai group [14, 37] who claimed a "new" CO vibrational feature at atmospheric pressures. This result, unfortunately, was later shown incorrect by other researchers [16, 25] and was indeed caused by water contamination. In this sense, there should not be a pressure gap when one considers CO adsorption at high pressures.

For the other reactant, O_2, the situation is completely different. Under various pressures and temperatures, there is vast literature in terms of interaction of O_2 with metal surfaces. Briefly, as the pressure of O_2 rises, oxygen involved phases change from chemisorbed oxygen overlayers to surface oxides and eventually bulk oxides. At very high temperatures, these oxides may decompose; and surfaces regain a metallic state. Take the oxidation on Pd(111) surface for example: at room temperature, the adsorption

of oxygen saturates at a coverage of 0.25 ML by forming a $p(2 \times 2)$ overlayer structure [38-40]. Deposition of oxygen at higher temperatures enables the increase of the oxygen coverage. When θ_O exceeds 0.25 ML, the adsorption rate into the chemisorbed state becomes small and oxygen starts to penetrate into the subsurface, causing the reconstruction of the Pd substrate [39-41]. At higher oxygen coverage, a two-dimensional surface oxide could be formed. The stoichiometry of the most stable surface oxide was identified as Pd_5O_4 by Lundgren and reported to be an incommensurate overlayer resembling a $\sqrt{6} \times \sqrt{6}$ arrangement [42], and the coverage was measured to be 0.58 ML [41]. The Pd_5O_4 2D oxide is regarded as the well-ordered intermediate state between chemisorbed oxygen and bulk PdO phase. A precursor state toward PdO formation was found by Weaver to be oxygen atoms adsorbed on top of a 2D oxide surface. Dissolution of oxygen into the bulk occurs at elevated pressures and temperatures, followed by the formation of bulk oxide PdO, leading to an increase of the inter-planar spacing between the first two layers [43]. The bulk oxide has been observed to form a “cauliflower-like” structure and the single crystal surface area increases as well during oxidation [43]. From these investigations, it becomes quite possible that a pressure gap may be seen during high pressure CO oxidation at certain reaction conditions (oxygen rich conditions).

For high pressure CO oxidation reactions, new phenomena were indeed found by some researchers. Lele et al. [44] and Rotemnund et al. [45] observed different spatio-temporal patterns during CO oxidation reactions on Pt(100) and Pt(110), respectively, using photoemission electron microscopy (PEEM) and ellipsomicroscopy

for surface imaging (EMSI) studies. RuO_2 was identified by Over and coworkers as the active phase that accounts for the high activity of Ru at high pressures [46]. Recently, based on in situ STM and reaction kinetics studies, Frenken and coworkers claimed that under high oxygen partial pressure conditions, CO oxidation reaches the highest activity on oxide phases and the reaction follows the Mars-van Krevelen oxidation-reduction mechanism [47]. However, their conclusions are debatable because their "high activity" reactions were performed in a mass transfer limited regime. Moreover, the Mars-van Krevelen mechanism was questioned by Vannice as "inconsistent and incorrect" and their rate expression "has no physical relevance, and must be viewed only as a mathematical fitting function." [48]. To clarify this conflictive issue, this dissertation will focus on in situ high pressure CO oxidation by means of PM-IRAS and reaction kinetics measurements.

Catalytically Active Au on Titanium Oxide

Gold is a well-known inert metal that exhibits much lower catalytic activities than other transition metals toward many reactions. However, it was found in the last decade that Au becomes extraordinarily active in various low-temperature catalytic reactions, such as CO oxidation, if Au is dispersed as ultra-fine particles supported on metal oxides such as TiO_2 [49, 50]. It is widely accepted that the size of Au particles plays a key role in the catalytic activity of Au catalysts. A significant increase in the reaction rate of low temperature oxidation of CO was observed as the diameter of the Au clusters is ~3.5 nm (Fig. 2) [51]. This size of Au clusters corresponds to the thickness of

two Au atoms (a bilayer) and has the band gap of 0.2 to 0.6 eV from the STM/STS study [51]. It is evident that Au nanoparticles with bilayer structure are more active than those with monolayer or multilayer structure.

Recently, two well-ordered Au films, a (1 × 1) monolayer and a (1 × 3) bilayer, which completely wet an ultra-thin TiO_x surface on Mo(112), were prepared in this laboratory [52]. Exceptional catalytic activity was reported for high pressure CO oxidation on the (1 × 3) bilayer Au films (Fig. 3). The specific rate per unit area was found to be 45 times higher than that reported for the most active highly dispersed Au/TiO_2 [53]. HREELS, LEED, and STM studies reveal the interaction between Ti and Au; the structures of (1 × 1) and (1 × 3) Au films were proposed as shown in Fig. 3. Au coverage of (1 × 3) Au film was determined to be 1.33 ML, and its structure exhibits the accessibility of reactants to both layers of Au [52].

In this dissertation, electronic and chemical properties of the mentioned (1 × 1) and (1 × 3) Au films explored by PM-IRAS are discussed and compared with those of a multilayer Au structure. The preparation procedures of the Au films are also described.

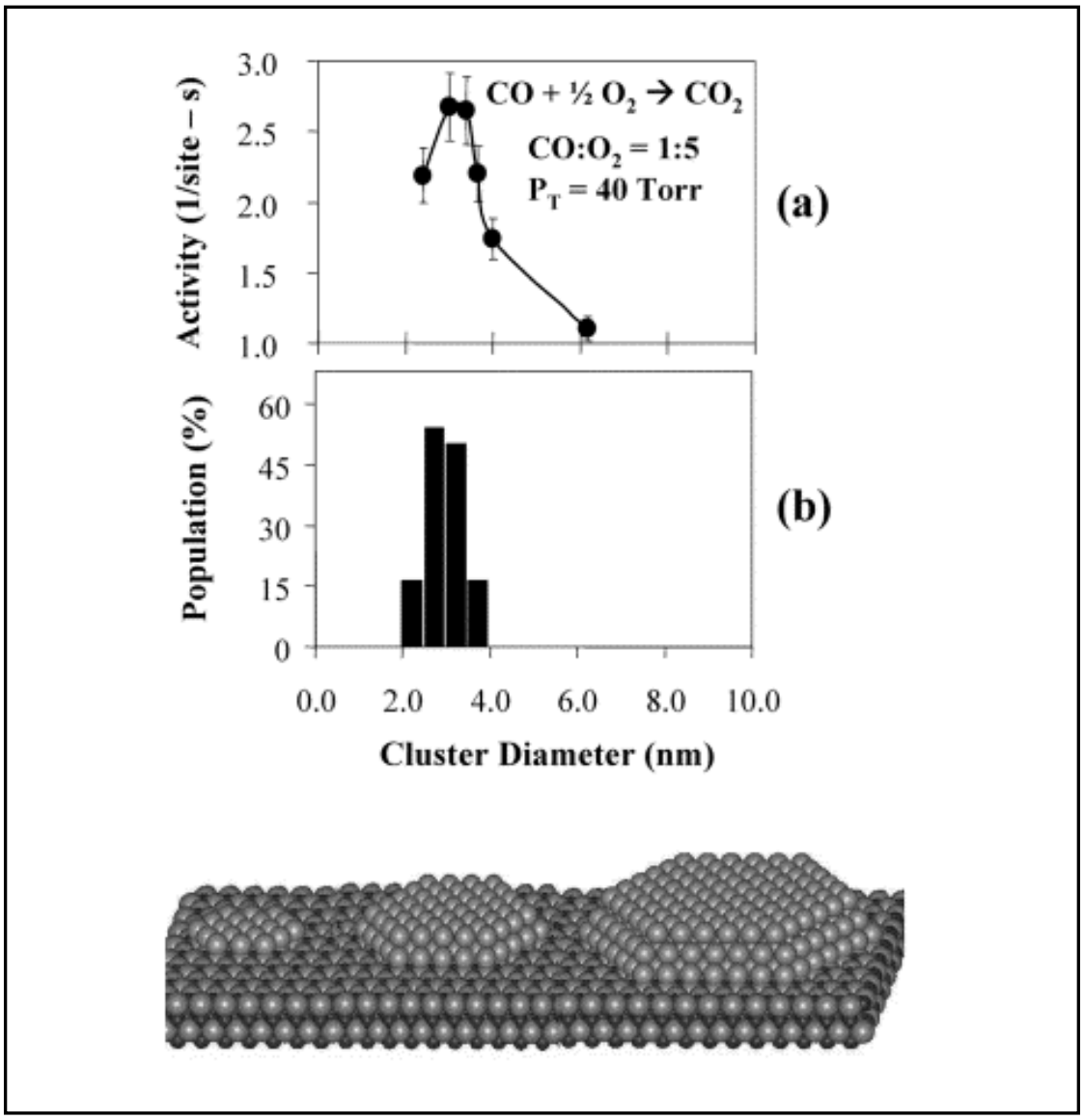

Fig. 2. The effect of the Au cluster size in CO oxidation reaction. (a) The activity at 350 K as a function of Au cluster size supported on TiO_2(110)-(1 × 1) thin films grown on Mo(100). A 1:5 CO/O_2 mixture was used at a total pressure of 40 Torr. (b) A histogram of the distribution of cluster sizes. The schematic at the bottom shows the evolution of the cluster morphologies within the 0–10 nm range [51].

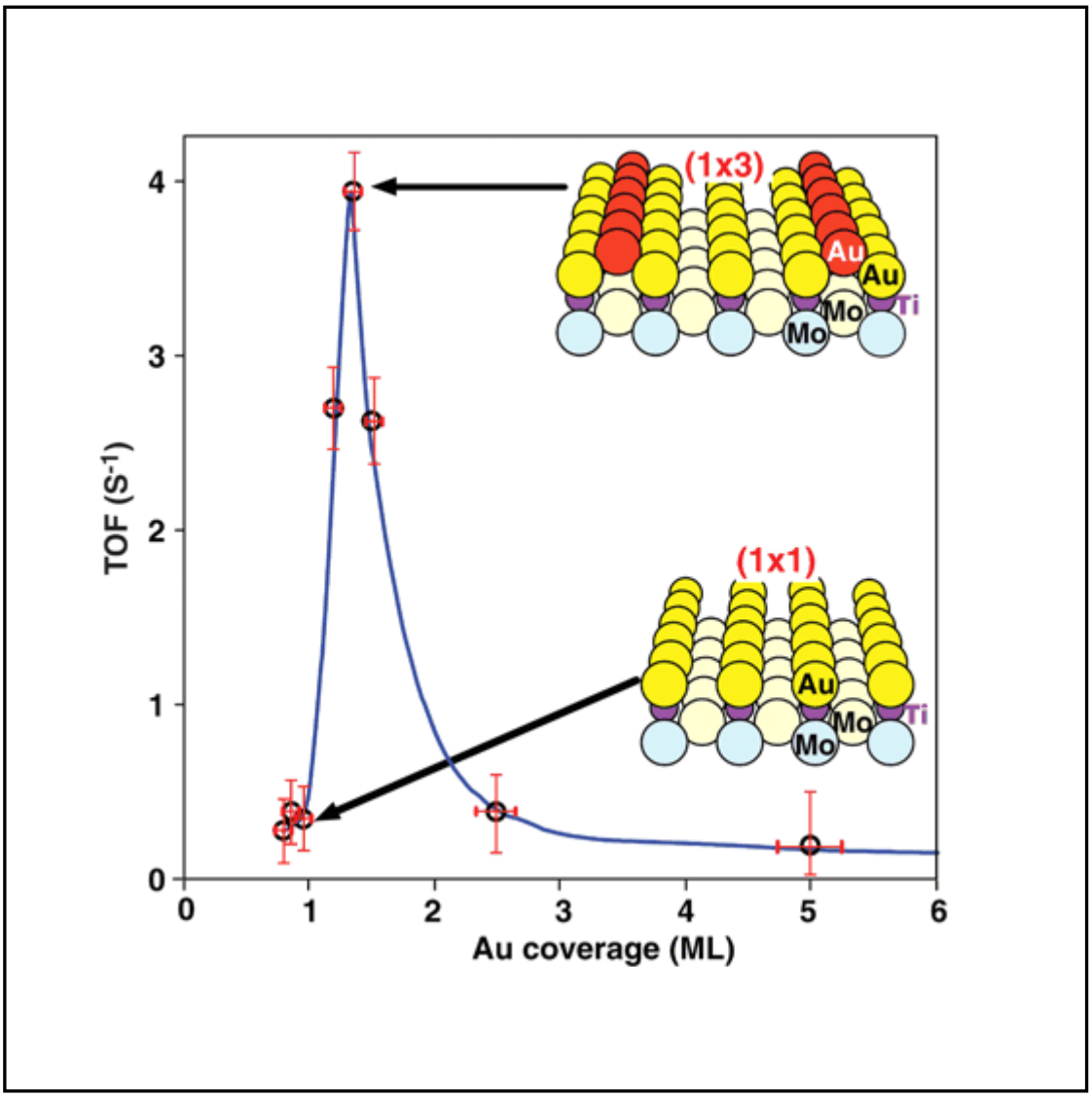

Fig. 3. Activity for CO oxidation at room temperature as a function of Au coverage on TiO_x/Mo(112). The CO/O_2 ratio was 2:1, and the total pressure was 5 Torr. Insets: Schematic models for the (1 × 1) and (1 × 3)-Au/TiO_x surfaces [52]

CHAPTER II

EXPERIMENTAL

This chapter introduces the experimental and technical fundamentals of this dissertation. The first section introduces the surface science techniques used in the experiments including Auger Electron Spectroscopy (AES), Low Energy Electron Diffraction (LEED), Infrared Reflection-Absorption Spectroscopy (IRAS), and Polarization Modulation Infrared Reflection-Absorption Spectroscopy (PM-IRAS). The experimental setup and sample preparations are described in the second section.

Surface Science Techniques

Auger Electron Spectroscopy (AES)

Auger Electron Spectroscopy (AES) has now emerged as one of the most widely used analytical techniques, providing the surface specific elemental information of a conducting surface. This technique is based on the Auger relaxation process discovered by Pierre Auger in1925 [54].

The Auger process can be described as the ionization of the core levels of a surface atom under electron beam bombardment. In detail, as illustrated schematically in Fig. 4, the specimen is first bombarded by a primary beam of electrons with kinetic energies of 2-10 keV, resulting in the photoemission of a core level electron and the formation of a core hole. The excited atom then releases energy via filling the core hole

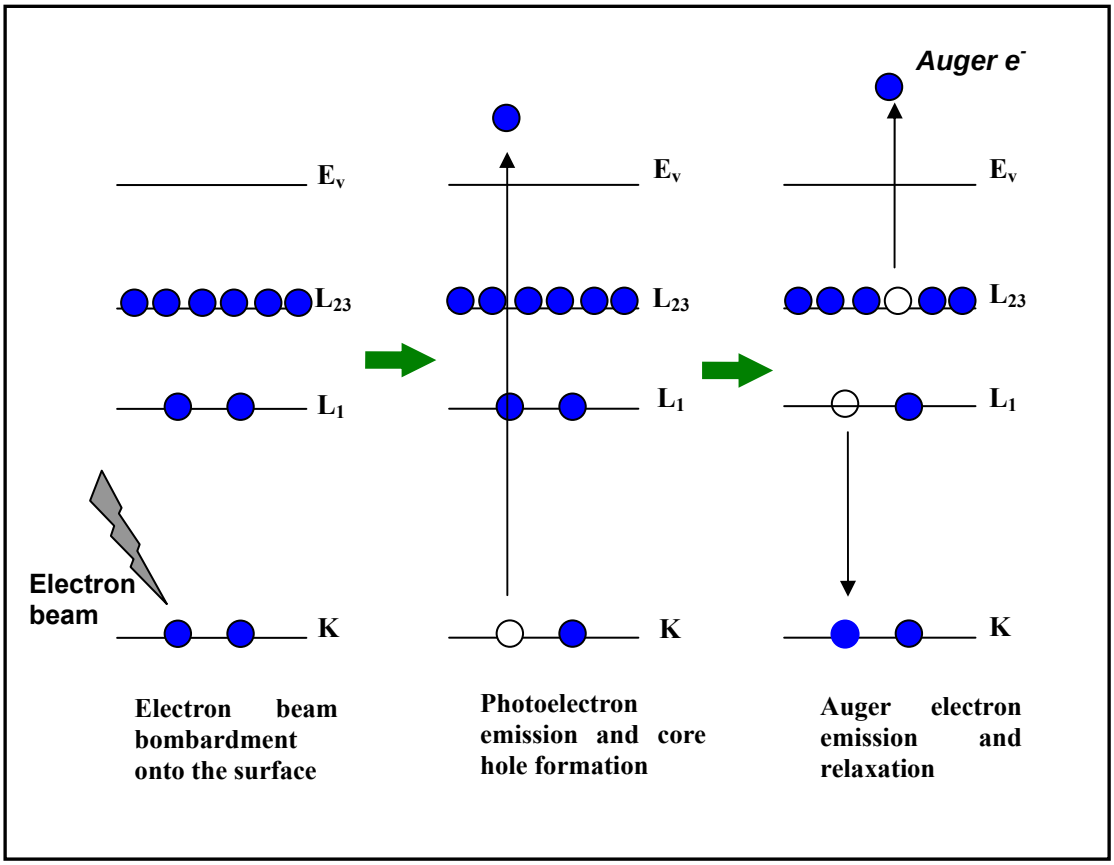

Fig. 4. Schematic diagram of the Auger process.

with an electron from a higher shell (L_1). The energy (E_K-E_{L1}) released from this transition ejects a secondary electron from the $L_{2,3}$ level, named as an Auger electron. After the emission of the Auger electron, the atom is left in a doubly ionized state. The above process is also denoted as a $KL_1L_{2,3}$ Auger transition. The energy of the Auger electron is determined only by the energy levels of an atom, and thus the distribution of kinetic energies provides a fingerprint for each element. The kinetic energy of the Auger electron from KL_1L_2 transition can be calculated as below:

$$E_{KL1L2,3} \approx E_K - E_{L1} - E_{L2,3} - \delta E - \Phi \qquad (8)$$

where, $E_{KL1L2,3}$ is the kinetic energy of the Auger electron, E_K, $_{L1}$, $_{L2,3}$ are the binding energies of the electrons in K, L_1, and $L_{2,3}$ shells, Φ is the work function of the sample, and δE is the energy shift caused by relaxation effects.

The emitted Auger electrons form small peaks superimposed in the total energy distribution function N(E), which includes a large background from the secondary electrons generated from various inelastic scattering processes. The conventional Auger spectrum is often presented as the function dN(E)/dE, with differentiation of the energy distribution function N(E), which removes the large background resulting in more pronounced peaks.

AES technique is considered surface sensitive due to the short mean free path of electrons in the kinetic energy range of 20-2500eV, and thus, it probes only the top few layers of a surface. Therefore, AES can be used to determine the coverage or thickness of the metal overlayers. In the most favorable case the overlayer will grow layer-by-layer on the substrate. During the growth of the first layer, the Auger signal of the overlayer

species will increase linearly, accompanied with a linear attenuation of the substrate signal with coverage up to the completion of the first layer. The second layer deposition will lead to the linear growth of the Auger signal of the deposit as well, but this linear rate will change due to the attenuation of emission from the first layer. As a result, a break point will appear in the plot of the AES intensity ratio of overlayer/substrate as a function of the deposition time.

In this study, AES spectra were obtained with an incident electron beam of energy of 2kV. The electrons were detected by a single pass CMA with a coaxial electron gun.

Low Energy Electron Diffraction (LEED)

Low Energy Electron Diffraction is one of the most frequently used techniques to explore the surface structure of the ordered overlayers and single crystals. In LEED, a diffraction pattern, namely the LEED pattern generated by the elastically scattered electrons from an ordered surface on which a monochromatic electron beam normally incidents is measured to collect the information of the periodicity of the surface. The energy of the electron beam used in LEED is typically in the range of 20 – 200 eV, which means electrons penetrate only ~10 Å into surface according to the universal curve [54], i.e., surface sensitive. Moreover, the wavelengths of 20-200 eV electrons are comparable with atomic spacing, which is the necessary condition for diffraction effects associated with atomic structure to be observed. Constructive interference occurs (diffractive intensity is significant) only when the scattering satisfies the Bragg

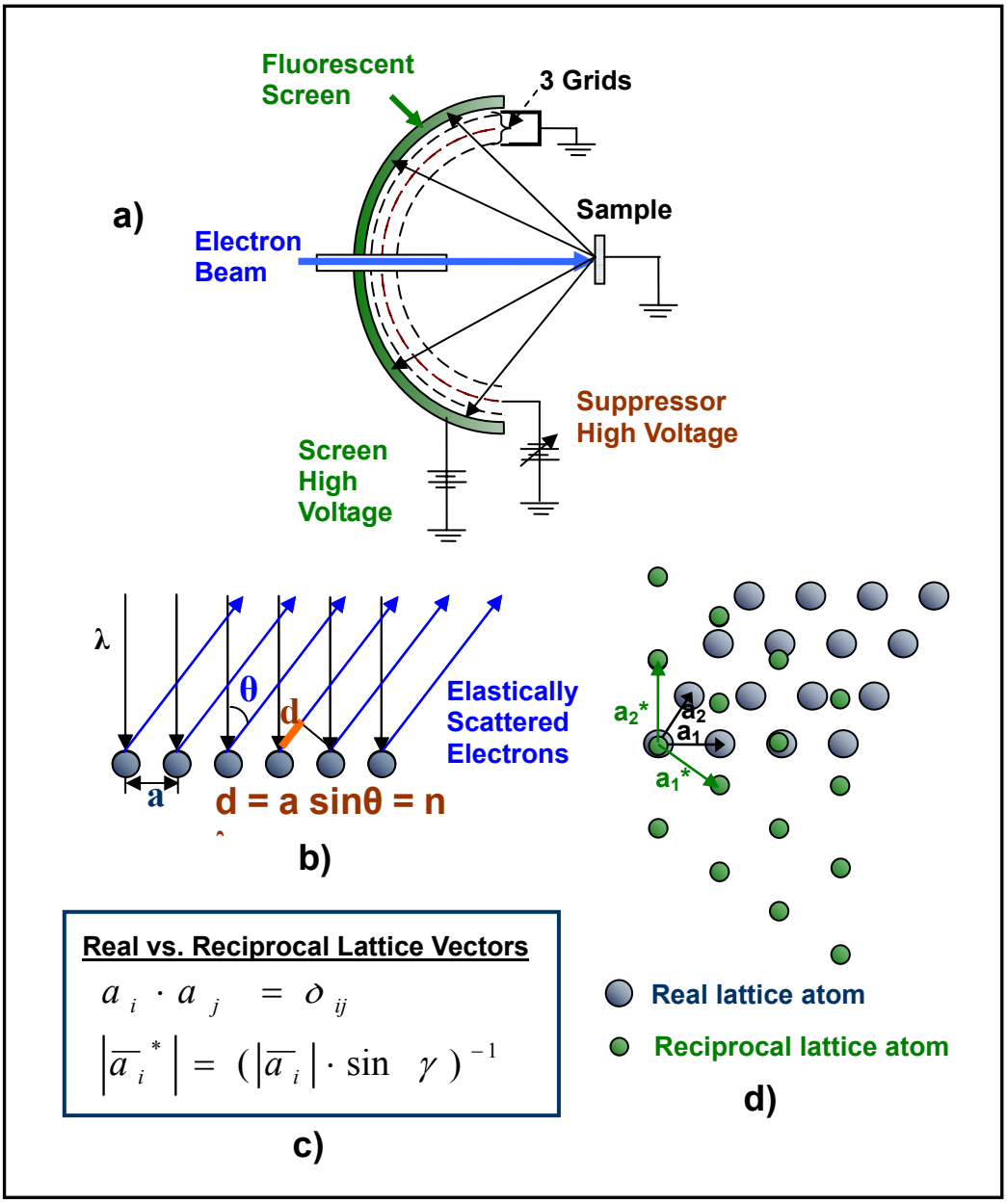

Fig. 5. LEED system and pattern formation. a) Schematic diagram of a standard LEED system. b) Elastic scattering process. c) Relationship between real and reciprocal lattice vectors. d) Real lattice and reciprocal lattice.

condition:

$$d = a \sin\theta = n\lambda. \quad (9)$$

where d is the path difference of scattered electrons traveling toward a detector, a is the distance between two adjacent atoms, and θ is the angle between the scattered beam and the surface normal. A better way to understand the LEED pattern involves the concept of reciprocal lattice. The reciprocal vectors are related to the real space unit cell vector by the scalar product relations (see Fig. 5c).

A standard LEED system is presented in Fig. 5a, including a hemispherical fluorescent screen with a fixed electron gun aligned along the central axis of the screen, with 3 or 4 hemispherical grids to screen out the inelastically scattered electrons (secondary electrons). The crystal sample is positioned at the center of the radius of the hemispherical screen.

The LEED pattern provides a two dimensional periodicity of the topmost surface. However, the position of the overlayer with respect to the substrate cannot be accurately determined by studying the pattern alone. I-V or I-θ must be applied to measure the atomic positions with higher accuracy.

Infrared Reflection Absorption Spectroscopy (IRAS)

IRAS is one of the most powerful tools in the investigation of molecular adsorptions on well-defined metal surfaces. In comparison with other vibrational techniques, such as High Resolution Electron Energy Loss Spectroscopy (HREELS) and Raman Spectroscopy, IRAS has a high sensitivity (< 1/1000 of a CO monolayer), a high

resolution (1-8 cm^{-1}), and virtually no pressure restrictions (from UHV to atmospheric pressures). These advantages enable IRAS to be the most widely used technique in the study of catalytically relevant systems.

In IRAS, the incident infrared beam is reflected from a highly reflective surface, such as a single crystal surface; the reflection loss due to the excitation of the adsorbed molecules is then measured, giving rise to a reflection absorption spectrum. The absorption of the infrared light by a molecule adsorbed on a metal surface is primarily affected by the dielectric behavior of the metal, because both the electric field of the incident infrared light and the dipole moment of the adsorbed molecule interact with the metal electrons. Theoretical studies [55] on IRAS have revealed that for metallic surfaces, only vibrations with a dipole moment perpendicular to the surface will be excited, which is known as the *surface selection rule* [56]. This can be rationalized from the phase differences and amplitude changes of the electric fields produced by the infrared radiation reflection on a metal surface as illustrated in Fig. 6. The incident infrared beam impinges at an angle φ with respect to the surface normal; the incidence and reflection of the radiation and the surface normal lie in the same plane, called the plane of incidence, perpendicular to the surface. The electric vector of the radiation parallel to the plane of incidence is named the *p*-polarization, with *s*-polarization being the perpendicular one, denoted as *Es* and *Ep* in Fig. 6, respectively. The phase change as a function of the incidence angle (Fig. 6b) indicates that at almost all angles of incidence the s-polarized electric vector suffers a 180^{o} phase change, resulting in the vanishing of the electric field at the surface due to the destructive interference. The phase change of

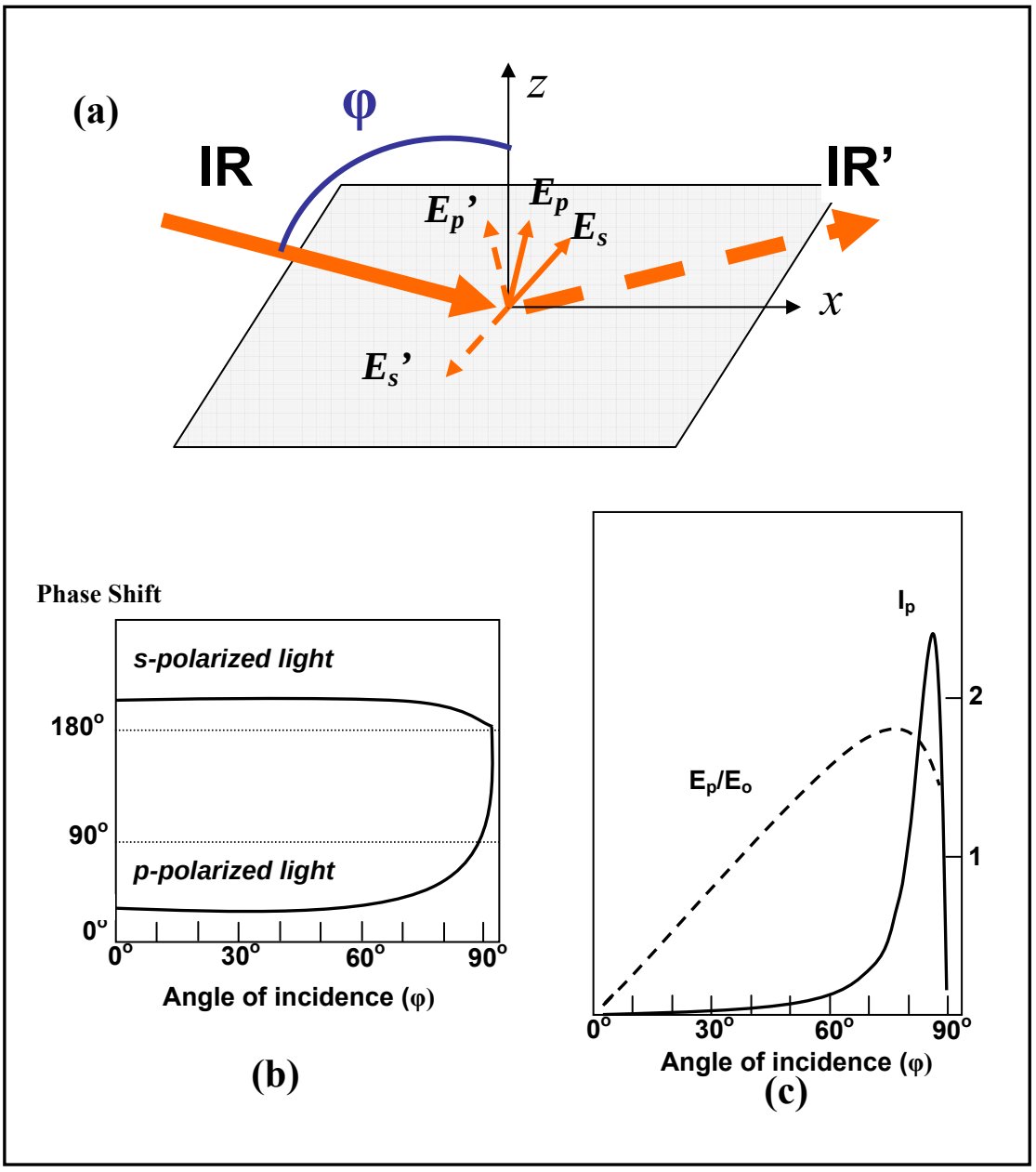

Fig. 6. Schematic representation of IRAS experiment. (a) The incident and reflected electric vectors of the p- and s-polarized infrared radiation at a metal surface. The plane of incidence is the xz plane. (b) Phase shift as a function of incidence angle. (c) Electrical field and intensity of p-light as a function of incidence angle. (Fig. 6 (b-c) are adapted from Ref. [56].)

the *p*-polarized vector, however, strongly depends on the angle of incidence and retains a small value for $0^o < \varphi < 85^o$. Furthermore, at a near grazing angle of incidence, the amplitude of the electric field of p-component reaches the maxima, nearly doubling that of the incidence light as shown in Fig. 6c, whereas the s-polarized light virtually has no intensity at the metal surface. Therefore, only the *p*-polarized component can interact strongly with the adsorbate which has a dipole moment perpendicular to the surface. To summarize, only the vibrational mode with a dipole moment perpendicular to the surface can be excited, and the p-polarized incidence at a near grazing angle to the surface is necessary in the performance of an IRAS experiment.

From IRA spectra, the information on the interaction between the adsorbate and metal substrate, as well as that between adsorbed molecules, can be obtained from the frequency shift, intensity change, and the width of the absorption band. For single molecule adsorptions on the metal surface, the most prominent factors that induce the frequency shift suggested by Hoffmann [56] are mechanical renormalization, the self-image dipole, and the chemical bond with the surface. Mechanical renormalization occurs when a diatomic molecule, CO for instance, adsorbs onto a rigid substrate, resulting in a frequency shift toward a higher wavenumber (blue shift), ~ 50 cm^{-1} for the case of CO. The interaction of adsorbed molecule with its own image in the metal surface, so-called self-image dipole effect, influenced by a local electric field which is sensitive to the different adsorption sites, will cause a red shift for CO of 30 ~ 50 cm^{-1}. The third factor is related to the chemical interaction between the adsorbed molecule and the substrate, which is believed to account for the appearance of different adsorption

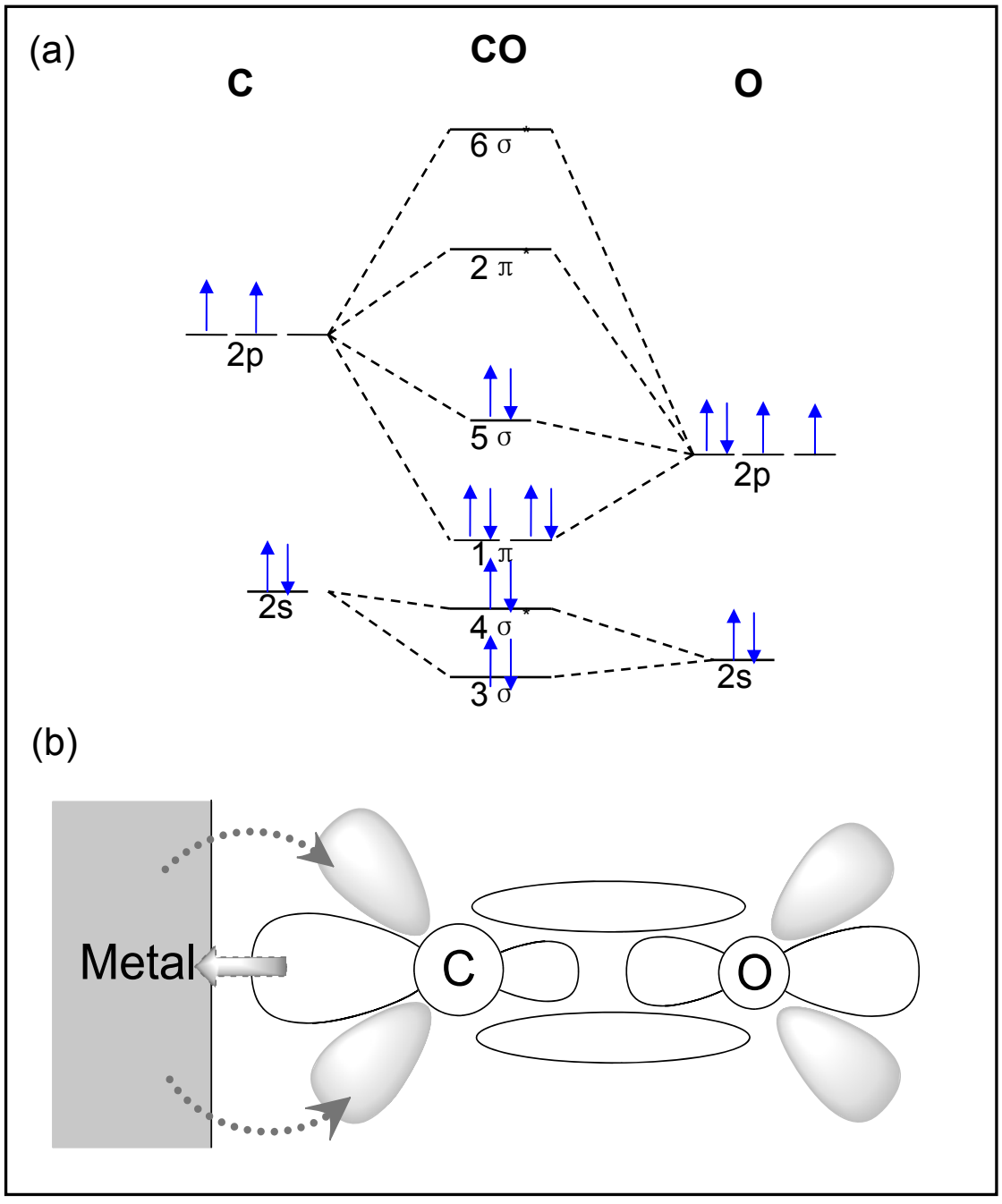

Fig. 7. Molecular level representation of CO-metal interaction. (a) Molecular orbital diagram for CO. (b) CO-Metal donation-backdonation mechanism (Blyholder mode).

bands when CO adsorbs on a transition metal surface, such as Pd [56]. A theoretical description of this interaction was given by Blyholder: the chemical bond formation between CO and metal substrate is through the electron transfer from the 5σ MO of CO to the metal and the "back-donation" of the charge from the metal d-band to the 2π* of CO (Fig. 7) [57]. Chemical bonding of CO to metal weakens the C-O bond and thus causes the red-shift of the CO vibrational frequency. It is generally accepted that CO adsorption on metals with the stretching frequencies above 2000 cm^{-1} is associated with a linear configuration, while frequencies between ~ 1860 cm^{-1} and 2000 cm^{-1} correspond to adsorption on bridge sites, and those below approximately 1860 cm^{-1} are from three-fold hollow site adsorptions [56].

Polarization Modulation Infrared Reflection and Absorption Spectroscopy (PM-IRAS)

As mentioned in the preceding section, one advantage of IRAS over HREELS is that IRAS can be operated under high pressure reaction conditions. However, since the exposed planar metal surface is generally less than 1 cm^2, at high pressures, the signal from the surface adsorbates is orders of magnitude smaller than the gas phase absorption. Take CO adsorption for example, at pressure above 10^{-3} mbar, the contribution of the gas-phase CO to the absorption spectra obscures the weak surface absorption signal of CO. Fig. 8 exhibits the IRA spectrum of 50 mbar CO adsorption on Pt(111) at 300 K [17]. The signal from linear CO adsorption (2060 cm^{-1}) is obscured by the

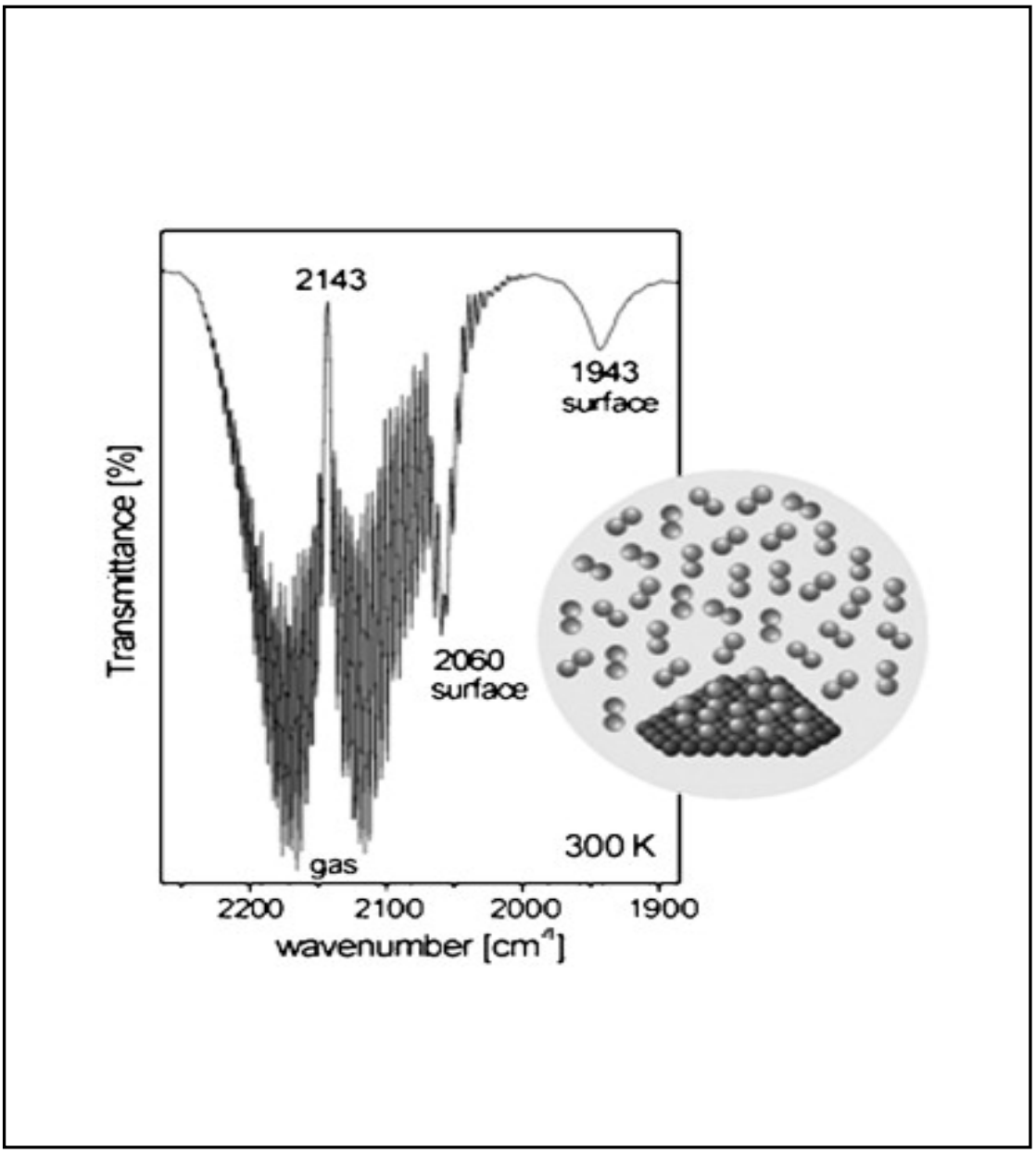

Fig. 8. An IRA spectrum of 50 mbar CO adsorption on Pt(111) at 300 K (Adapted from Ref. [17]).

rotovibrational absorption of gas phase CO. To solve this problem, in 1978, Overend [58] in Minnesota was the first to apply polarization modulation technique to discriminate the surface contributions from the gas phase, in a study of adsorbed CO on polycrystalline Pt foil in the presence of up to 55 Torr CO. The PM-IRAS technique was applied to heterogeneous catalysis study on model systems for the first time by Beitel et al. in 1996, i.e., CO adsorption on Co(0001) under 1-600 mbar of pressure at temperatures between 300 and 520 K [59].

The basic principle of polarization modulation is a fast modulation of the polarization state of the near grazing incident infrared beam between p-polarized light (parallel to the plane of incidence) and s-polarized light (perpendicular to the plane of incidence). According to the metal surface selection rule, both p- and s-polarized light are absorbed by randomly oriented (isotropic) gas/liquid phase molecules, while p-polarized light is absorbed by the oriented molecules adsorbed on the metal surface. Thus, if s-polarized absorptions (I_s) are subtracted from p-polarized absorptions (I_p) and normalized by the absorptions of both p- and s- lights, a surface sensitive infrared spectrum, virtually independent of the environmental conditions, can be obtained.

Polarization modulation is realized through a photoelastic modulator (PEM), a resonance device (see Fig. 9) which produces oscillating birefringence at a fixed frequency. PEM's operation principle is based on the photoelastic effect. In brief, when a transparent solid material (e.g., ZnSe crystal) is stressed by compression or stretch, the material exhibits birefringence proportional to the resulting strain, i.e., different linear polarizations (s- or p-) of light have slightly different speeds of light when passing

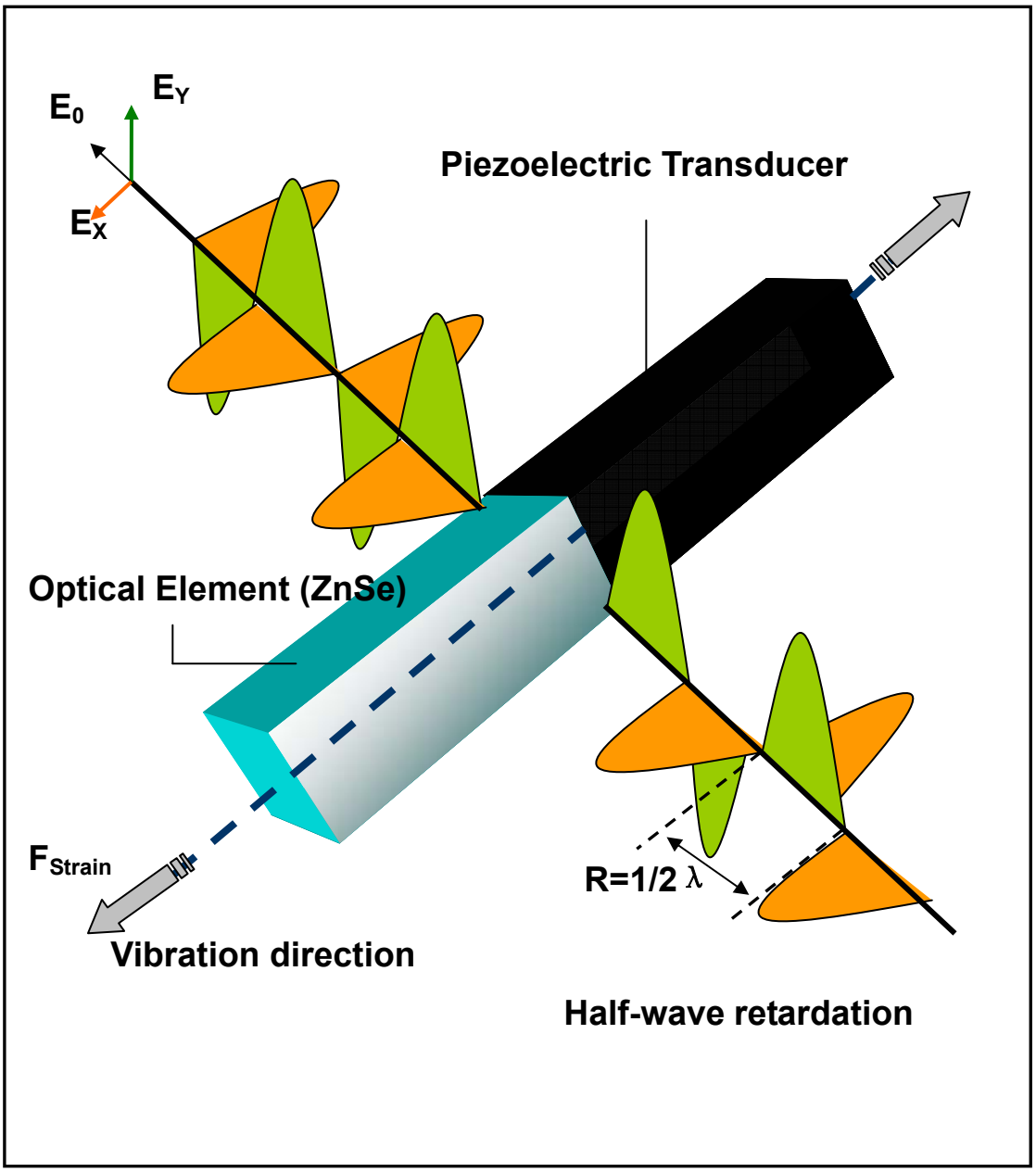

Fig. 9. Operation principle of a photoelastic modulator.

through the material. The mechanical force generated on the ZnSe crystal is controlled electronically by the PEM Controller via adding a sinusoidal voltage to the piezoelectric transducer inside the PEM. When the phase difference between two polarized lights, referred to as retardation, reaches one-half of the wavelength of the light, it can be rotated 90 degree with a frequency of 50 kHz. In the polarization of the light (Fig. 9), a state which is called half-wave retardation mode, the incoming infrared light impinging onto the sample surface can be switched back and forth from p- to s- polarizations extremely rapidly. The two orthogonal polarized states occur twice in each PEM oscillating cycle. Therefore, the sampling frequency is twice the frequency of the sinusoidal mechanical stress applied to the ZnSe crystal.

PM-IRAS optical setup

PM-IRA optical setup used in the present study is illustrated in Fig. 10. The spectrometer and the polarization modulation (PM) optics are placed on a steel honeycomb optical top (Technical Manufacturing Corporation), which is vibrationally isolated with pneumatic legs. An infrared beam generated from the infrared spectrometer (Equinox 55, Bruker Optics) is first focused by an Au-coated parabolic mirror (focal length 12”, Bruker Optics) onto the sample at an angle of 85 degrees with respect to the surface normal. Before reaching the sample surface, the infrared beam first passes through a wire-grid polarizer (Graseby Speca, Inc.). The grids of the polarizer are aligned parallel to the sample surface so that the transmitted light has only a p-polarized electric field vector. The linear polarized light from the wire-grid polarizer then passes

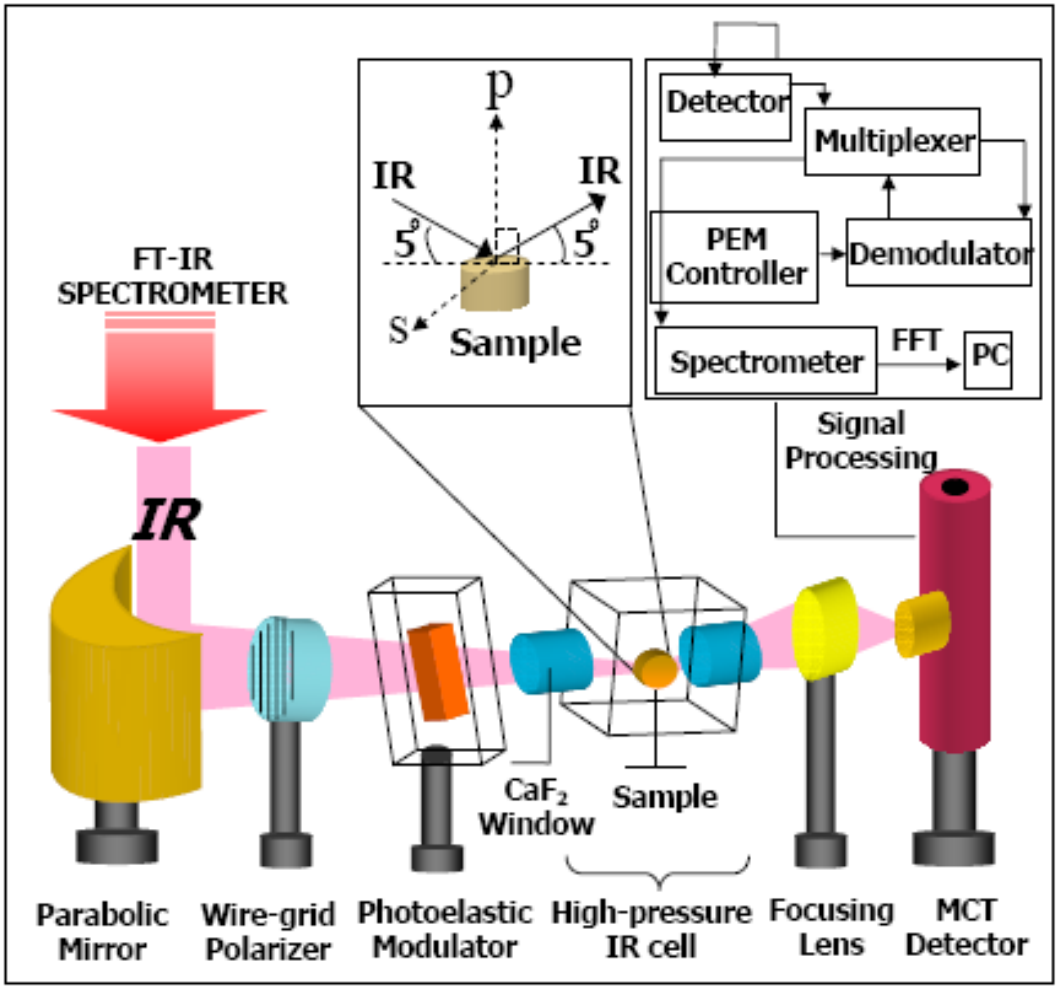

Fig. 10. Optical setup of PM-IRAS experiments and signal processing devices.

through a photoelastic modulator (PEM) (II/ZS50, 50 kHz, Hinds Instrument) consisting of a ZnSe crystal attached with a piezoelectric transducer. The PEM is oriented at 45 degrees with respect to the surface normal to enable s- and p- polarized lights alternately incident on the detector. After reflecting from the sample, the infrared beam reflected is collected by a focusing lens (Bruker Opitcs) and detected by a nitrogen-cooled MCT detector (D313/6-M, Infrared Associates, Inc.).

The signals collected by the detector are processed using a single analog to digital converter (ADC), a multiplexing electronic unit (IR Multiplexer XA/2, Bruker Optics), a photoelastic modulator controller (PEM 90D), and a synchronous sampling demodulator (SSD-100-15, GWC Instruments). Through these real-time sampling electronics, the interferogram containing both the sum ($I_p + I_s$) and the difference ($I_p - I_s$) signals is obtained (Fig. 11a). The Fast Fourier Transform (FFT) is then applied to deconvolute the interferogram into two separate infrared spectra, sum spectrum and difference spectrum (Fig. 11b). The PM-IRA spectrum, also called *differential reflectance spectrum*, is generated from the difference spectrum divided by the sum spectrum (Fig. 11c).

The PM-IRAS can also be understood from the following equations given by Corn et.al [60]

$$I(t) = (I_p + I_s + (I_p - I_s) \cos (\varphi_o \cos (\gamma t))) / 2 \qquad (10)$$

where $I_{p,s}$ are the *p* and *s*-polarized light intensities with respect to the sample surface, cos (γt) is set to a modulation frequency of 50 kHz. φ_o is a constant with respect to time, which depends linearly on the modulation voltage and is inversely related to the

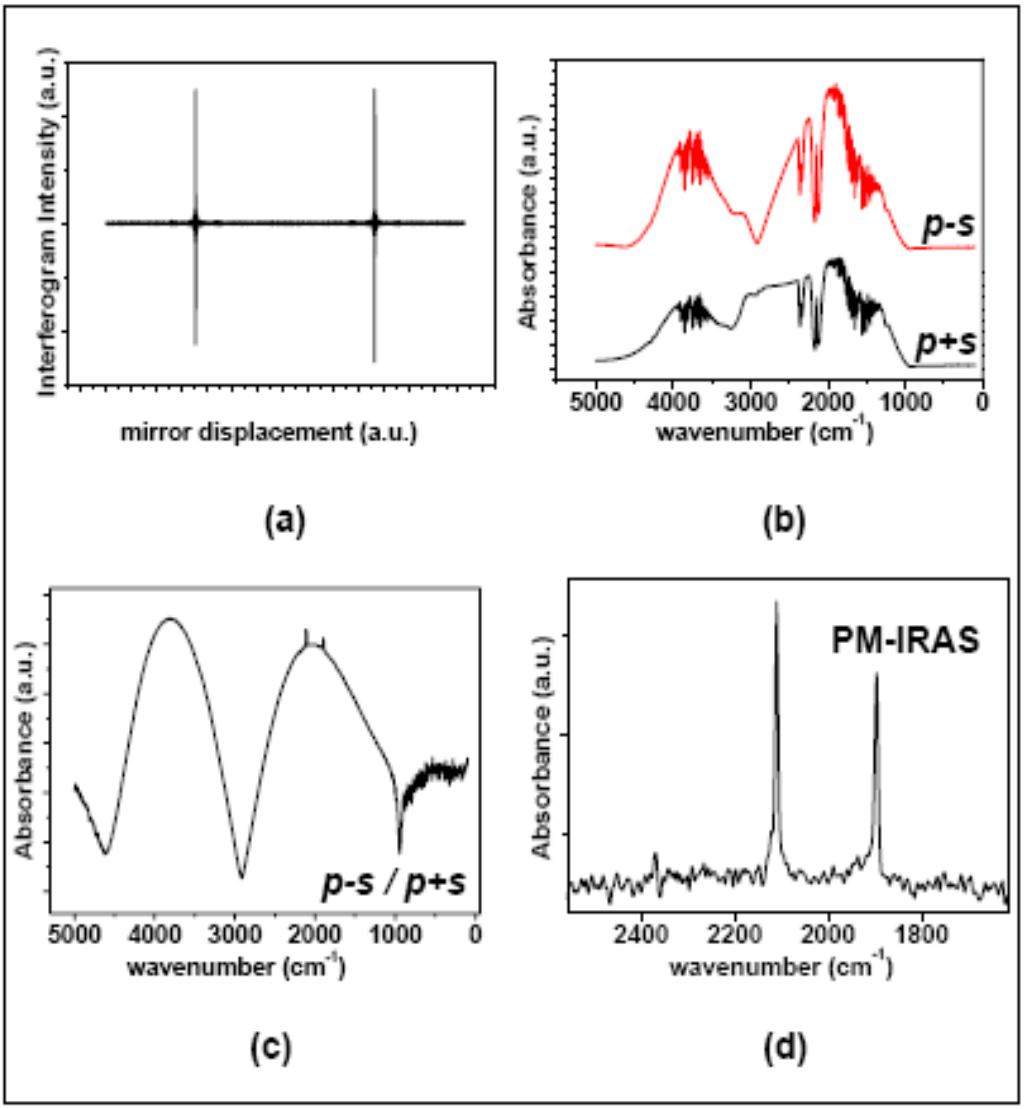

Fig. 11. Signal processing steps of PM-IRA spectra. (a) Double-channel interferogram. (b) Sum and difference channels after FFT. (c) Difference channel after normalized by sum channel. (d) PM-IRA spectrum after baseline correction.

wavelength of the IR light ($\varphi_o \sim V_m/\lambda$). Then,

$$I(t) = I_p \qquad \gamma t = 90^o, 270^0 \tag{11}$$

and

$$I(t) = \text{“}I_s\text{”} = I_s + (I_p - I_s)(1+\cos \varphi_o)/2 \qquad \gamma t = 0^o, 180^o \tag{12}$$

Real-time sampling electronics used for demodulation of the PM-IRAS signal thus measure the signal $I(t)$ at 0^o and 90^o during each modulation cycle and then compute the *sum* (I_p + “I_s”) and difference (I_p - “I_s”) spectra. Then the difference spectrum can be divided by the sum spectrum to obtain a differential reflectance spectrum ($\Delta R/R$) in the form:

$$\Delta R/R \approx ((1-\cos \varphi_o)/2 - (I_p - I_s) / ((I_p + I_s)/2) \text{ x } (\sin^2 \varphi_o)/8) \text{ x } ((I_p - I_s) / ((I_p + I_s)/2)) \tag{13}$$

which can also be written as:

$$\Delta R/R \approx J_2(\varphi_o) ((I_p - I_s) / (I_p + I_s)) \tag{14}$$

Experimental Setup

All experiments were carried out in a stainless steel UHV chamber consisting of two compartments (Fig. 12). The main chamber is equipped with a number of surface analysis probes, including a PHI 11-020 single pass CMA for AES measurements, a PHI 11-020 Low Energy Electron Diffraction (LEED) screen, and a UTI-100 mass spectrometer (MS). The base pressure for the main chamber maintains at ~5.0×10^{-10} Torr following bake out. A high-pressure cell (HPC) equipped with CaF_2 windows is attached to the bottom of the surface analysis chamber. The HPC is separated from the UHV

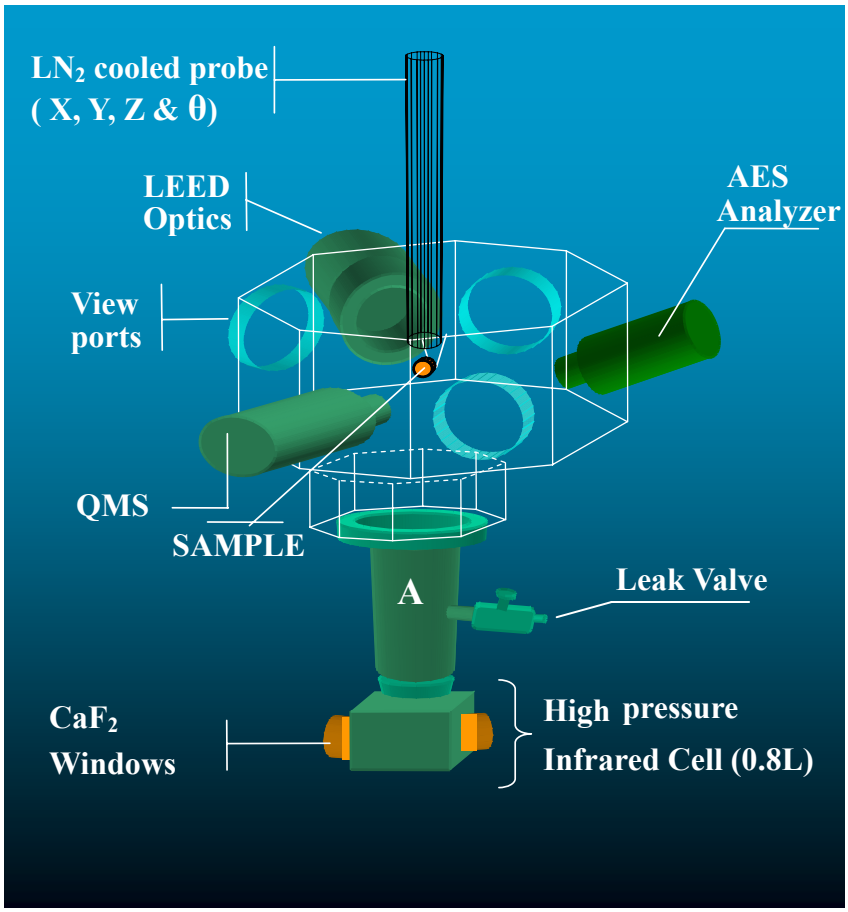

Fig. 12. Schematic representation of PM-IRAS chamber setup.

chamber via a doubly differentially pumped sliding seal, enabling the transfer of the sample between the UHV chamber and HPC stage. The pressure of the HPC can be increased to 1 atm with no disruption of the vacuum condition in the main chamber.

In the MS-PMIRAS experiments, the differentially pumped sliding seal was removed, and the connection (denoted as "A" in Fig. 12) between the HPC and the surface analysis chamber was replaced with a larger diameter tubing to enable good transportation of gas reactants and products.

PM-IRAS experiments were carried out using a Bruker Equinox 55 FTIR spectrometer coupled with a static wire-grid polarizer and a photoelastic modulator to subtract infrared signals arising from the gas phase. IR signal was detected by a liquid nitrogen cooled MCT detector, and spectra were typically obtained with 4 cm^{-1} resolution.

Sample Preparation and Gas Handling

The single crystals used in the experiments were first mounted to a tantalum wire and then attached to copper rods, which were then attached to the feedthrough. The temperature of the sample was monitored by a W-5%Re/W-26%Re (C-type) thermocouple spot-welded to the back side of the crystal. The samples can be cooled to ~90 K using liquid nitrogen and annealed to ~2400 K using electron bombardment. The Mo(112) sample was cleaned by repeated cycles of oxidation at 1200 K followed by flashing to 2100 K. The Pd single crystals were cleaned by the repeated cycles of Argon ion sputtering, oxidizing in $1x10^{-7}$ Torr oxygen at 800 K and resistively annealing to

1100 K. The cleaning process of Rh(111) is similar to that of Pd single crystals except that the annealing temperature is slightly higher (1300 K). This is achieved by electron bombardment. The cleanliness of the samples was routinely monitored with LEED and AES.

Research grade (99.999%, Matheson) CO and O_2 were used. The CO was further purified by storing it in a liquid nitrogen cooled trap to remove trace amounts of carbonyl contaminants. Purified CO and O_2 were mixed thoroughly before being introduced into the chamber. For steady-state reactions performed at low pressures ($< 10^{-3}$ Torr), the reaction was monitored with the mass spectrometer and reaction rates were calculated from signal intensities at 28 (CO) and 44 (CO_2) amu. For reaction performed at high pressures, the reaction rate was derived from the pressure change of the gaseous mixtures, which was monitored with a Baratron gauge (MKS Instrument).

CHAPTER III

NO ADSORPTION AND DISSOCIATION ON Rh(111)*

Literature Review on NO/Rh(111)

Because of its ability to convert NO to N_2 with high selectivity, rhodium has become an integral part of automotive catalytic converters [61-64]. To gain a better understanding of the mechanism behind this conversion, numerous surface science studies have used techniques such as low energy electron diffraction (LEED), temperature programmed desorption (TPD), X-ray photoelectron spectroscopy (XPS), and high-resolution electron energy loss spectroscopy (HREELS). These studies have generally focused on the adsorption and dissociation that take place on the low Miller index surfaces (i.e., Rh(111), (100), and (110)) and also on polycrystalline Rh [65-73]. However, more recent work has focused on more highly stepped surfaces in an attempt to determine if these surfaces are more active for NO dissociation than flat surfaces [74-76].

Early work on the NO/Rh(111) system was carried out by Castner et al., using LEED and TPD [77-79]. These authors found that NO adsorbed at 298 K produced a *c*(4 × 2) LEED pattern at low coverage, i.e., ~0.1 langmuir, L (1 L = 1×10^{-6} Torr s), which converted to a (2 × 2) pattern as the NO coverage was increased beyond 1 L. Subsequent studies aimed at understanding NO coordination and dissociation on the Rh(111) system

---

* Reprinted with permission from "NO Adsorption and Dissociation on Rh(111): PM-IRAS Study" by W.T. Wallace, Y. Cai, M.S. Chen, D. W. Goodman, J. Phys. Chem. B**,** 110 (2006) 6245, Copyright (2006) American Chemical Society.

were carried out by Root et al. using TPD and HREELS [77-82]. At low NO coverages at 95 K, these authors observed a loss feature between 1480 and 1630 cm^{-1} that was attributed to NO bound at bridging sites. They also noted that no LEED pattern was observed at 95 K but that heating to 250 K resulted in the appearance of a (2 × 1) pattern, in contrast to the patterns seen by Castner et al. [77]. TPD showed desorption of NO at ~450 K, with N_2 and O_2 desorbing at higher temperatures. HREELS was used to observe the dissociation of NO in situ. At low NO coverage, the NO stretching feature at 1500 cm^{-1} disappeared at 325 K, well below the NO desorption temperature, providing evidence for complete NO dissociation. By increasing NO coverage, the molecular NO stretching feature (1630 cm^{-1}) was still evident at 425 K, indicating that, at high coverages, dissociation is limited in the absence of NO desorption due to insufficient surface sites. The oxygen atoms produced during NO decomposition were postulated to adsorb in the hollow sites, while it was suggested that the N atoms may diffuse into the near-surface metal region. The latter conclusion followed because of the absence of a Rh-N stretching mode and the very weak N(1s) XPS intensity even at high coverages [74, 82]. Root et al. also studied the effects of coadsorbed oxygen on NO adsorption[81]. After creating a surface containing 0.37 ML oxygen, exposures of small amounts of NO produced a loss peak at 1580 cm^{-1}, significantly blue-shifted from that seen when NO was exposed to the clean Rh surface. Of greater interest was the appearance of a small loss peak at 1850 cm^{-1} corresponding to NO on atop sites. Because this feature was present only with coadsorbed oxygen, the authors concluded that NO adsorbs at atop sites on Rh(111) only in the presence of coadsorbed oxygen.

More recently, Rider et al. have studied the effects of higher pressures on the surface structures obtained for NO/Rh(111) [83, 84]. Using high-pressure scanning tunneling microscopy at room temperature, these authors observed a change in the NO surface structure as a function of pressure. While a (2 × 2) structure is obtained when small amounts of NO are added to the Rh(111) surface at 200 K, it is also possible to maintain this structure at room temperature in a background of 10^{-8} Torr. Rider et al. found that this structure transformed into (3 × 3) domains at~300 K as the pressure was increased to 0.01-0.05 Torr. Using their pressure and temperature data, Rider et al. found that the energy barrier for the transition between the phases was on the order of 0.7 eV. Subsequent studies addressing CO and NO coadsorption found that CO and NO mixed in a (2 × 2)-3(CO-NO) structure. As the pressure of NO was increased, however, NO-rich islands formed with a (3 × 3) structure.

The current consensus regarding the NO/Rh(111) system can be summarized as follows. At temperatures below 275 K, NO adsorbs molecularly; above this temperature, dissociation of NO takes place, forming two different structures that depend on the temperature and coverage. At low coverages (<0.25 ML), all NO dissociates between 275 and 325 K, and the N atoms combine and desorb between 450 and 650 K. At higher coverages, some NO dissociates above 300 K until all empty 3-fold hollow sites are filled. At this point, decomposition is inhibited. Raising the NO coverage even further results in the adsorption of NO on atop and 3-fold hollow sites. At this point, NO dissociation is inhibited until >400 K where 3-fold hollow NO begins to desorb.

While a significant number of studies have been carried out on Rh single crystals

in an attempt to gain a better understanding of the mechanism of NO decomposition and the changes that occur under more realistic pressures [61-64, 66-70, 72, 73, 76-82, 84, 85], several theoretical studies of this system have also been performed [75, 86-89]. Sautet and co-workers used density functional theory (DFT) to study the adsorption of NO on Rh(111) at three different coverages [75, 88]. These authors found that at 0.33 and 0.5 ML, the most stable adsorption site for NO was a 3-fold hollow site. At 0.75 monolayers, however, the most stable configuration consisted of one NO in an atop site and two in 3-fold hollow sites. These results are in direct contrast to earlier experimental work showing NO in bridging sites [80, 81] or one NO in an atop site and two in bridging sites [78]. Following further experimental studies, it was later agreed that the feature attributed to a bridging site was actually a 3-fold hollow site [66, 86].

Loffreda et al. [75] have used DFT to study NO adsorption on close-packed (111), open (100), and stepped (511) Rh surfaces to understand what role surface structure might play in dissociation activity. This kind of study is highly relevant since the supported Rh clusters used as commercial catalysts typically exhibit a variety of surface defects. The authors found that the most stable adsorption site for NO at 1/6 ML coverage on Rh(511) was at a bridging site overlooking a step, although several other configurations are within a few tenths of an electronvolt of being stable. Regarding the dissociation of NO, the authors found the highest activity for <100> terraces of the Rh(511) surface and proposed that NO dissociation on Rh(111) surfaces could be dominated by steps, possibly of the <100> variety.

While experimental and theoretical studies on single crystal rhodium surfaces

have provided a better understanding of the mechanism of NO bond scission, the ultimate goal is to determine whether the NO dissociation mechanism on single crystal surfaces is the same as that on supported metal clusters of commercial catalysts. Several groups are currently looking at various reactions involving NO on supported Rh particles [90-93].

With respect to the question of NO decomposition, Overbury and co-workers recently presented some intriguing results [91, 92]. These authors found that Rh supported on a reduced ceria (CeO*x*) thin film is more active for NO dissociation than Rh supported on an oxidized ceria (CeO2) thin film, which behaves like a single crystal surface. They noted that, while oxygen spillover from the Rh clusters to the support frees up sites for further NO dissociation, the level of enhanced dissociation does not appear to result simply from oxygen spillover. Using angle-resolved temperature-programmed desorption (ARTPD), Matsushima et al. [94] proposed that N_2O is the reaction intermediate during NO decomposition.

In further studies, Overbury and co-workers [92] studied the coverage dependence of NO dissociation over Rh supported on ceria thin films. Using XPS, they found that saturation NO on Rh/CeO2 at 250 K results in two features in the N(1s) region, which they assigned to undissociated NO and the dissociation product N. A Rh/CeO*x* surface was found to dissociate large amounts of NO at 300 K, with complete conversion by 350 K, while no NO dissociation was seen on the highly oxidized surface. At lower coverages, the dissociation temperature decreased for both supports. Poisoning the oxygen vacancies of the reduced ceria surface with H_2O did not affect the enhanced

dissociation, supporting the previous conclusion that oxygen spillover could not account for the enhancement. The authors noted that NO dissociation had been seen at lower temperatures on the more open Rh surfaces (such as the Rh(100) surface), so it was possible that Rh adopts more active morphologies on reduced ceria.

Currently, there is still disagreement regarding NO surface structures on Rh(111), one concern being the failure to account for dissociated N and O atoms in the structural models. The actual transition in NO binding from 3-fold hollow to atop sites is still not completely understood, nor is the process of how the dissociation products affect this transition. In this paper, we describe studies using Auger electron spectroscopy (AES) and polarization modulation infrared reflection absorption spectroscopy (PM-IRAS) where we follow the structural transitions of NO on Rh(111) and the role of adsorbed oxygen and nitrogen in altering these structures. To our knowledge, these are the first experiments using the PM-IRAS technique at elevated pressures to study NO dissociation on the Rh(111) surface.

NO Adsorption on Rh(111)

Fig. 13 shows infrared spectra obtained at various temperatures after dosing 300 L (1 x 10^{-6} Torr s) for 300 s. Note that NO saturation occurs between 15 and 20 L. To ensure cleanliness of the sample, after each spectrum was acquired, the sample was flashed to 1200 K. AES analysis has shown that this procedure yields a clean surface. As can be seen, NO exposure below 150 K leads to a single vibrational mode at 1652 cm^{-1}. This mode was also observed by HREELS [78] and assigned to NO bonding in 3-fold

hollow sites [88]. However, at approximately 150 K, a new feature appeared at 1848 cm^{-1}, corresponding to bonding at atop sites [78, 88]. With a further increase in the temperature, the intensity of this atop feature continued to increase, with a concomitant decrease in the hollow site feature. At 300 K, only the atop feature was evident. This change in the surface adsorption sites is common for CO adsorption on many metal surfaces with increasing CO coverages and also has been reported for NO adsorption [78]. However, at adsorption temperatures below 150 K, only one mode, corresponding to NO at 3-fold hollow sites, is evident over the entire NO coverage range. These results suggest that the change of the NO adsorption site may be an activated process and/or associated with the decomposition of NO at elevated temperatures.

Next, experiments were carried out to determine the time-dependent nature of the PM-IRA spectra (Fig. 14a). After exposing the Rh(111) surface to 20 L of NO (saturation coverage) at 250 K, spectra were acquired at 5 min intervals. The spectra are dominated by the 3-fold hollow feature at 1650 cm^{-1}, with a smaller feature at 1850 cm-1 related to atop NO. There are no apparent changes in the spectra after 25 min. However, a second 20 L of NO exposure (40 L total) leads to a noticeable change in the spectrum (Fig. 14b). In this spectrum, the intensity of the atop feature approaches that of the 3-fold hollow site. Further exposure leads to an atop feature intensity greater than that of the 3-fold hollow feature (Fig.14c). Apparently, the addition of NO is a prerequisite for NO to bind at atop sites.

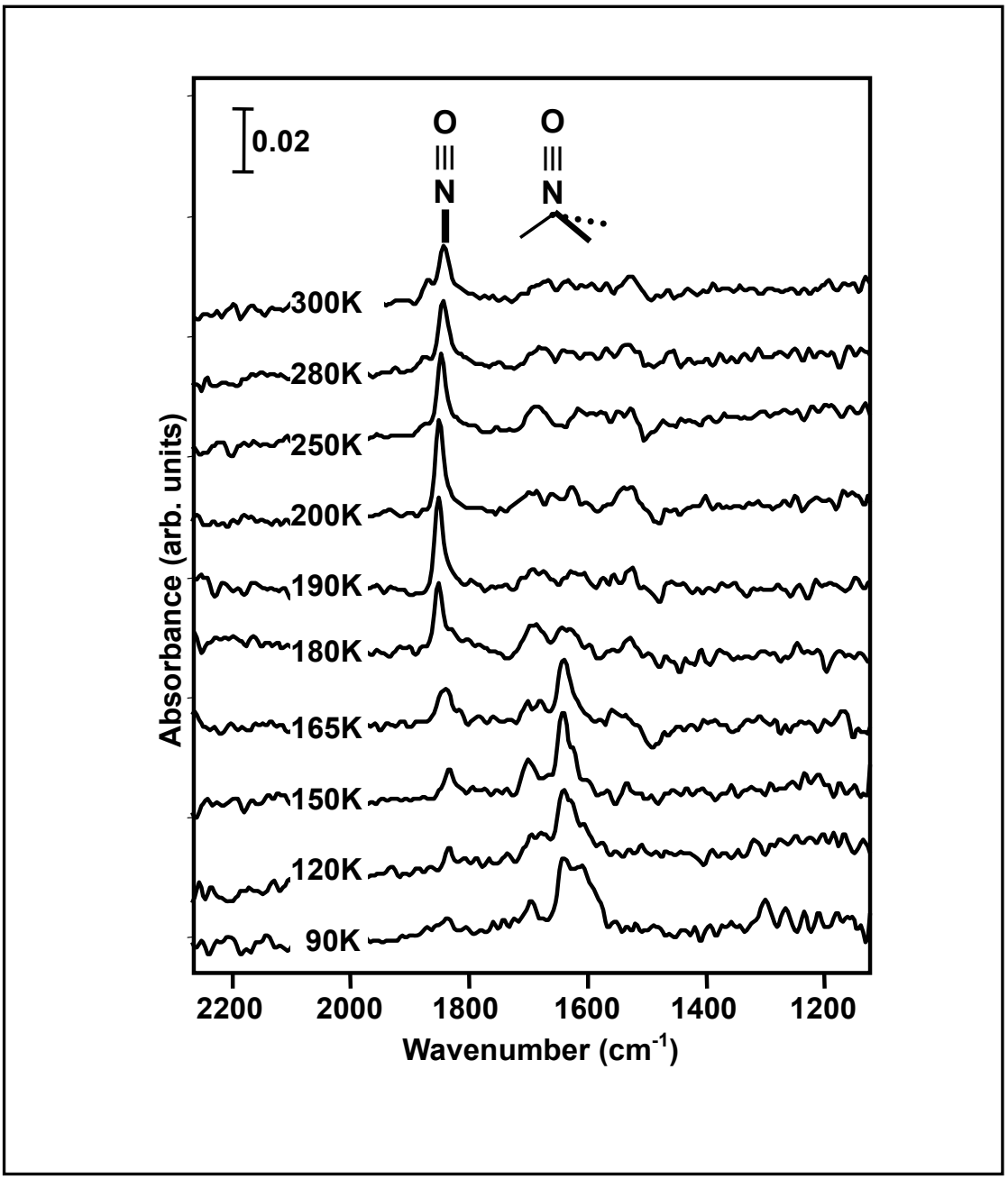

Fig. 13. Temperature-dependent PM-IRA spectra of NO on Rh(111). A total of 300 L NO was dosed at the indicated temperature, and then the infrared spectrum was acquired.

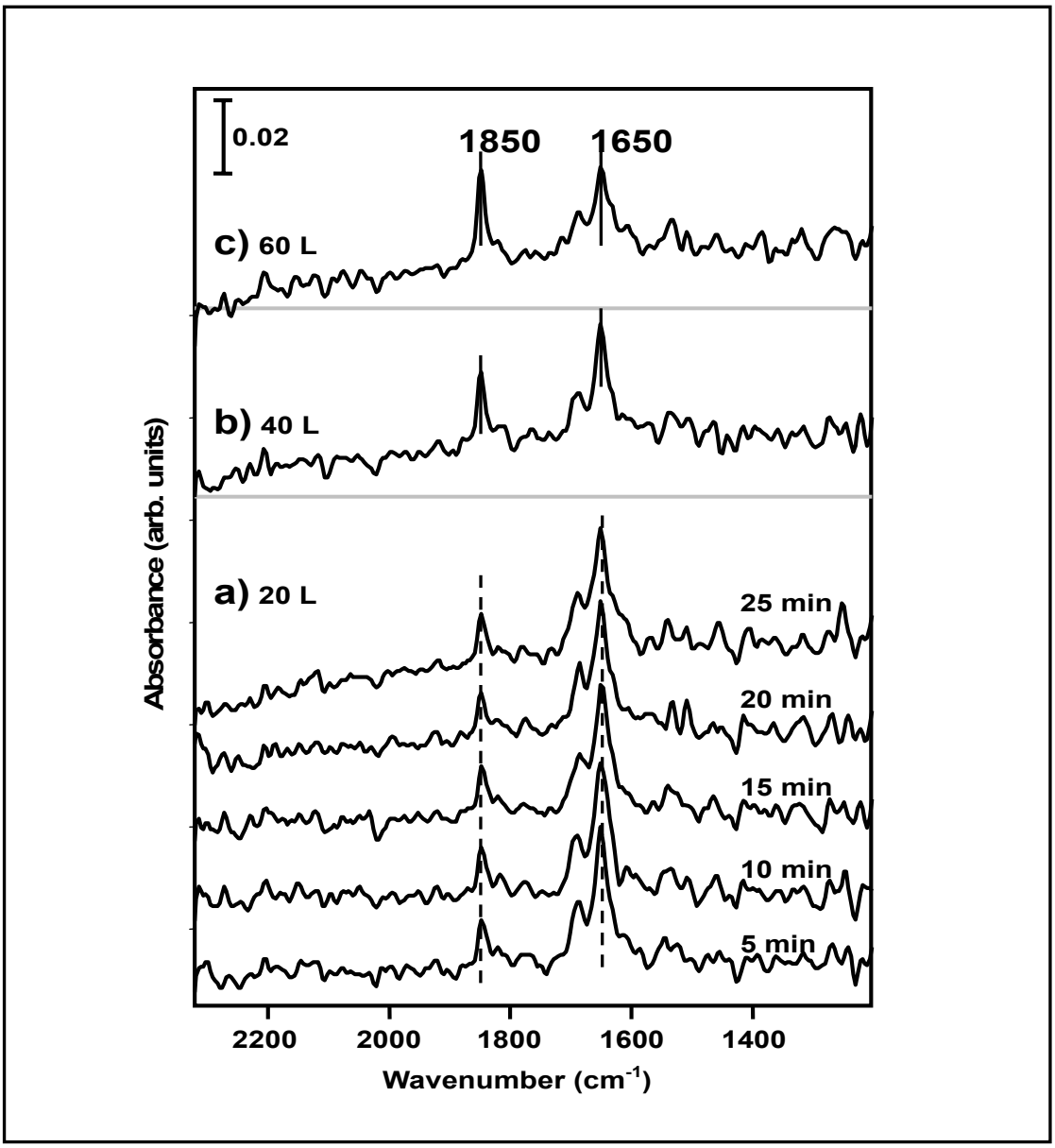

Fig. 14. PM-IRA spectra of NO on Rh(111) with different exposures. (a) 20 L of NO on the Rh(111) surface; (b) following a 20 L dose (40 L total) of NO to the surface of panel a; (c) following a final 20 L dose (60 L total) of NO to the surface of panel b.

Further time-dependent experiments were carried out at 250 K under flowing conditions of 5×10^{-8} Torr NO. The spectra in Fig. 15a are dominated initially by molecular NO binding at 3-fold hollow sites (1650 cm^{-1}). Bonding of NO at atop sites (1850 cm^{-1}) is also evident. However, with time, those features corresponding to 3-fold hollow sites disappear with the only significant feature in the spectrum being that due to molecular NO at atop sites. The changes in atop- and 3-fold hollow intensities as a function of time are summarized in Fig. 15b.

Spectra were also acquired at 120 K after exposing the sample to 1×10^{-7} Torr NO as shown in Fig. 16a. As expected at this temperature, 3-fold hollow bonding dominates the spectrum (Fig. 16 a1). With repeated flashing to 200 K in background NO (Fig. 16 a2 to a6), the atop feature grows, and the 3-fold hollow feature attenuates. These results are at odds with previous adsorption/dissociation mechanisms for NO on Rh(111) [66, 74, 80, 86] and offer further evidence that dissociation occurs at temperatures much lower than previously suggested. Note that similar experiments, where background NO is not present during the flash, lead to spectra where there is no change with respect to 3-fold hollow and atop bonding sites (Fig. 16b). These results confirm that migration from 3-fold hollow sites does not occur during a vacuum anneal and that the atop bonding seen in Fig. 16a is a result of the addition of gas-phase NO coadsorbed with NO decomposition species.

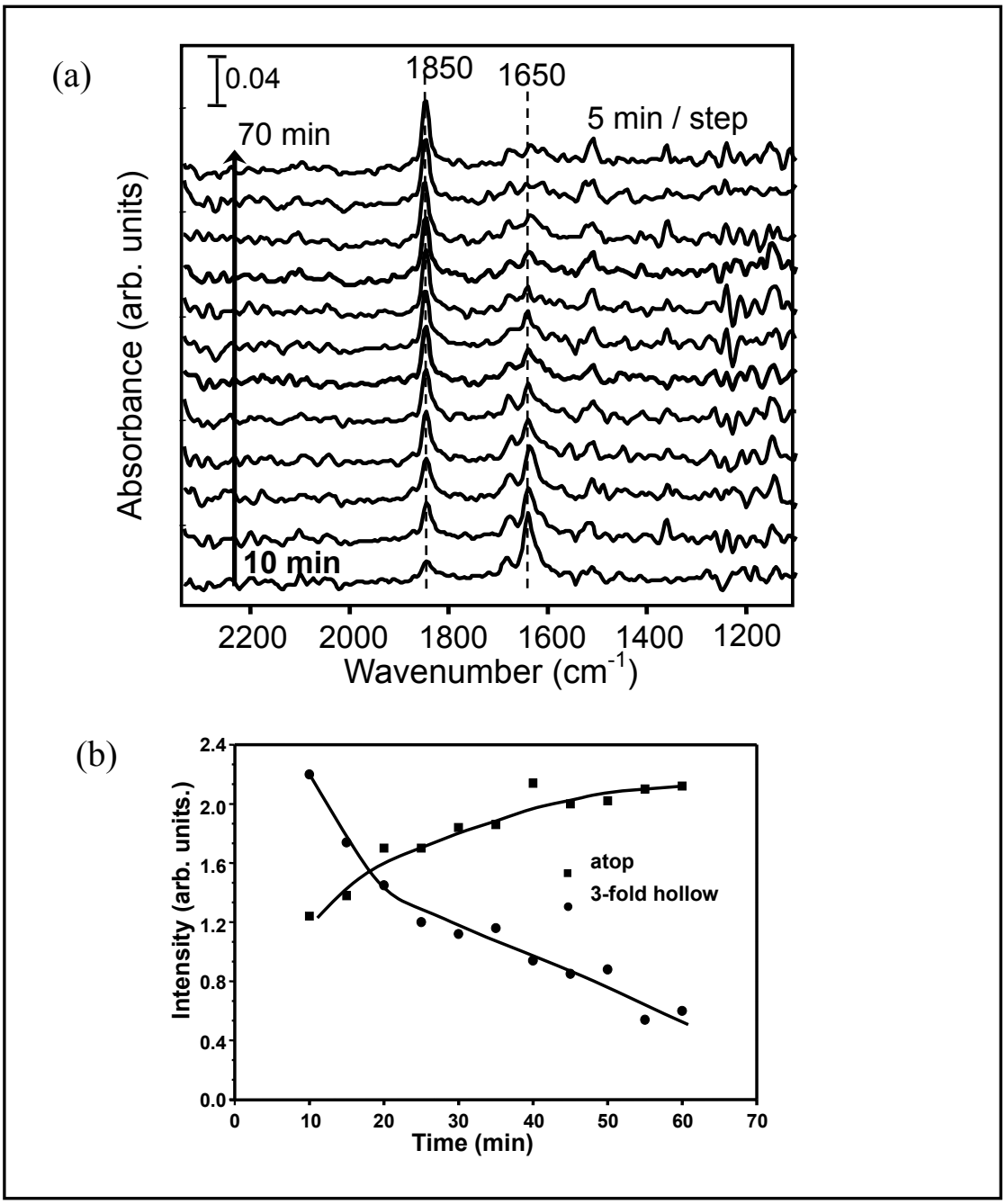

Fig. 15. Time-dependent NO adsorption at 250 K on Rh(111). (a) The corresponding PM-IRA spectra. (b) IR intensity of absorption in the atop and 3-fold hollow site from panel (a) as a function of time.

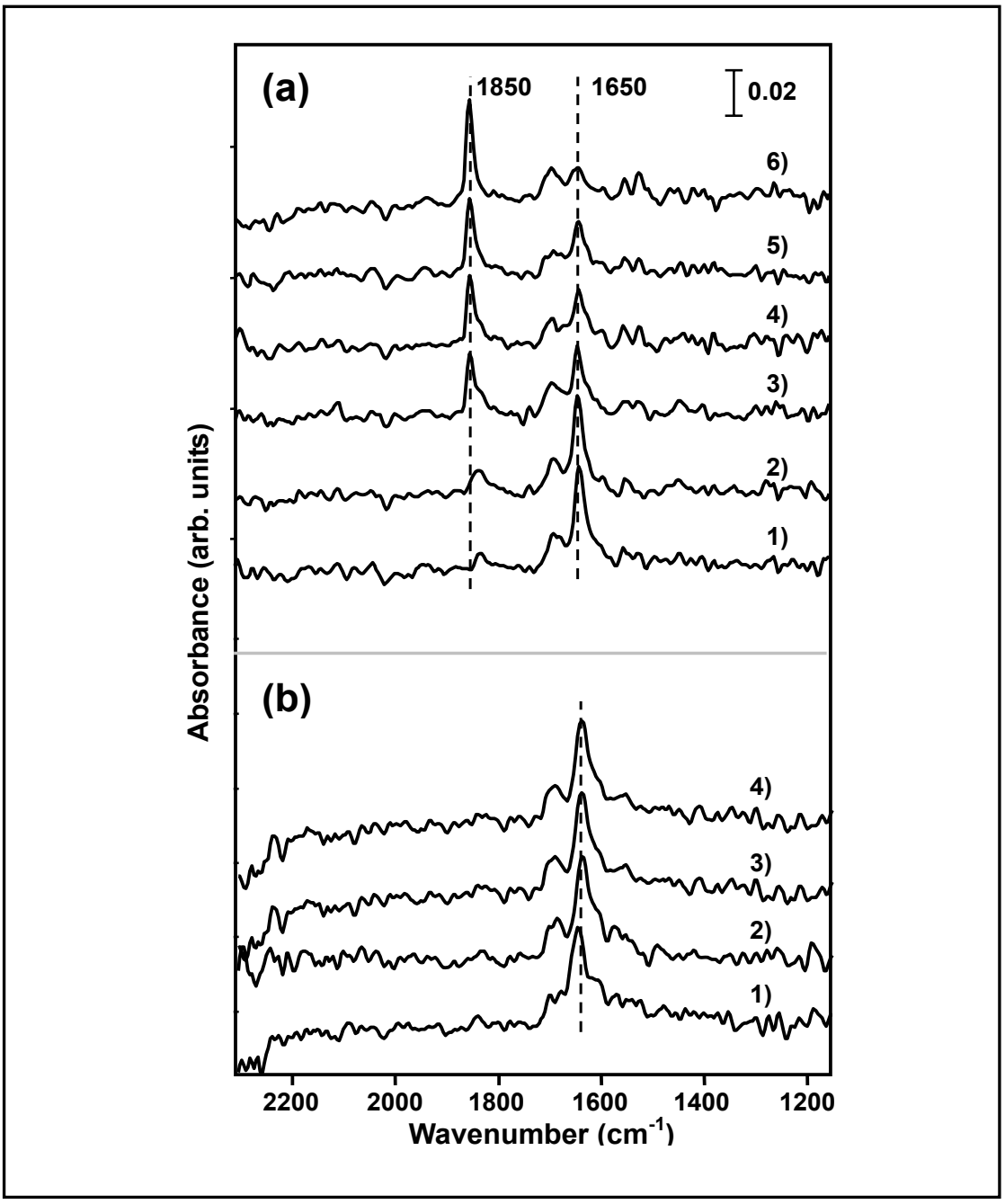

Fig. 16. PM-IRA spectra of NO adsorption on Rh(111) at 150 K. (a1 and b1) in 1×10^{-7} Torr NO. (a2 to a6) after flashing the sample to 200 K and cooling in 1×10^{-7} Torr NO. (b2 to a4) after flashing the sample to 200 K in vacuum.

As mentioned in the first section, at the coverages reported previously, it is assumed that NO bonds molecularly since dissociation is not observed below 275 K [66, 86]. However, our results show that NO bonding occurs only at atop sites with the 3-fold hollow site being occupied only at relatively low temperatures (i.e., <150 K (Fig. 16)). The complete shift of the NO modes exclusively from 3-fold hollow to atop (Fig. 13-16) cannot be explained based on the results and explanations previously reported (i.e., coverage-induced surface restructuring). The number of atop sites is identical to the 3-fold hollow sites, and also, NO prefers the 3-fold hollow sites at low NO coverage. These points suggest that dissociation of NO likely takes place below 200 K, much lower than the previous reported temperature of 275 K [66, 86]. The growth of the atop feature must result from the coadsorption of NO dissociation products that induces molecular NO at the atop site. Since the 3-fold hollow sites are filled with dissociation products (e.g. O_{ad}) as well as with molecular NO, incoming NO molecules are forced to adsorb at atop sites. Molecular NO is reported to desorb from the Rh(111) surface at approximately 400 K by TPD [66, 80], so desorption can be ruled out as a cause for the decrease in the hollow-related IRAS feature. The only other possibilities are the movement of NO from the hollow sites to the atop sites or the dissociation of the NO molecules adsorbed at the 3-fold hollow sites. It is unlikely that NO migrates from the hollow sites, as the time lapse experiments at 250 K show (Fig. 14a). Therefore, a plausible explanation is that the molecules in the hollow sites are dissociating and filling the hollow sites. The data of Fig. 14b, c support this conclusion, as further exposure of the surface to NO leads to the population of atop sites. This explanation is the only one

that can account for the changes seen in the spectra; however, it is at odds with all previous work, in which dissociation is inhibited at relative high NO coverages [66, 74, 80, 86].

NO Adsorption on O-Rh(111)

To examine how the NO dissociation products influence bonding, NO was dosed on an oxygen pretreated surface at 120 K (Fig. 17). On an oxygen-free surface, NO absorbed only at 3-fold hollow sites (Fig. 17a). However, on a surface pretreated with various amounts of oxygen (i.e., 2, 4, and 6 L at 650 K), atop NO adsorption was also observed, with the intensity increasing with an increase in the O_2 coverage and a concomitant decrease in the intensity of 3-fold hollow NO sites. These data confirm that surface oxygen leads to NO adsorption at atop sites, suggesting that NO and oxygen coexist in the same phase, in contrast to a previous proposal, based on STM data, that NO and oxygen form separate phases on the surface [73].

These data have important implications for understanding how NO interacts with Rh(111). Specifically, at room temperature or even below, the surface is essentially covered by atop NO, with very little 3-fold hollow site occupation. This contrasts with previous reports, particularly those surface adsorbate structures [75, 83, 84, 88] with at least a 2:1 ratio of atop/hollow or hollow/atop. Since NO dissociation has received considerable attention on this surface, it is surprising that the dissociation products, O_{ad} and N-containing species, have not been considered with respect to their influence on the structures of NO on Rh. Although the surface structure at room temperature is purported

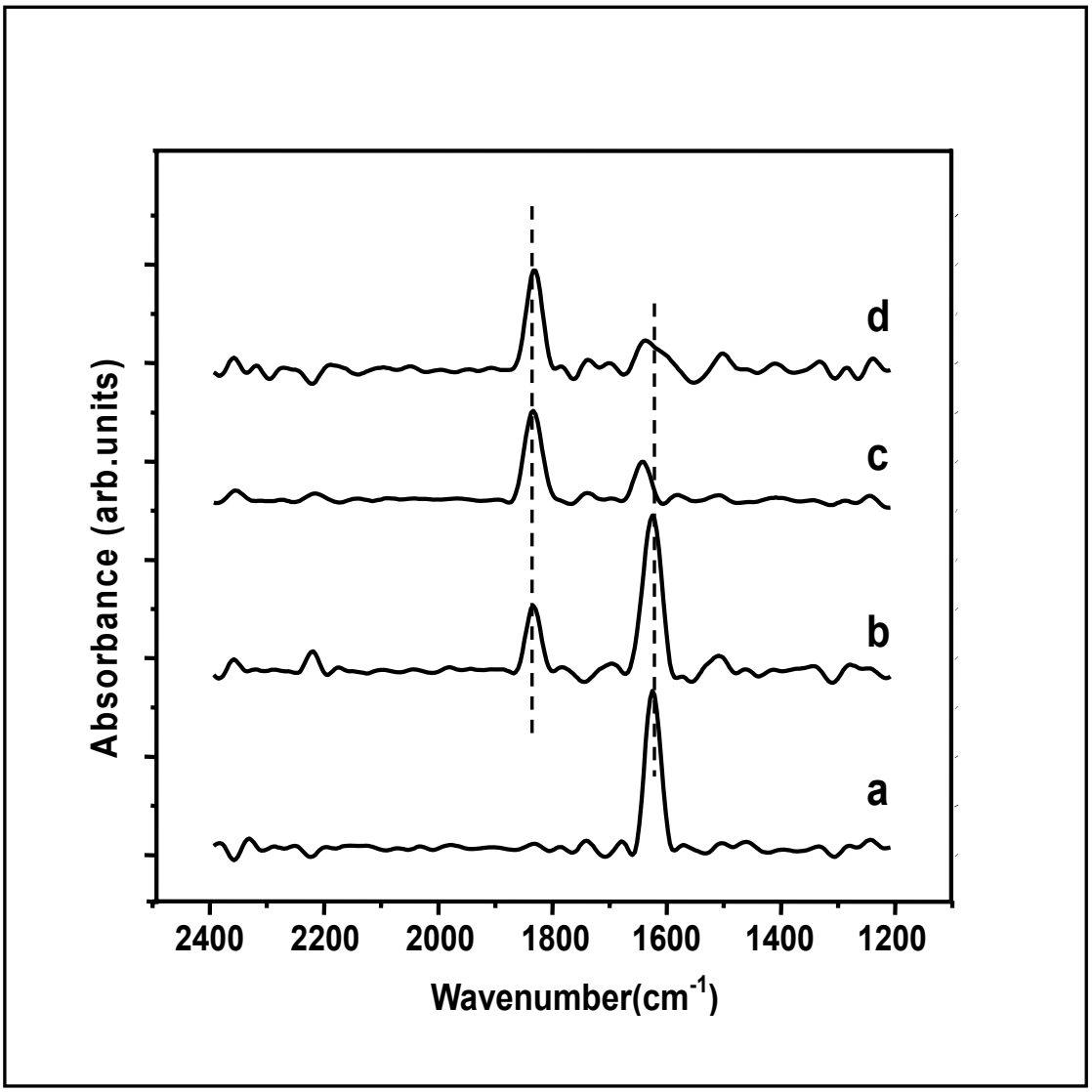

Fig. 17. NO (2 L) adsorption at 120 K on various oxygen pretreated Rh(111) surfaces. Various oxygen coverages were obtained by dosing: (a) 0 L of O_2; (b) 2 L of O_2; (c) 4 L of O_2; and (d) 6 L of O_2 at 650K.

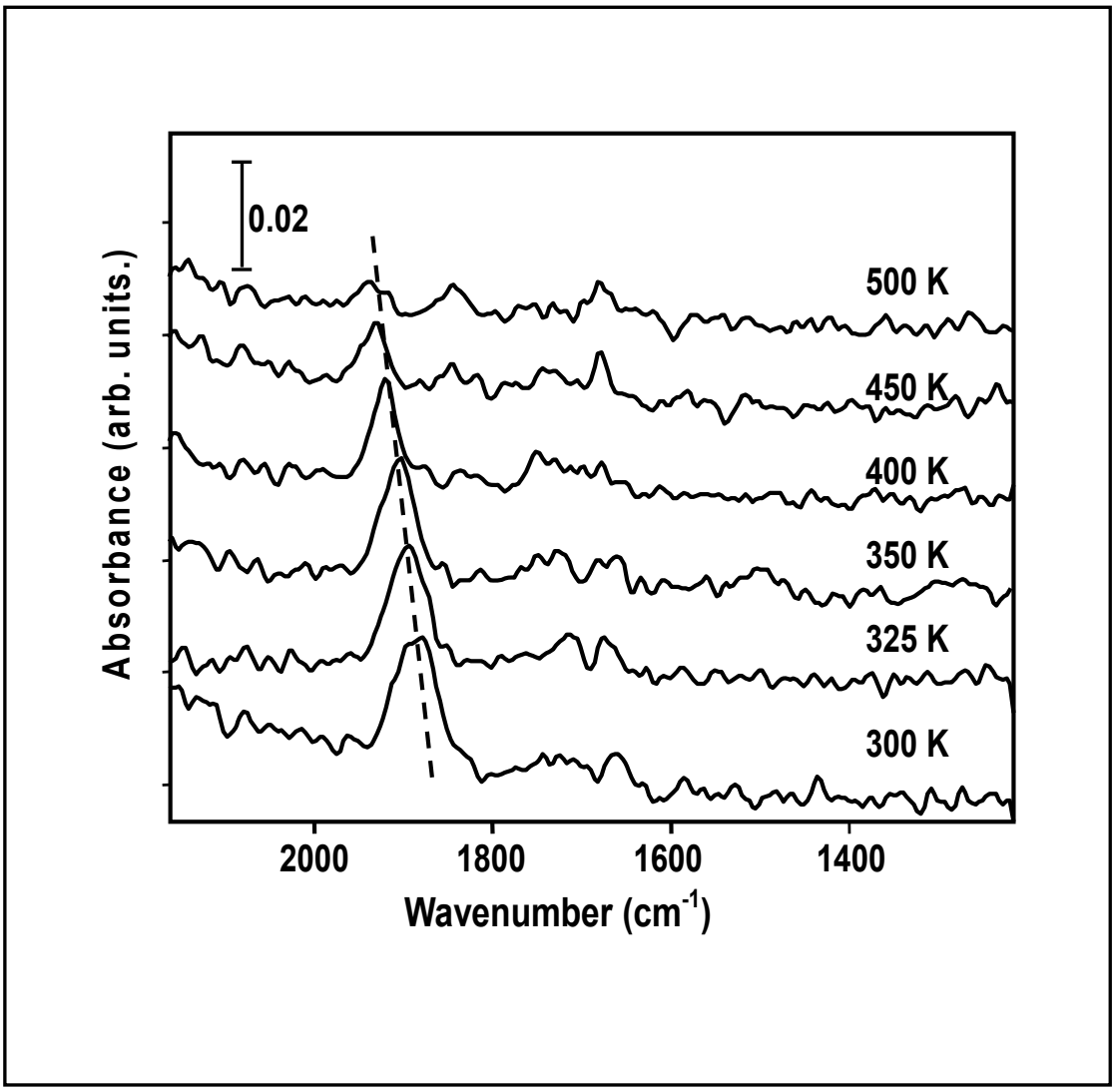

Fig. 18. PM-IRAS spectra obtained as a function of temperature in the presence of 1 Torr NO. The Rh(111) sample was exposed to 1 Torr NO at 300 K, and the temperature was then raised as indicated.

to change at elevated (~1 Torr) pressure [83], we note that our results for 1 Torr NO on Rh(111) show that the surface is essentially covered by atop NO (Fig. 18). The present study strongly suggests that further theoretical and experimental studies should be carried out to clarify the remaining discrepancies in this important adsorbate system.

CHAPTER IV

CHARACTERIZATION OF A COMPLEX MODEL CATALYST: $Au/TiO_x/Mo(112)$*

Highly dispersed Au particles have been shown to exhibit exceptional catalytic activity for several reactions [50, 95-99]. Of these, low temperature CO oxidation has received the most attention for understanding the origin of the exceptional reactivity of Au nanoparticles [50-52, 96, 97, 99-105]. It is generally accepted that the catalytic activity of Au depends to a large extent on the size of the Au particles; however other effects, such as the nature of the support, the Au-support interaction, the particle shape, and metal-support charge transfer, are proposed to be of fundamental importance. Based on kinetic studies and scanning tunneling microscopic (STM) study, the most active structures of supported Au particles have been shown to be two atomic layers in thickness (a bilayer) [50, 51] and to have distinctive electronic [106] and chemical properties [107, 108] compared to bulk Au. To further explore the properties of this bilayer thickness effect, two ordered Au films, a (1 × 1) monolayer and a (1 × 3) bilayer, were synthesized in our laboratory [52]. Specifically, these two films completely wet an ultrathin TiO_x film grown on Mo(112), i.e., TiO_x/Mo(112). Unprecedented catalytic activity for CO oxidation was observed on the Au bilayer film [52]. The PM-IRAS and ultraviolet photoemission spectroscopy (UPS) have been combined to study the

---

*Reprinted in part with permission from "On the Origin of the Unique Properties of Supported Au Nanoparticles" by M.S. Chen, Y. Cai, Z. Yan, D. W. Goodman, J. Am. Chem. Soc. 128 (2006) 6341, Copyright (2006) American Chemical Society.

electronic and chemical properties of the ordered Au films using CO as a probe.

Preparation of (1 × 1)- and (1 × 3)-Au Films on TiO_x/Mo(112)

A well-ordered ultra-imthin silica film was first prepared following the procedures in the literature [109]. In brief, clean Mo(112) substrate was first oxidized in 5×10^{-8} Torr O_2 at 850 K for 10 min to obtain a Mo(112)-*p*(2 × 3)-O surface. Less than 1 monolayer (ML) Si then was deposited onto the thus prepared surface, followed by an oxidation at 800 K in a 1×10^{-7} Torr O_2 for 5 min and the successive annealing at 1200 K for an additional 5 min. The above procedure (deposition/oxidation/annealing) was repeated until a constant Si/Mo AES ratio was achieved. The prepared surface was proved to be a well-ordered Mo(112)-*c*(2 × 2)–[SiO_4] structure.

The Mo(112)-(8 × 2)-TiO_x support was prepared by first depositing ~ 1 ML of Ti from a filament source onto the Mo(112)-*c*(2 × 2)-[SiO_4] surface followed by an oxidation at 800 K in 5×10^{-8} Torr O_2 for 10 min and thus a TiO_x film was formed on the silica film. The subsequent annealing at 1400 K in 5×10^{-8} Torr O_2 for 10 min causes the decomposition of silica film. The final step, an additional annealing at 1400 K in 1×10^{-8} O_2 for 5 min leads to the complete removal of the *c*(2 × 2)-[SiO_4] film and any residual Si [52, 110]. The detailed procedure is also illustrated in Fig. 19. The prepared TiO_x film exhibits a sharp (8 × 2) LEED pattern as shown in Fig. 20. The resulted TiO_x film yields a film with an identical Ti/Mo AES ratio corresponding to 1 ML. A possible structure for this film has been proposed [52, 110], where there are seven Ti atoms for every eight Mo atoms in the Mo(112) trough (the [-1-11] direction), with the Ti atoms bound to the

surface via Ti-O-Mo bonds and to each other via Ti-O-Ti linkages. A new single phonon feature at 84 meV in HREELS was observed [52]. This energy loss in this feature is between the one observed for bulk TiO_2 and the mode for three-dimensional TiO_2 clusters on Mo(112) surface. From the HREELS and XPS data, the oxidation state of Ti in the (8 × 2) film was deduced to be 3+ [52, 110].

Au was deposited onto the Mo(112)-(8 × 2)-TiO_x surface from an Au wire wrapped around a Ta filament that was heated resistively. The surface was then annealed at 900 K in O_2 of $<3 \times 10^{-9}$ Torr. The Au flux was calibrated using AES break points on Mo(112) and (8 × 2)-TiO_x/Mo(112) (see Fig. 21). The Au coverage is reported in monolayers (ML) and references to the top layer Mo atom density in Mo(112). Au on the TiO_x/Mo(112) grows epitaxially to 1.0 ML, forming a (1 × 1) monolayer at 1 ML, a (1 × 3) bilayer at 1.3 ML, then forms 3-D clusters at coverages > 1.3 ML. The order of the Au (1 × 1) and (1 × 3) structures were confirmed by sharp LEED patterns at Au coverages of ~1 and 1.3 ML, respectively (see Fig. 21)

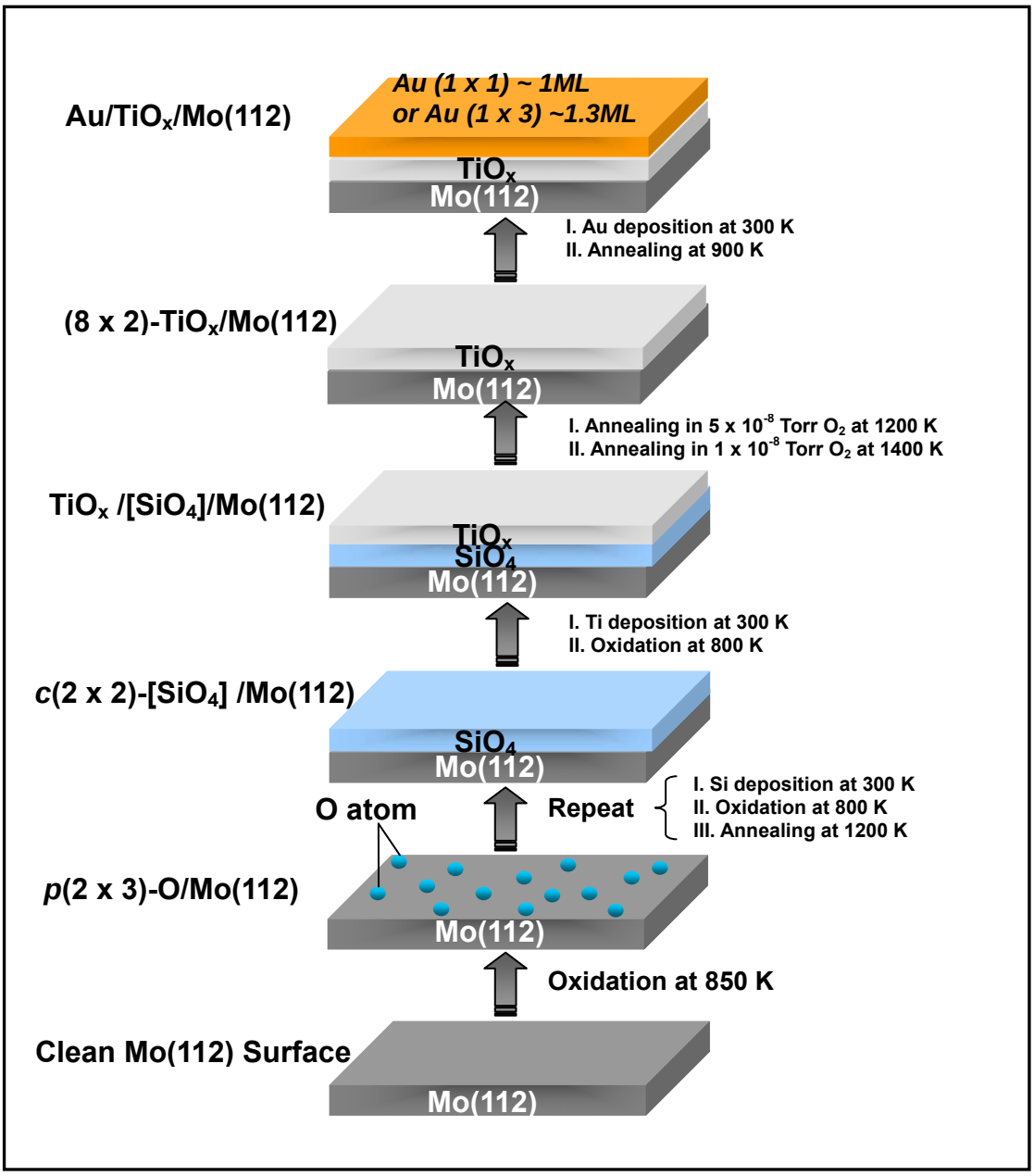

Fig. 19. Preparation procedure of $Au/TiO_x/Mo(112)$ model catalyst.

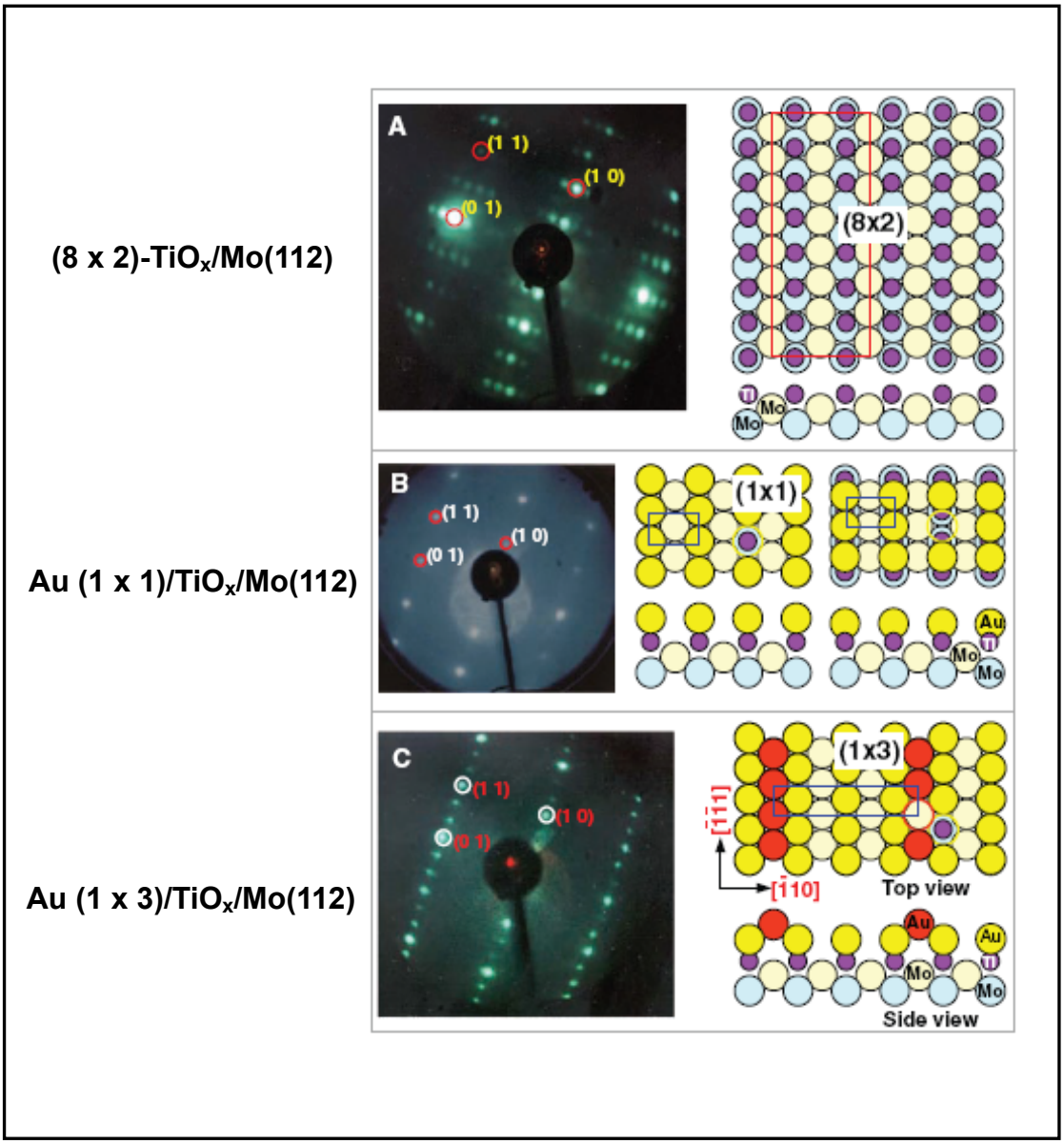

Fig. 20. LEED patterns and structure models. Top and side views for (A) the (8 × 2)-TiO_x/Mo(112); (B) the Au (1 × 1)/ TiO_x/Mo(112); (C) the Au (1 × 3)/ TiO_x/Mo(112); adapted from [52].

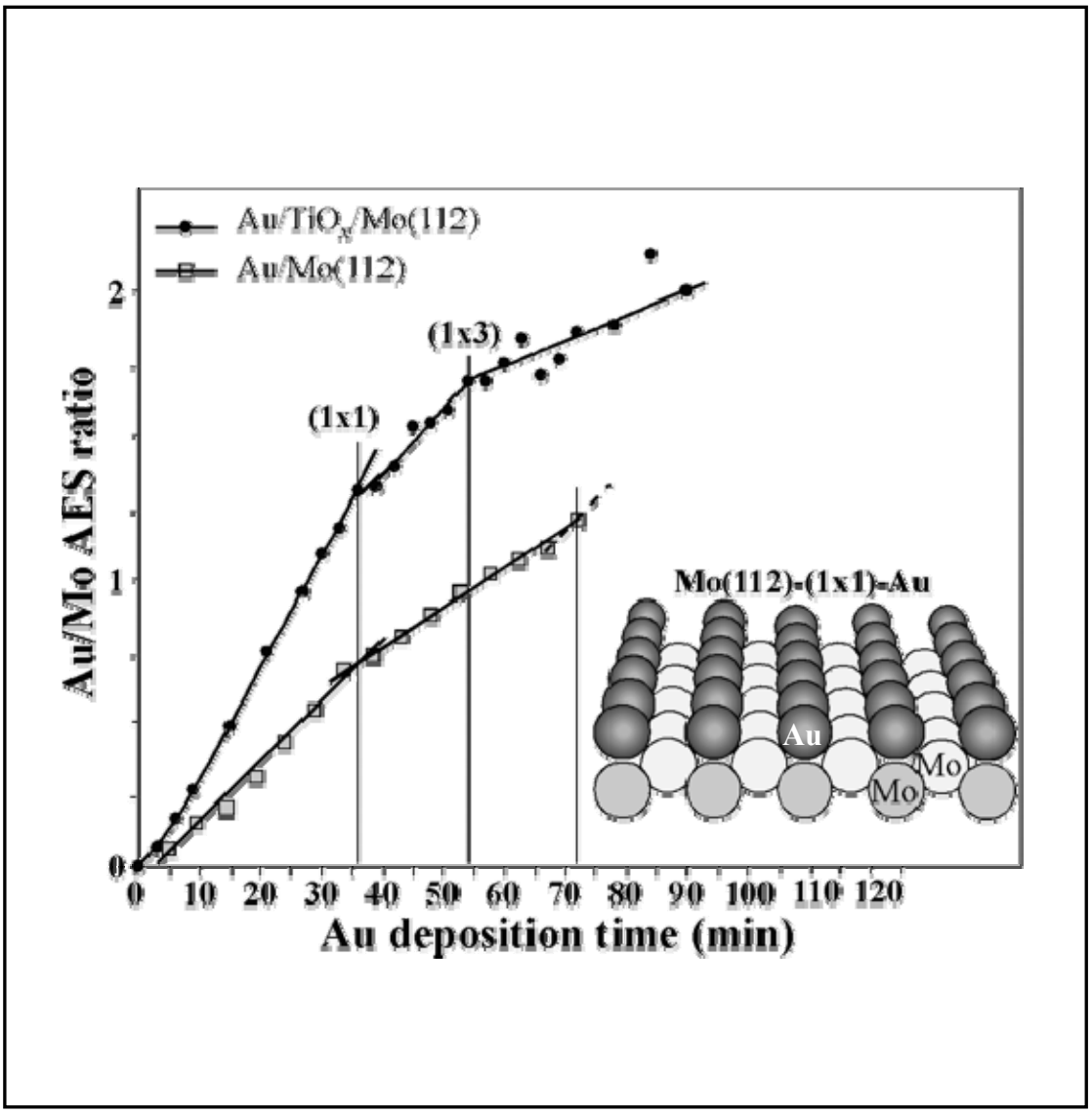

Fig. 21. Plot of Au/Mo AES ratios versus deposition time. The insert is a structural model of (1 × 1)-Au/Mo(112).

Electronic Properties of Catalytically Active Au

A number of theoretical and experimental studies have addressed the electronic properties of Au nanoparticles on oxide supports with the goal of understanding the unique properties of Au/TiO_2. Density functional theory (DFT) calculations suggest that the metal-support interaction alters the electronic structure of Au nanoclusters and promotes their catalytic activity for low-temperature CO oxidation [111]. In particular, defects on the oxide support are thought to play a key role in anchoring the Au particles and in transferring electron density to Au, with these two effects in combination contributing to the special catalytic activity [50, 104, 112-116]. Based on the shift of the Ti-O phonon mode in HREELS [52], Ti was proposed to be oxidized from 3+ in the (8 × 2)-TiO_x/Mo- (112) to 4+ in the (1 × 1) and (1 × 3)-Au/TiO_x/Mo(112) upon bonding to Au. Oxidation of Ti in the support upon deposition of Au implies the formation of $Au^{\delta-}$.

In this study the vibrational stretching mode (νCO) of adsorbed CO was used to investigate the nature of the electronic state of Au in ordered Au films on TiO_x. The νCO mode shifts to lower frequency on electron-rich Au clusters and to higher frequency on electron-deficient clusters relative to bulk Au with the extent of this shift having been shown to correlate with the cluster charge [117-119]. The shift to lower frequency of the νCO has been proposed to arise from enhanced back-donation from the Au cluster to the anti-bonding $2\pi^*$ orbital of CO [120]. CO adsorption was carried out at 90 K with various CO exposures on the (1 × 1)-Au/TiO_x/Mo(112) surface and compared to the corresponding data for 1 ML Au on Mo(112) and 8 ML Au on Mo(112), hereafter referred to as (1 × 1)-Au/Mo(112) and Au(8 ML)/Mo(112), respectively (Fig. 22).

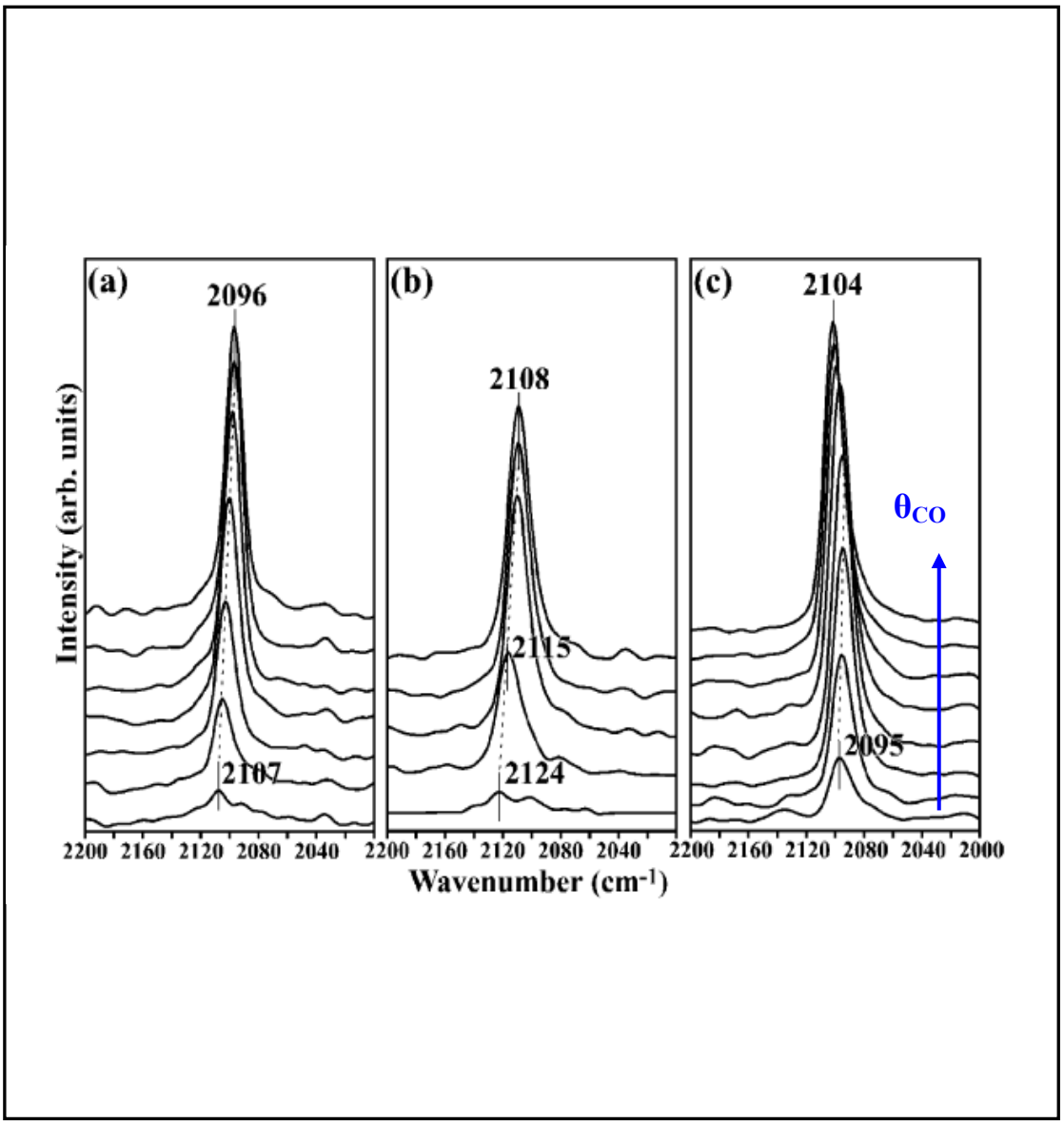

Fig. 22. PM-IRA spectra of CO adsorption on various Au surface as a function of CO exposure at 90K. (a) (1 × 1)-Au/TiO_s/Mo(112); (b) Au (8 ML)/Mo(112); (c) (1 × 1)-Au/Mo(112).

.

Note that at coverages near 1 ML, Au on Mo(112) forms a (1 × 1) surface structure (see the insert of Fig. 21) as deduced from the sharp LEED pattern. The arrangement of Au atoms in (1 × 1)-Au/Mo(112) is identical to the structure of Au in a (1 × 1)-Au/TiO_x/Mo(112) surface [52], with the exception that in the former, Au binds directly to the substrate Mo while in the latter, Au binds to the substrate through Ti. For low coverages of CO adsorbed on (1 × 1)-Au/ TiO_x/Mo(112), a single νCO mode corresponding to CO on atop Au atom was observed at ~2107 cm^{-1} (Fig. 22a). This feature red-shifts to 2096 cm^{-1} as the CO coverage is increased to saturation, as seen with increasing CO coverage on Cu, Ag, and Au surfaces [121, 122]. This red-shift is thought to occur because of limited back-donation from the Au d states into the 2π* orbital of CO, with the Au-CO bonding occurring primarily through 5σ donation from CO to Au. A decrease in the extent of the 5σ donation to Au with increasing CO coverage leads to a red-shift in the CO mode [108, 122-124]. As shown in Fig. 22b, for CO adsorbed on multilayer Au, e.g., Au(8 ML)/Mo(112), the νCO mode red-shifts from 2124 to 2108 cm^{-1} with increasing CO coverage. In contrast, on (1 × 1)-Au/Mo(112), the νCO mode remains essentially constant at 2095 cm^{-1} from low to relatively high (~90%) CO coverages, finally blue-shifting to 2104 cm^{-1} at saturation. This blue-shift on (1 × 1)-Au/Mo(112) suggests more extensive back-donation exists between the Au d levels and the CO 2π* anti-orbital, compared to bulk Au, which is consistent with a strong interaction between Au and the Mo substrate, and in agreement with previous UPS results for Au on Mo(110) [125].

The νCO frequency at low CO coverages then can be used to qualitatively

estimate the charge on Au. As shown in Fig. 22, the νCO frequencies occur at ~2107, 2124, and 2095 cm^{-1} for low CO exposures on the (1 × 1)-Au/TiO_x/Mo(112), Au(8 ML)/Mo(112), and (1 × 1)-Au/Mo(112), respectively. These νCO frequencies indicate that the Au films on TiO_x/Mo(112) are electron-rich and that the extent of electron transfer from the substrate to the Au is less than the electron transfer to Au in (1 × 1)-Au/Mo(112). The extent of the charge transfer has been estimated to be ~0.08 e from a Mo substrate to Au in Au/Mo(110) [125]. Such charge transfer has been shown to be important in the bonding between dissimilar metals and to lead to relatively large perturbations of the metal electronic and chemical properties [126, 127]. Furthermore, the differences between the frequency shifts as a function of CO coverage for (1 × 1)-Au/TiO_x/Mo(112) and (1 × 1)-Au/Mo(112) also suggest very little rehybridization of Au or charge transfer between Au and the Mo substrate in (1 × 1)-Au/TiO_x/Mo(112). This is likely a consequence of the absence of direct bonding between Au and Mo in (1 × 1)-Au/TiO_x/Mo(112), in contrast to (1 × 1)-Au/Mo(112). The electron-rich nature of supported Au nanoparticles is supported by theoretical calculations [112, 113] and ancillary experimental data [50, 114, 116]. Electron-rich Au nanoparticles are predicted to adsorb dioxygen more strongly and to activate the O-O bond via charge transfer from Au to form a superoxolike species [128], as well as to facilitate the activation of CO [104, 112, 113, 115]

The electronic properties of these Au films were also investigated by UPS in this group [129]. It was found that upon deposition of Au, new valence band features appear at 4~5 and ~7 eV, corresponding to the Au $5d_{5/2}$ and Au $5d_{3/2}$ states, respectively,

increasing in intensity with increasing Au coverage. Moreover, with increasing Au coverage, the $5d_{5/2}$ feature moves slightly toward the Fermi edge, while the $5d_{3/2}$ feature remains essentially unchanged. The significant difference in the valence band spectrum for $Au/TiO_x/Mo(112)$, compared with bulk Au, indicates a strong redistribution of the Au 5d valence states in the formation of Au thin films on the oxide surface.

Chemical Properties of Catalytically Active Au

The upper panel in Fig. 23 shows a plot of the IR intensity of the CO feature versus CO pressure, where saturation of the IRAS signal corresponds to a saturation coverage of CO. The maximum intensity is assumed to correspond to one monolayer CO coverage. The expression for a Langmuir isotherm (see insert of Fig. 23) assumes non-dissociative adsorption, a fixed number of adsorption sites, and an adsorption enthalpy independent of the coverage. The constant, b, in the expression is dependent on temperature (T) and the enthalpy/heat of adsorption (ΔHads), i.e., b is proportional to $\exp(\Delta H\text{ads}/RT)$. Based on the Langmuir isotherm expression, the behavior indicated by the arrow in Fig. 23 reflects an increase in b, corresponding either to an increase in the heat of adsorption at a given temperature or to a decrease in the temperature for a fixed set of adsorption conditions. The data in Fig. 23 demonstrate that the order of the heats of adsorption for CO is (1×1)-$Au/Mo(112) > (1 \times 1)$-$Au/TiO_x/Mo(112) >$ Au(8 ML)/Mo(112). This sequence is consistent with the shift of the observed νCO (see Fig. 22) and also with electron-rich Au.

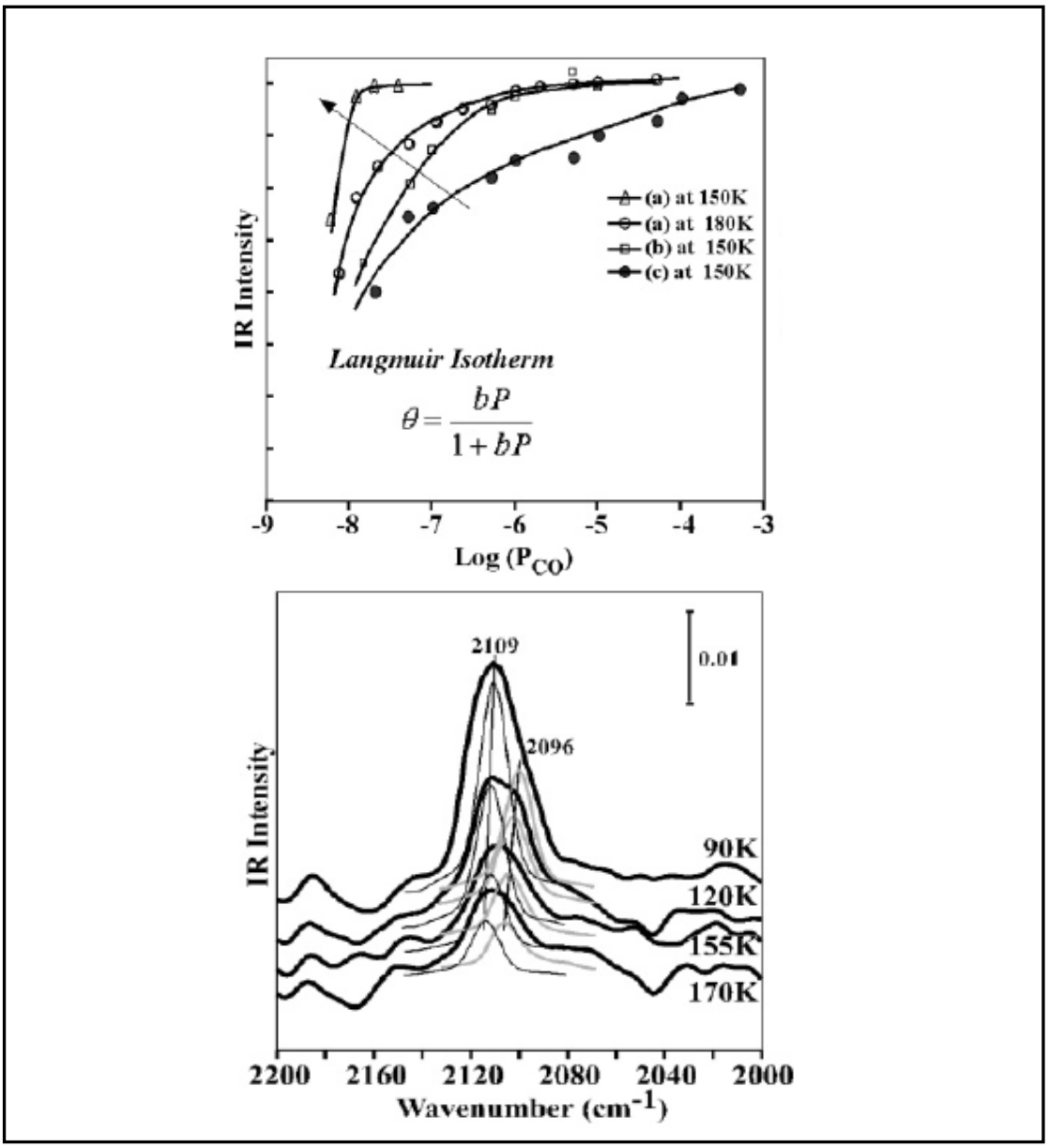

Fig. 23. CO adsorptions on various Au catalysts. (Upper panel) Isotherms from PM-IRAS data of CO (from bottom to top) of (a) (1 × 1)-Au/Mo(112), (b) (1 × 1)-Au/TiO_x/Mo(112), and (c) Au(8 ML)/Mo(112). The insert is an expression for a Langmuir isotherm. (Bottom panel) PM-IRAS of CO on a (1 × 3)-Au/TiO_x/Mo(112) bilayer at various temperatures.

In (1 × 3)-Au/TiO_x/Mo(112) [52], both layers of Au are accessible to the adsorbate. CO adsorbed on this surface at 90 K yields a broad feature at ~2109 cm^{-1} (see Fig. 23b) that can be qualitatively decomposed into two features: one high frequency feature, assigned to atop CO bonded to the topmost Au atoms, and one low frequency feature, assigned to CO bonded to the bottom layer Au atoms. Upon warming the sample to 120, then to 155, and finally to 170 K, the IR intensity of the mode corresponding to CO adsorbed on the topmost layer decreases more rapidly than that for the bottom layer. These results indicate that CO binds more tightly to the bottom Au layer than to the topmost Au layer.

Note that the top and bottom layers of Au atoms in the (1 ×3) bilayer are all accessible to the reactants. The interaction of the first-layer Au with Ti^{3+} of the support resulting electron rich in Au, which in turns facilitates the activation of oxygen. While the second Au layer exhibits low coordination geometry, which has been proposed to play a key role in defining the catalytic activity of Au nanoparticles [104, 123]. Thus, it is apparent that a combination of the first- and second- layer Au sites is crucial in the promotion of catalytic activity.

CHAPTER V

CO ADSORPTION AND OXIDATION ON Rh(111)

As discussed in Chapter I, although CO oxidation is one of the most thoroughly studied reactions, there are still doubts about its mechanism, particularly under high pressures and oxygen rich conditions. Moreover, in the literature, there is not much data available on single crystal surface characterization under technical reaction conditions. In this paper, CO oxidation reactions were performed on Rh, Pd, and Pt single crystals over a wide pressure range ($P_{CO} = 10^{-8}$ to 8.0 Torr) and various O_2/CO ratios (1/2 to 20/1). Surface phase evolution was monitored by in situ PM-IRAS experiments. The kinetic measurements were conducted simultaneously to explore the reaction mechanism in a full pressure range. In this chapter, CO oxidation on Rh(111) is elucidated in detail. Chapter VI focuses on the studies on Pd single crystals and Pt(110).

This chapter starts with the work of CO adsorption on Rh(111), followed by investigations of CO oxidation. Low pressure experiments are presented first, before the discussion on high pressure experiments. For brevity, only the results on 10^{-7} Torr of CO partial pressure are discussed in detail. Other results are briefly summarized. As explained in the experimental setup section, the CO_2 signal monitored by mass spectrometer was used to measure the CO_2 formation rate in the low pressure CO oxidation experiments. Experiments in 8 Torr of CO partial pressure are discussed with respect to high pressure reactions. Total pressure change over reaction time was measured to calculate the reaction rate in the high pressure experiments.

CO Adsorption on Rh(111)

Various techniques, such as LEED [130-133], HREELS [130, 131], TPD [130, 131, 134], XPS [132, 134], HRCLS [132, 133] et al., and DFT calculations [135] have been used to study CO adsorption on Rh(111) under UHV conditions. IRAS investigations have also been reported by Schennach [135] and Fujitani [134] in 2006. Several different CO overlayer structures were observed with respect to CO coverage (θ_{CO}). Among all reported CO overlayer structures, ($\sqrt{3} \times \sqrt{3}$) R30^o (Fig. 24a) at θ_{CO} = 0.33 ML (1 ML, θ_{CO} = 1, is defined as one CO molecule per surface Rh atom.), and (2 × 2)-3CO (Fig. 24b) at θ_{CO} = 0.75 ML, a saturation coverage under UHV conditions, were observed in all the investigations. It was found that at $\theta_{CO} \leq$ 0.33 ML, CO only adsorbs on atop sites; and the intensity of the atop feature in the vibrational spectrum reaches a maximum at $\theta_{CO} \sim$ 0.37 ML. A further increase of CO coverage leads to the adsorption on three-fold hollow sites, accompanied by the emergence of a low temperature desorption feature in the TPD spectrum. The adsorption on three-fold hollow sites becomes more evident at $\theta_{CO} >$ 0.5 ML, the vibrational feature of which is more pronounced in HREELS spectra [131] than in IRA spectra [134, 135]. It was found that the population on three-fold hollow sites hinders the adsorption on atop sites, and some adsorption on atop sites converts to three-fold hollow sites as well. Consequently, the intensity of the atop vibrational feature decreases with the appearance of adsorption feature on three-fold hollow sites.

It is well known that the CO stretching vibrational frequency shifts considerably with increasing CO coverage on Rh(111). The CO stretching frequency of atop

adsorption was observed at 2015 cm^{-1} [131] at θ_{CO} = 0.04 ML, and reaches 2070 cm^{-1} (HREELS) [131] or 2067 cm^{-1} (IRAS) [134] at saturation coverage (θ_{CO} = 0.75 ML). The correlation between vibrational frequencies and CO coverages is also summarized in Table 1. Such shifts reflect the interactions between the adsorbed molecules due to dipole-dipole coupling and/or chemical effects. The studies of isotopic mixtures of ^{12}CO and ^{13}CO on Rh(111) [131] showed that the dipole-dipole coupling accounts for the frequency shifts at $\theta_{CO} < 0.5$ ML, whereas the chemical effect caused by adsorption on neighboring sites adds the contribution at $\theta_{CO} > 0.5$ ML with the population on three-fold hollow sites. CO stretching frequency correlates strongly with the coverage of CO on Rh(111). CO coverage, in turn, can be estimated from the vibrational frequency of CO. Since the IRAS peak intensity of CO on three-fold hollow sites is significantly low compared with that on atop sites, the atop feature will be the focus in the following paragraphs in the discussion of CO coverages on Rh(111).

CO adsorptions at ambient pressures on Rh(111) [12] were reported by SFG and STM studies with the pressure ranging from 10^{-7} to 700 Torr. In these studies, at pressures up to 100 Torr, CO adsorption spectra exhibit identical adsorption features to that under UHV conditions, i.e., no new CO overlayer structures are observed.

CO adsorption plays a key role in the CO oxidation reaction. It is necessary to study CO adsorption, especially at ambient pressures, to assist with the understanding of CO oxidation reaction mechanisms. In the following paragraphs, PM-IRAS studies of CO adsorption on Rh (111) under CO pressures ranging from 10^{-8} to 1.0 Torr are presented.

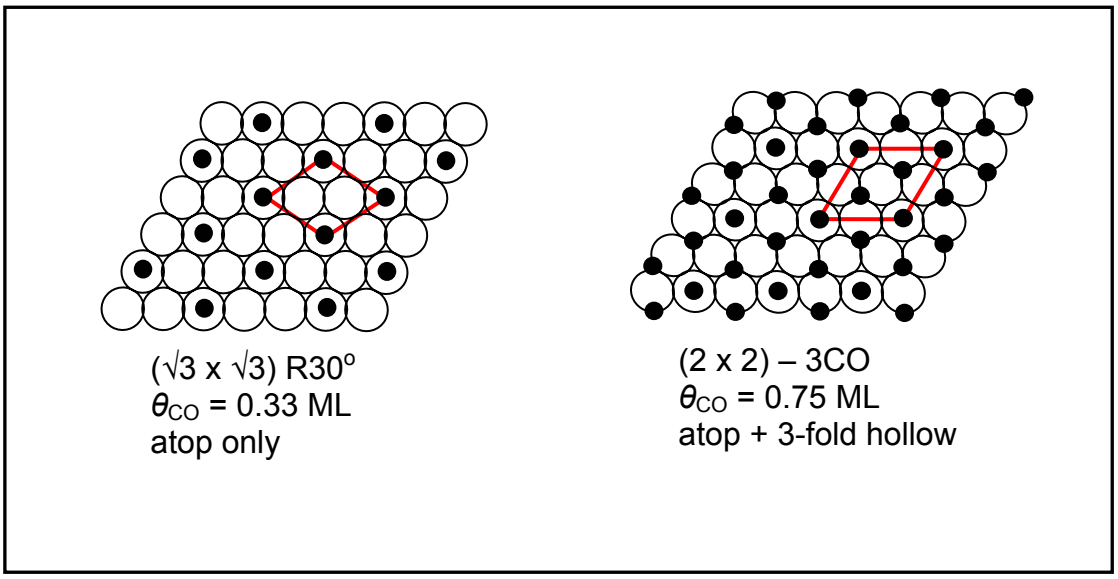

Fig. 24. Structure of CO overlayer on Rh(111) at the coverage of 0.33 and 0.75 ML.

Table 1

CO adsorption on Rh(111) at various coverages

θ_{CO} (ML)	Adsorption Site	ν_{CO} (cm^{-1})	CO overlayer Structure	Reference
0.04	atop	2015		[131]
0.33	atop	2041	$(\sqrt{3} \times \sqrt{3})R30^{o}$	[131, 136]
0.37	atop	2050		[135]
0.75	Atop + 3-fold hollow	2070, 1861	(2 × 2)-3CO	[130, 131, 136]

Low-pressure CO adsorption on Rh(111)

Fig. 25 displays the PM-IRA spectra of CO adsorption on Rh(111) acquired at various temperatures in a pressure of 1.0×10^{-7} Torr. The corresponding vibrational frequency and integrated peak area of the atop feature as a function of sample temperature are also illustrated in Figs. b and c, respectively. At 320 K, the atop adsorption feature was observed at 2060 cm^{-1}, indicating that the CO coverage is close to 0.6 ML. At that coverage, CO starts to adsorb on three-fold hollow sites as well. The adsorption on three-fold hollow site can be inferred from the evolution of the peak area of the atop-CO feature (see Fig. 25b). With an increase in the sample temperature, the atop peak area first increases and then remains constant, followed by a substantial drop in intensity when the temperature was above 440 K. The corresponding vibrational frequency (Fig. 25c) also continuously shifts to lower wavenumbers. In addition, at temperatures above 440 K, the red-shift of the vibrational frequency is enhanced. The change of the slope of the frequency shift suggests the conversion of CO overlayer structures on Rh(111). Moreover, the atop CO stretching frequency at 440 K in Fig. 25a was 2038 cm^{-1}, which corresponds to a coverage of 0.36 ML as measured in reference [131], a coverage above which a second peak emerges in the CO TPD spectrum.

CO adsorptions on Rh(111) with pressures of 1.0×10^{-6}, 1.0×10^{-5}, and 1.0×10^{-4} Torr were also conducted. Fig. 26 shows the vibrational frequency of the atop feature as a function of temperature at various CO pressures. All the curves follow the trend that atop-CO features red-shift with an increase in temperature. In addition, as indicated by the data, the shift of the frequency is greatly enhanced with temperature from the

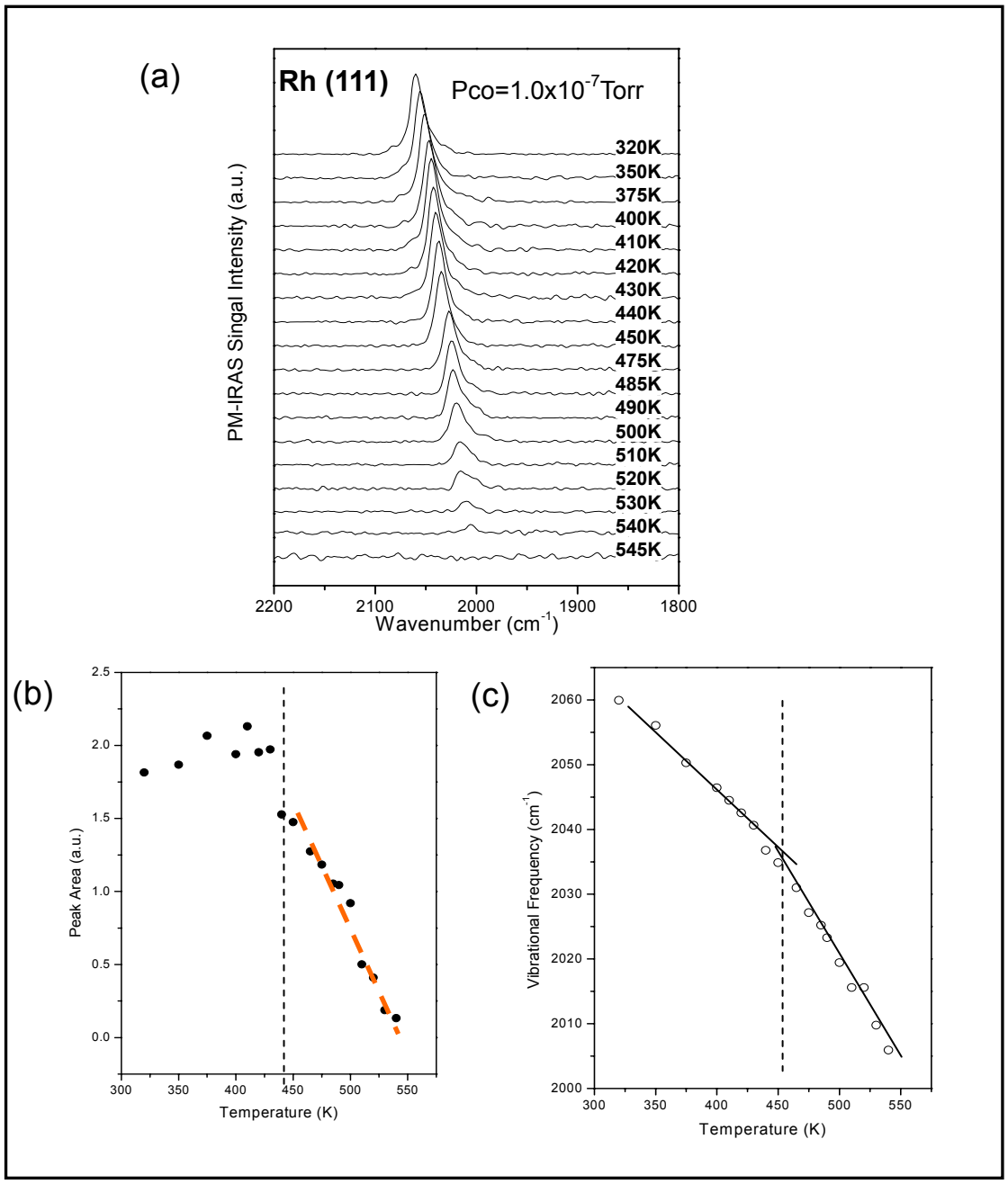

Fig. 25. Adsorption of1.0×10^{-7} Torr of CO on Rh(111). (a) PM-IRA spectra at various temperatures. Sample temperatures are marked adjacent to each spectrum; (b) integrated peak area of atop feature; (c) vibrational frequency as a function of sample temperature.

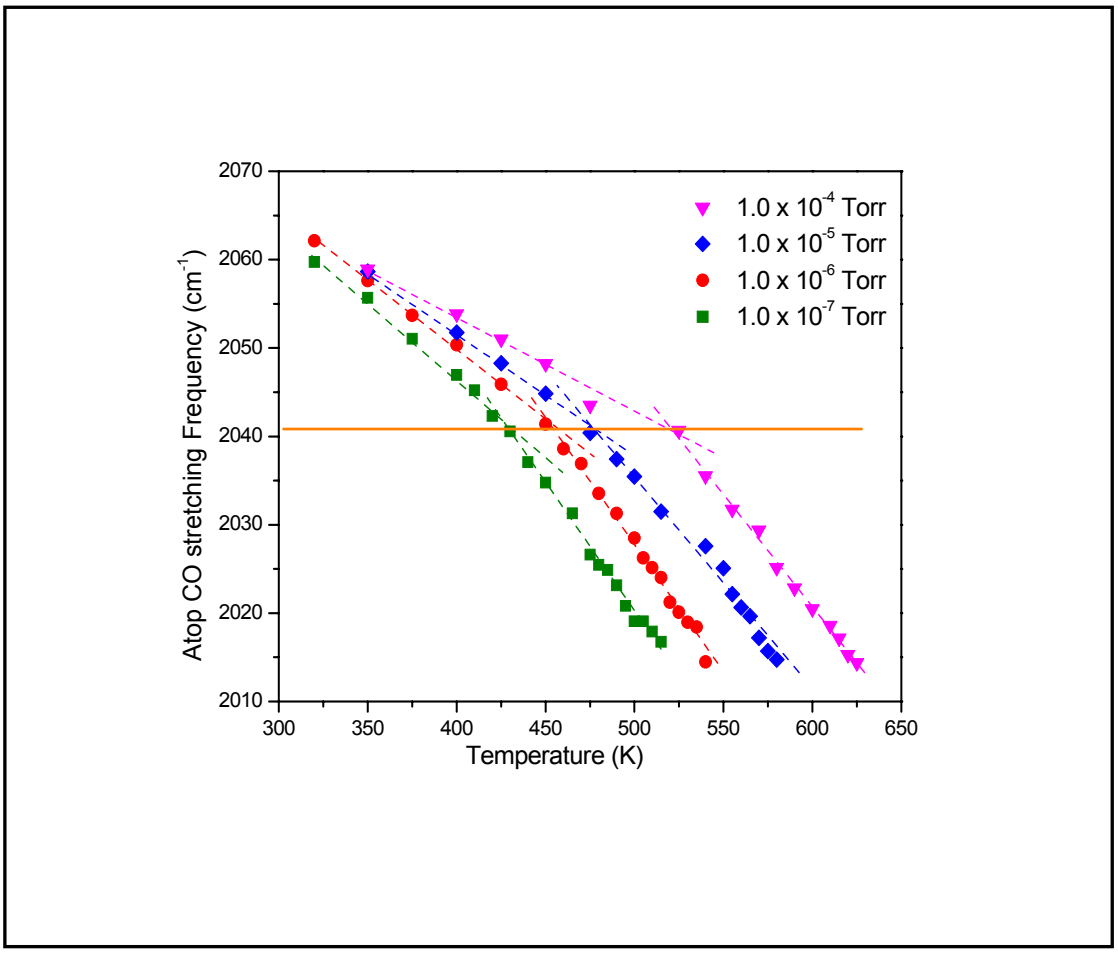

Fig. 26. Vibrational frequency of low pressure CO adsorption on Rh(111) as a function of sample temperature. CO pressures are as indicated.

vibrational feature of CO at ~ 2040 cm^{-1} at all CO pressures. Such behavior implies the formation of the same overlayer structure at the turning point, that is, the completion of the ($\sqrt{3} \times \sqrt{3}$) $R30^{o}$ structure corresponding to a CO coverage of 0.33 ML.

1 Torr CO adsorption on Rh(111)

Fig. 27 shows PM-IRA spectra as a function of temperature on Rh(111) in the presence of 1.0 Torr CO. At 350 K, atop-CO feature at 2066 cm^{-1} was observed, accompanied by a small and broad peak at ~1886 cm^{-1}, which indicates the CO coverage is close to 0.75 ML. From 350 to 650 K, the vibrational frequency of the atop feature decreases monotonously. The peak area initially increases and then remains constant. Nevertheless the peak width does not change significantly. However, as the temperature increases to above 700 K, the atop feature decreases considerably in intensity; meanwhile, the peak becomes broader. Such changes in atop adsorptions indicate the desorption of CO and the disorderliness of the CO overlayer. At 775 K, the CO stretching vibration frequency at 2016 cm^{-1} suggests the CO coverage is ~0.04 ML. At 800 K, CO could barely be detected. The temperature-dependent evolution of the spectra (Fig. 27a) showed the same trend as that at low pressures. This indicates that CO adsorption at higher pressures (in the Torr range) is essentially identical to that at low pressures. No new adsorption phases were observed, which is in agreement with previous SFG results [12].

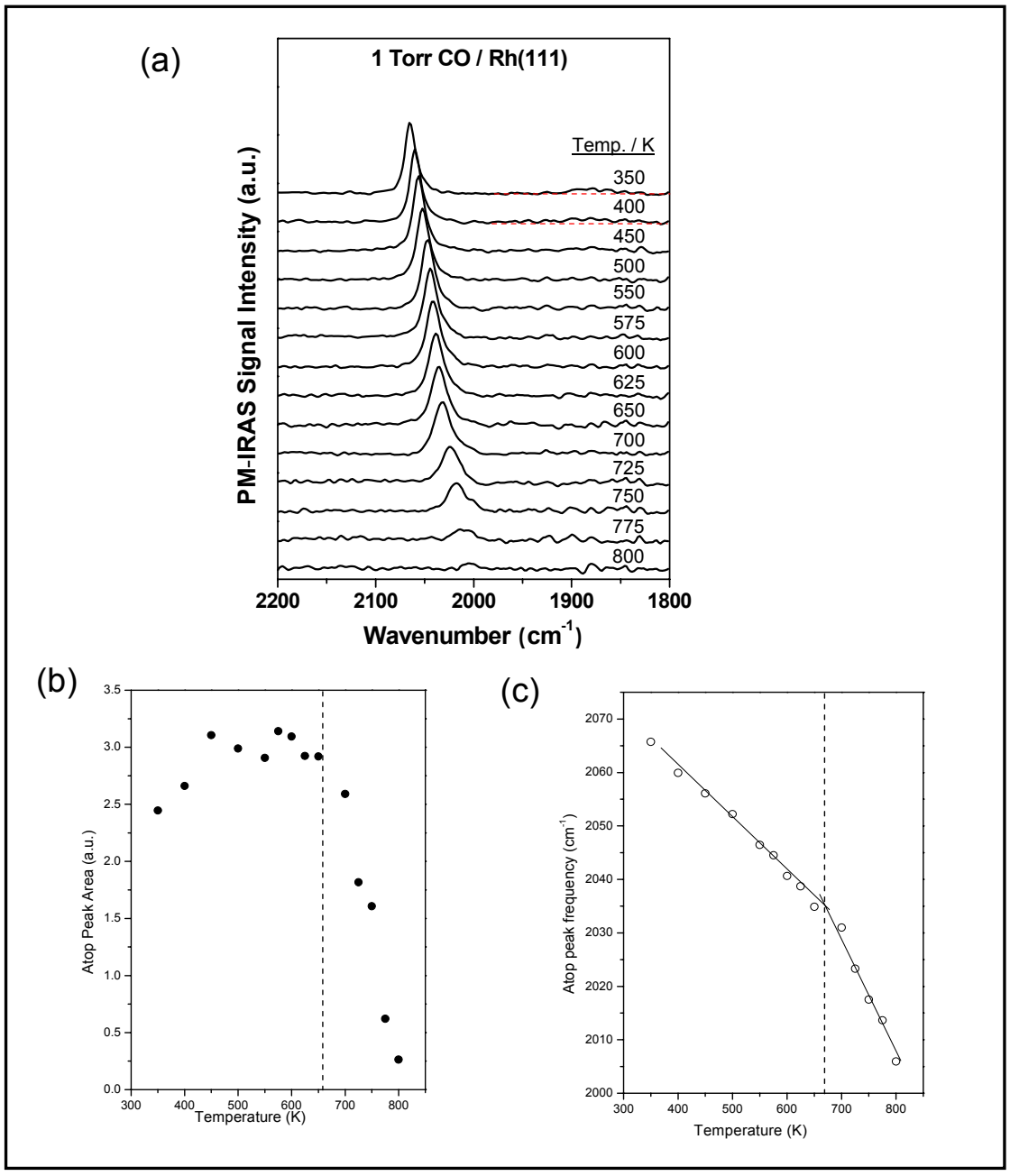

Fig. 27. Adsorption of 1.0 Torr of CO on Rh(111). (a) PM-IRA spectra at various temperatures. Sample temperatures are marked adjacent to each spectrum; (b) integrated peak area of atop feature; (c) vibrational frequency as a function of sample temperature.

CO Oxidation on Rh(111)

Low-pressure steady state CO oxidation on Rh (111)

The experiments of steady-state reactions at low pressures were performed in the following fashion: pre-mixed CO and O_2 with various compositions were introduced into the UHV chamber through a leak valve to reach a certain total pressure; the sample temperature was then raised stepwise to the steady state reaction temperature. The gas phase signal intensities at 28 (CO), 32 (O_2), and 44 (CO_2) amu were monitored with a mass spectrometer. Once a steady state was reached, i.e., the CO_2 formation rate did not vary with time, PM-IRA spectra were taken of the adsorbed CO. The sample temperature was then changed to another value at which the same measurements were performed.

CO oxidation in 1:1 O_2/ CO mixtures

Fig. 28a displays CO_2 formation rates at different sample temperatures where the Rh(111) sample was stepwise heated to higher temperatures with the presence of a 1:1 O_2/CO mixture at a total pressure of 2.0×10^{-7} Torr. As shown, the reaction rate increases with temperature. At 470 K, the reaction rate reaches a maximum, and then decreases at higher temperatures. The corresponding PM-IRA spectra at various reaction temperatures are shown in Fig. 28b. Fig. 28c shows the corresponding CO peak area and vibrational frequency as a function of temperature. For the purpose of direct comparison, results with CO alone are also plotted. As displayed in (c), CO red-shifts gradually with temperature, and co-adsorption of O_2 does not affect the CO signal below 440 K. This

suggests that the surface is still predominantly covered by CO at this temperature. Above 440 K, however, the CO intensity decreased significantly.

From the CO adsorption experiments, it has been known that at pressure of 10^{-7} Torr of CO, and at temperature above 440K, the surface is free of CO adsorption on three-fold hollow sites, which facilitates the adsorption and dissociation of oxygen. The reaction thus goes faster, giving rise to the sharp drop of CO adsorption intensity. Before 440 K, because the surface is poisoned by CO, oxygen can only dissociatively adsorb on defect sites, and the reaction rate is low. In Fig. 28c, at temperatures higher than 440 K, although atop CO intensity drops much faster due to the reaction, its vibrational frequency monotonously red-shifts until the temperature reaches 480 K, a temperature above which the reaction rate starts to decrease and CO vibrational frequency shifts to a higher wavenumber. The reaction rate reaches a maximum (R_{max}) at 470 K, at which the CO coverage is almost zero. The shift of vibrational frequency suggests that before the reaction rate reaches maximum, the dissociatively adsorbed oxygen does not have either the coupling effect with CO or electronic effect with Rh substrate, at least not strong enough, to influence the vibrational frequency of adsorbed CO. Another possibility is the formation of (2 × 2)O + CO structure. Based on the studies of Krenn [135] and Schwegmann [137], this structure has similar mixing energy to that of the (2 × 2)-3CO structure. Therefore oxygen has less influence on CO adsorption, which explains the small change in CO stretching frequency. It is also plausible that before the R_{man}, most dissociatively adsorbed oxygen reacts with CO

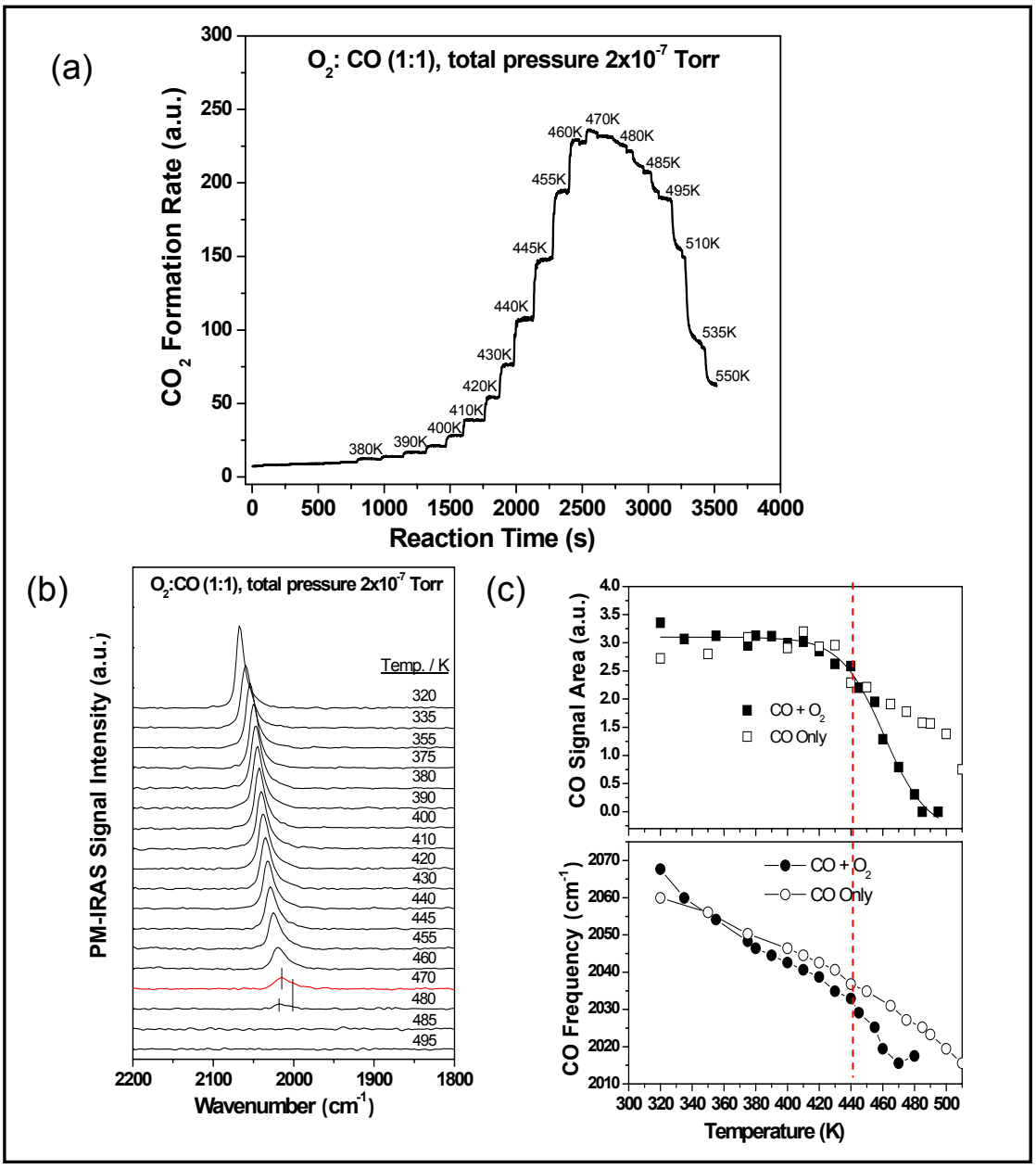

Fig. 28. Steady-state reactions on Rh(111) in a 1:1 O_2 / CO mixture at a total pressure of 2.0×10^{-7} Torr. (a) CO_2 formation rate at different temperatures; (b) PM-IRA spectra corresponding to (a); (c) integrated atop CO signal area and vibrational frequency as a function of temperature. CO alone data is also presented.

right away, before the formation of islands, and hence the reaction rate is only determined by the adsorption of oxygen. At higher temperatures, the decrease of the reaction rate could be due to the decrease of CO sticking probability and the formation of oxygen islands; the latter can be inferred from the blue shift in the vibrational frequency of the atop CO feature.

CO oxidation in 5:1 O_2/ CO mixtures

Similar experiments were conducted in 5:1 O_2/CO mixtures. CO_2 formation rate as a function of reaction time, and the corresponding PM-IRA spectra are shown in Figs. 29. During the reaction, only the atop-CO feature is observed, whereas the intensity remains constant up to 410 K, while the vibrational frequency exhibits a monotonic decrease. Such evolutions are similar to those in the reactions of 1:1 O_2/CO mixtures. A noticeable phenomenon, however, as displayed in Fig. 29, is a considerable increase of the CO_2 formation rate upon heating from 410 K to 415 K. As a result, a sharp peak appears in the spectrum, which was not observed in the reaction of 1:1 O_2/CO mixture. The corresponding PM-IRA spectra exhibit a sharp drop in the intensity of the CO adsorption band. The vibrational frequency also shifts from 2046 cm^{-1} at 410 K to 2052 cm^{-1}. Such dramatic changes indicate the adsorption of oxygen atoms which alter the CO surroundings, and in turn, affect the vibrational dipole. CO coverage at 410 K can be estimated to be ~ 0.36 ML, inferred from the vibrational frequency of 2046 cm^{-1}. The infrared feature at 2052 cm^{-1} is stable up to 425 K, and then disappears at

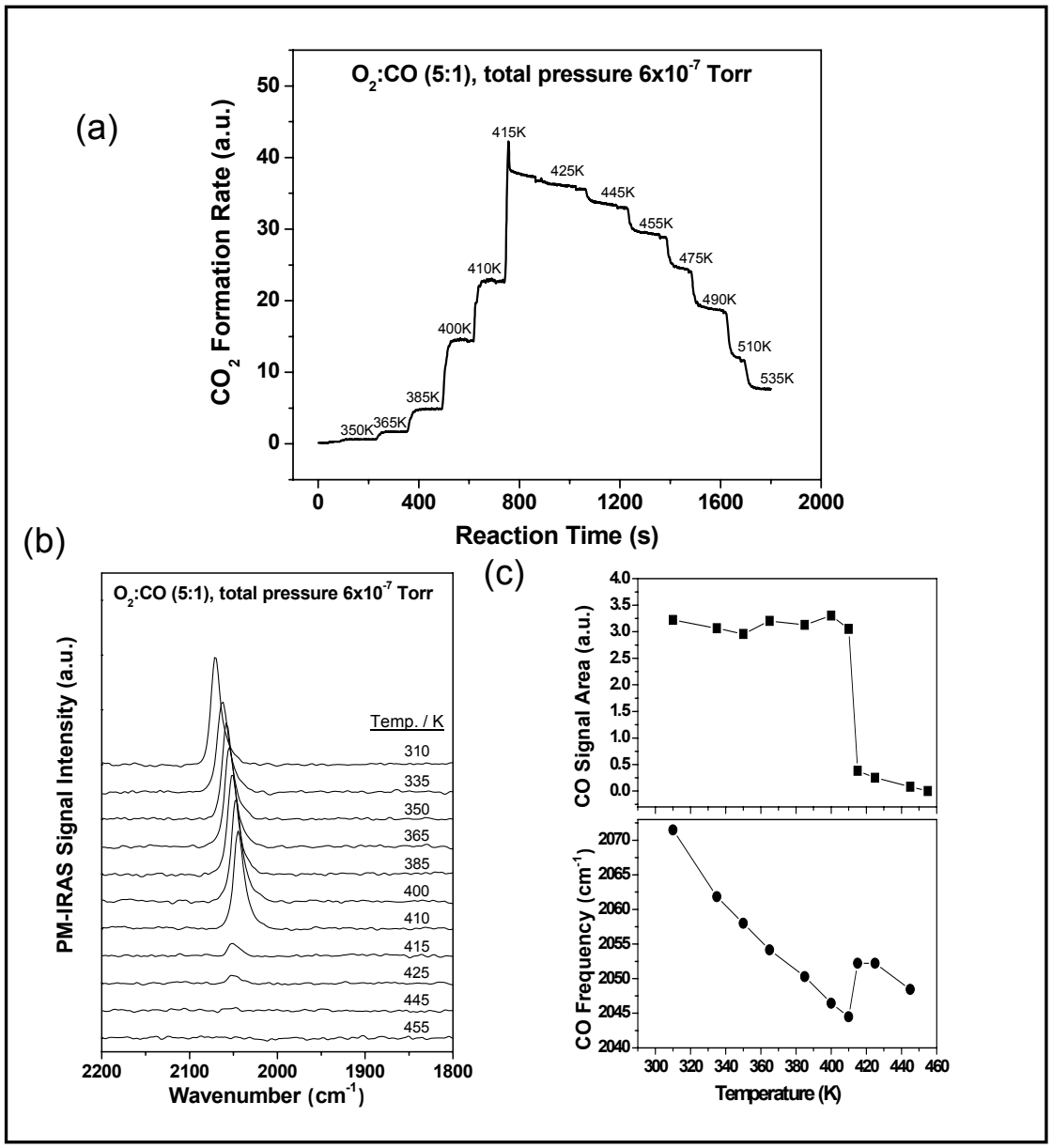

Fig. 29. Steady-state reactions on Rh(111) in a 5:1 O_2/CO mixture at a total pressure of 6.0×10^{-7} Torr. (a) CO_2 formation rate at different temperatures; (b) PM-IRA spectra corresponding to (a); (c) integrated atop CO signal area and vibrational frequency as a function of temperature.

higher temperatures. The fact that the occurrence of maximum rate in 5:1 O_2/CO mixture at lower temperature (415 K) than that in 1:1 O_2/CO mixture (470 K) suggests that the reaction activates earlier in oxygen-rich conditions.

CO oxidation in 10:1 O_2/ CO mixtures

Fig. 30 shows the CO_2 formation rate as a function of reaction time in the 10:1 O_2/CO mixture with the CO partial pressure of 1.0×10^{-8} Torr. The sample was first stepwise heated to high temperatures, and then stepwise cooled in O_2/CO mixtures. This allows hysteresis, if it exists, to be explored easily. A jump of the CO_2 formation rate occurred when the sample was heated from 360 to 365 K. The graph basically resembles that in the 5:1 O_2/CO mixture, but the abrupt increase of the rate ("jump") was more pronounced. Fig. 30b shows the corresponding PM-IRA spectra at various sample temperatures; Fig. 30c plots the integrated CO peak area and vibrational frequencies. These data, together with similar measurements performed at other O_2/CO ratios and total pressures, demonstrate that the jump in rate occurs only when the surface changes quickly from CO-rich to CO-deficient conditions. This is well-reflected by data shown in Fig. 30c where at 360 K, CO displays a strong atop feature at 2052 cm^{-1} demonstrating a CO-rich surface. While at 365 K, the signal intensity drops greatly; meanwhile, it blue-shifts to 2060 cm^{-1}, demonstrating the formation of a CO, O co-adsorbed surface. As the sample was cooled from 375 to 360 K, no such jump was observed; the corresponding PM-IRA spectra exhibited a gradual increase of CO signal. Such abrupt

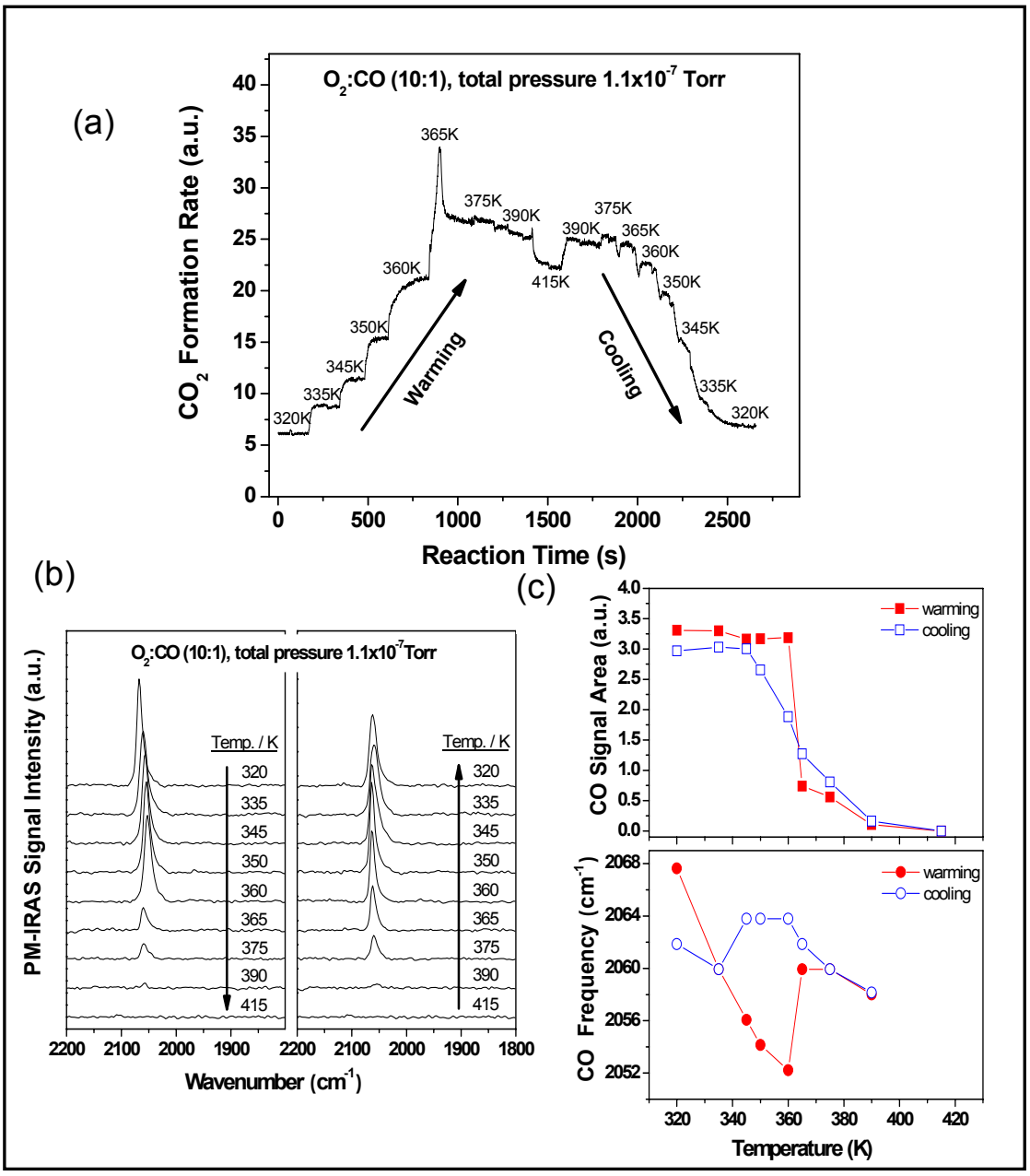

Fig. 30. Steady-state reaction on Rh(111) with a 10:1 O_2/CO mixture at a total pressure of 1.1×10^{-7} Torr. (a) CO_2 formation rate at different temperatures; (b) PM-IRA spectra corresponding to (a); (c) integrated atop CO signal area and vibrational frequency as a function of temperature.

increase of the reaction rate is less prominent in the experiments with higher partial pressure of CO (data not shown), suggesting the insufficient supply of CO onto the sample surface in a short time period may account for the "jump".

To explore the surface state during the "jump", time-dependent PM-IRA spectra (Fig. 31) were collected at 365 K with only 4 scan (~4 s) for each spectrum. As shown in Fig. 31, the reaction rate starts to increase from spectra No.5 at the expense of CO adsorption feature A. Another adsorption feature B emerges as a shoulder first, and then becomes the only adsorption band in the spectra after the R_{max}. The intensity of feature A is almost zero when the R_{max} is reached, while the intensity of feature B remains constant in the whole period of time. From the CO stretching frequency, it is reasonable to assign A as CO on CO islands, and B as CO on oxygen islands, respectively. It is evident that the reaction rate is inversely proportional to the intensity of A, and thus A should be the species that inhibits the reaction. Right before the emergence of feature B, the vibrational frequency of feature A is ~ 2050 cm^{-1}, a wavenumber which is characteristic for the initial adsorption on three-fold hollow sites [135]. In other words, at the coverage below 0.33 ML, three-fold hollow sites are free of CO adsorption. Therefore, the appearance of B indicates the existence of hollow site vacancies, and the occupation of oxygen on those sites. As seen from Fig.31, the appearance of feature B facilitates the CO_2 formation, and the quick consumption of the adsorbed CO layer gives rise to the "jump" in the reaction rate. After the "jump," the surface is co-adsorbed by CO and O in the same unit cell, which could be either 1CO+1O or 1CO+2O according to the DFT calculations [135]. The steady-state reaction rate after the jump, therefore,

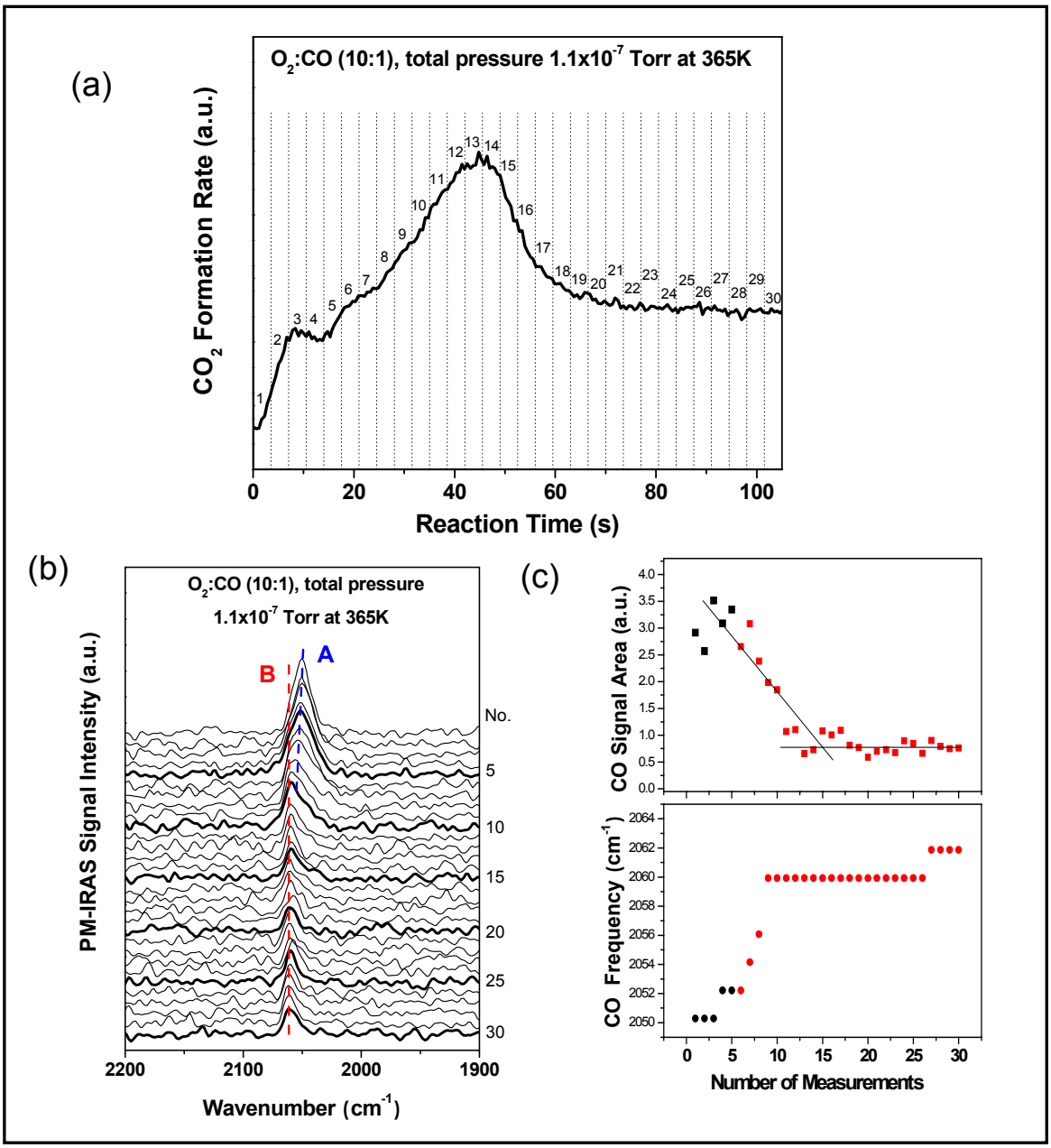

Fig. 31. CO oxidation on Rh(111) in a 10:1 O_2/CO mixture at a total pressure of 1.1 × 10^{-7} Torr at 365 K. (a) CO_2 formation rate vs. reaction time during the "jump;" (b) PM-IRA spectra corresponding to (a); (c) integrated CO signal area and vibrational frequency of the spectra. Red one refers to the spectrum after the appearance of feature B.

occurs on such CO, O co-adsorbed surfaces.

Fig. 32 summarizes the low-pressure results, where the CO_2 formation rate (presented using turnover frequency, TOF, molecule/site/second) is plotted at various reaction conditions. Under all reaction conditions, CO_2 formation rate increases as the sample was heated to higher temperatures until an R_{max} is reached. Following that, the CO_2 formation rate decreases with increasing temperature. This behavior is fully consistent with the Langmuir-Hinshelwood reaction mechanism. Several trends can be concluded as follows: 1) for a given P_{CO}, R_{max} for the 1:1 and 5:1 O_2/CO mixtures are similar, but both are higher than the 10:1 mixture. This is especially apparent for $P_{CO} = 1 \times 10^{-8}$ Torr; 2) for a given O_2/CO ratio, reaction temperature at R_{max} increases with reactant pressure; 3) for a given P_{CO}, reaction temperature at R_{max} decreases with O_2/CO ratio.

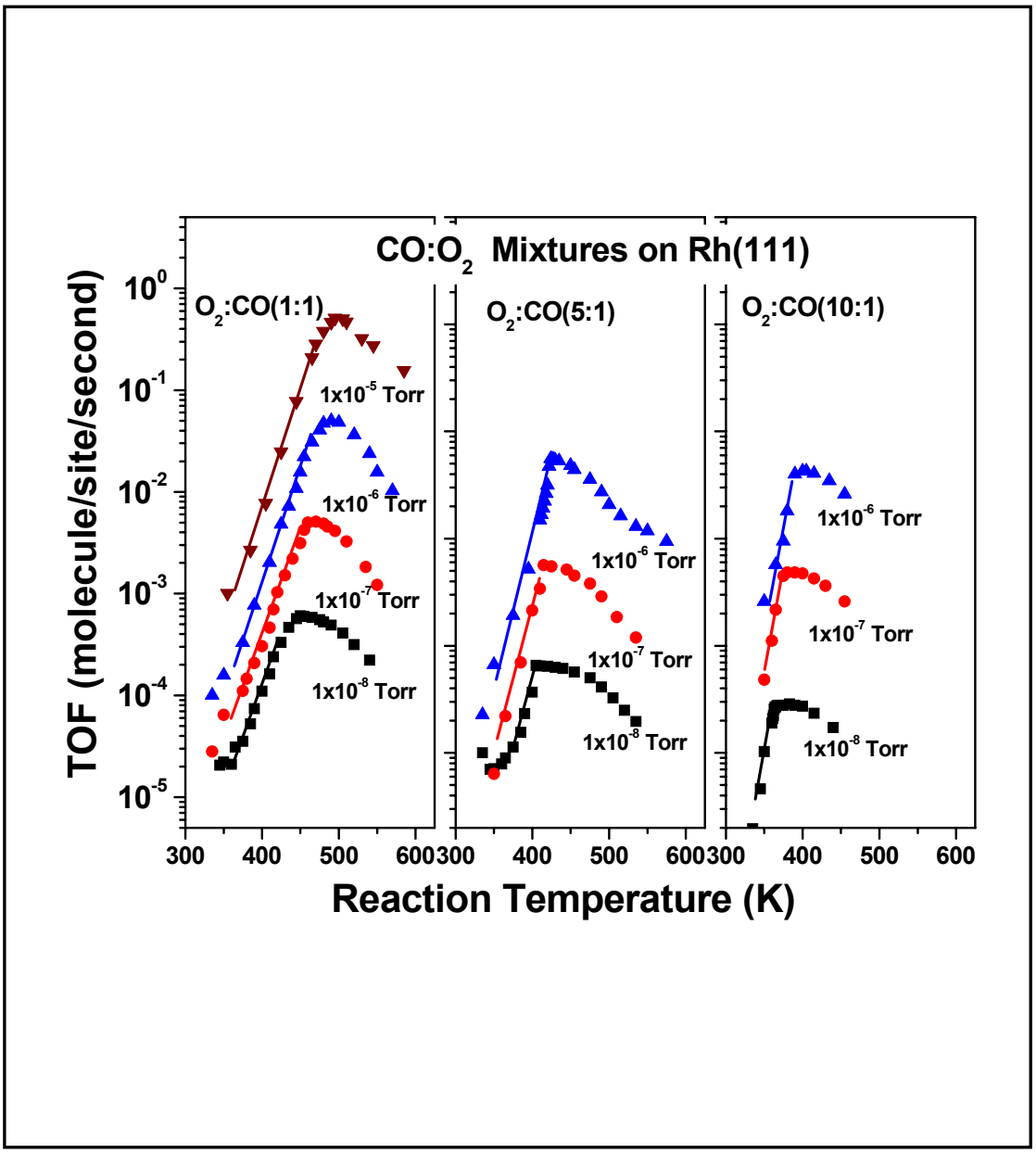

Fig. 32. CO_2 formation rate (in TOF, molecule/site/second) as a function of reaction temperature for 1:1 (left panel), 5:1 (middle panel), and 10:1 (right panel) O_2/CO mixtures at various CO partial pressures as denoted on the graph.

High-pressure reactions

Experiments were also carried out at high pressures where P_{CO} was kept at 8.0 Torr while O_2 pressure varied from 8.0 to 80 Torr. During the experiment, the whole UHV chamber (~60 L) served as the reactor and was pressurized with reactants, and the Rh(111) sample was placed in a high pressure cell. Fig. 33 exhibits one of the high pressure experiments, in which 8.0 Torr of CO and 8.0 Torr of O_2 were introduced to the chamber; changing the order of CO and O_2 introduction did not have any effect on the reaction. Thereafter, the Rh(111) sample was heated step-wise from 315 to 700 K, after which it was cooled to 550 K and heated to 575 K again. Finally the sample was cooled back to 450 K. Concurrently the pressure of the gaseous reactant was monitored with a Baratron gauge, and the resulting change of pressure was subsequently used to calculate the reaction rate. Fig. 33(a) displays the total pressure versus time curve at various sample temperatures, and (b) shows the corresponding PM-IRA spectra. It is apparent from the pressure-time curve that three reaction regimes could be distinguished: a low reaction rate regime below 550 K, an transient high rate regime at 575K, and a steady high rate regime above 550 K. Note especially that the transient reaction rate increase at 575 K causes a transient sample temperature jump of ~25 K (marked with solid cycles). However, this behavior does not always occur. As the sample was cooled from 700 to 550 K, and then increased to 575 K again, this phenomenon is not observed (marked with dashed cycles). Only when the sample was cooled to 450 K or below, and then annealed again, could this behavior be reproduced (data not shown).

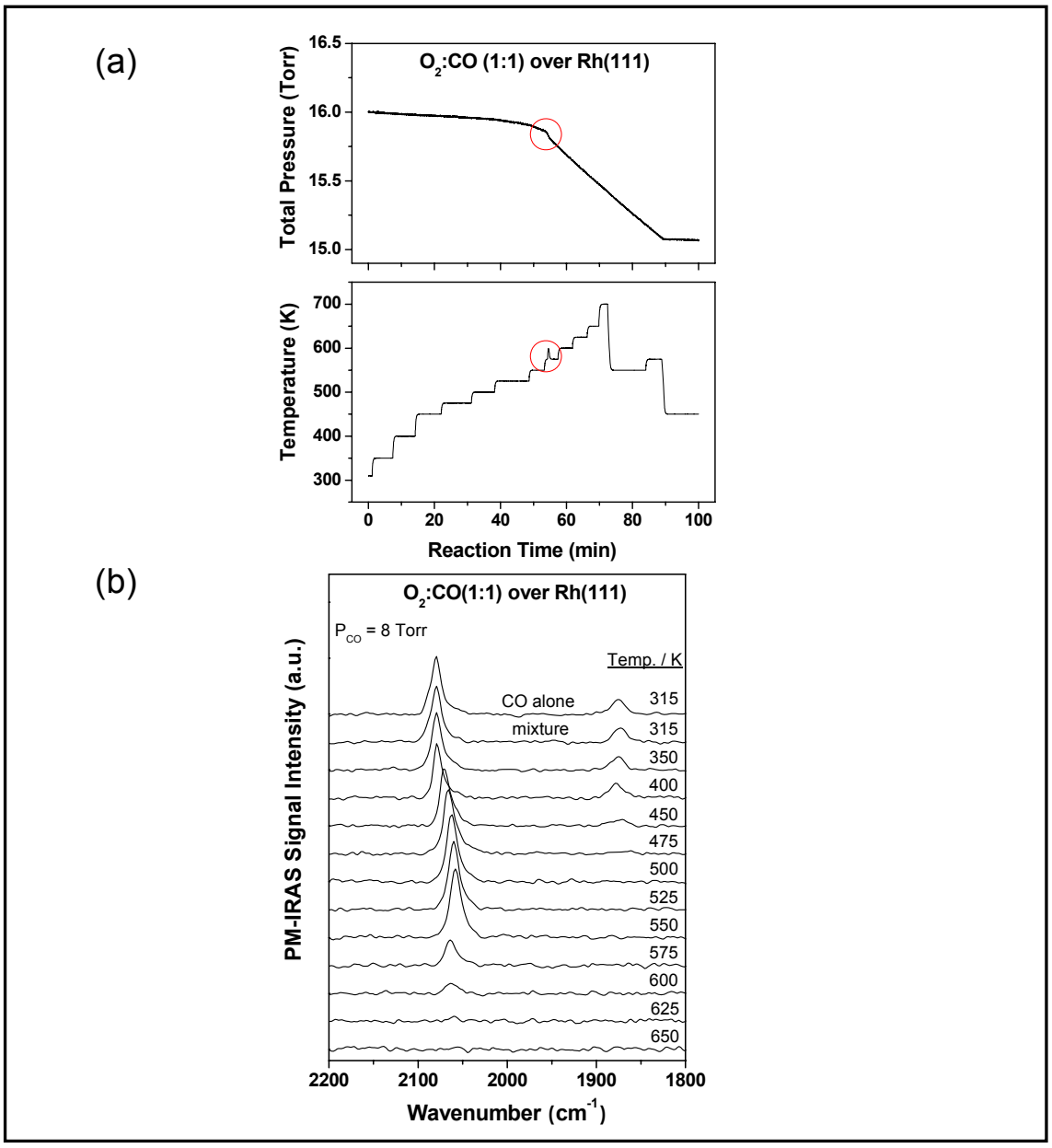

Fig. 33. CO oxidation on Rh(111) in a 1:1 O_2/CO mixture at a total initial pressure of 16 Torr. (a) Total pressure and sample temperature versus reaction time; (b) the corresponding PM-IRA spectra at different temperatures where reaction temperate is marked adjacent to each spectrum. All spectra are acquired during heating the sample. Spectra recorded after 650 K are not shown.

The corresponding PM-IRAS spectra are displayed in Fig. 33b. At 450 K and below, the strong three-fold hollow CO species were found at ~1880 cm^{-1}, suggesting that the surface CO coverage was approaching 0.75 ML [131, 135]. Starting from 500 K, this feature completely disappears, indicating that surface CO coverage have dropped below 0.5 ML. At 575 K the atop CO signal intensity decreases greatly, accompanied by a 6 cm^{-1} blue-shift (2059 to 2065cm^{-1}). It is evident that the surface has changed from CO-rich to O-rich at this temperature. Note that this is where transient reaction rate jump occurs, and the behavior appears to be identical to that found at low pressures (Fig. 29, 30). By 625 K, surface CO species disappears completely. Interestingly, the reaction rate remains rather constant between 575 and 700 K, i.e. independent of surface CO coverage.

Fig. 34 displays PM-IRA spectra acquired with a 5:1 O_2/CO mixture at a total pressure of 48 Torr. The pressure vs. time curve is not shown since it resembles that shown in Fig. 33a. In this case a transient reaction rate jump occurs at 530 K. It should be mentioned that PM-IRA spectra acquired after the jump point display two atop CO features at 2084 and 2065 cm^{-1}. At 575 K, all surface CO features disappear. The peak at 2065cm^{-1}, which was also observed in low pressure reactions, is from adsorbed-CO islands. The vibrational feature at 2084 cm^{-1}, however, was not observed in either low-pressure or high-pressure 1:1 O_2/CO reactions. Since these two atop features appear only in the reaction at high O_2/CO ratio reactants, oxygen species (either at or below surface) should account for their emergence.

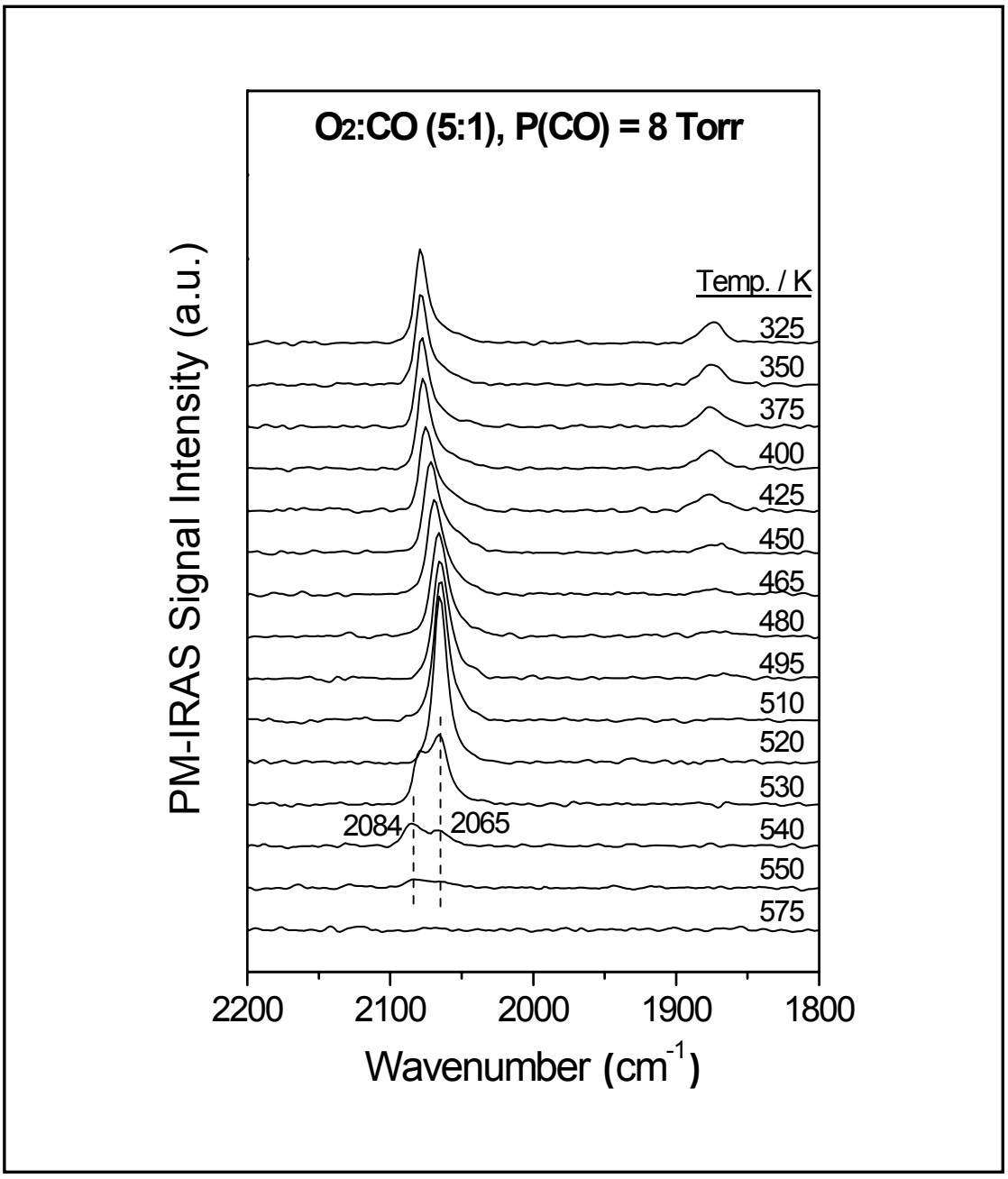

Fig. 34. PM-IRA spectra acquired at different temperatures on Rh(111) in a 5:1 O_2/CO mixture at a total initial pressure of 48 Torr. Reaction temperate is marked adjacent to each spectrum.

Fig. 35 shows the PM-IRA spectra during the reaction in 1 Torr CO and 8 Torr O_2 mixture at 460 K. From the top to the bottom, the spectra depict the development of surface phases with time (0.5min/spec.). The Rh(111) surface was first fully covered by CO, as evident by the CO stretching frequency at 2067 cm^{-1}. A transient increase in the reaction rate ("jump") (not shown) was observed between spectra 13 and 14. Similar to the reaction in 5:1 O_2/CO mixture, two atop features at 2083 and 2067 cm^{-1} appear in the spectra right after the jump. Another high frequency feature at 2130 cm^{-1} also appear in the spectra, which is often observed in the reactions on oxide supported Rh catalysts, and is assigned as the CO adsorption on Rh(111) sites [138]. Therefore, the appearance of 2130 cm^{-1} correlates with a highly charged Rh atom, such as Rh(III) in bulk oxide Rh_2O_3. Therefore, it is possible that Rh_2O_3 formed after the jump.

As a summary of high pressure experiments, Fig. 36 shows the PM-IRA spectra acquired during the high pressure reactions in various gas compositions with the same CO partial pressure of 8 Torr. It is apparent that before the reaction rate rollover, the surface was dominated by CO. Right after the occurrence of the maximum rate (R_{max}), the spectra display different adsorption features for the reactions in different gas compositions: in the reactants with O_2/CO ratio ranging from 1/2 to 2/1, no shift or only a slight shift in vibrational frequency was observed, indicating the formation of a co-adsorbed CO, O phase; in (5:1) and (10:1) O_2/CO mixtures, however, another atop feature at 2084 cm^{-1} appeared, suggesting the formation of a stronger bonded oxygen species.

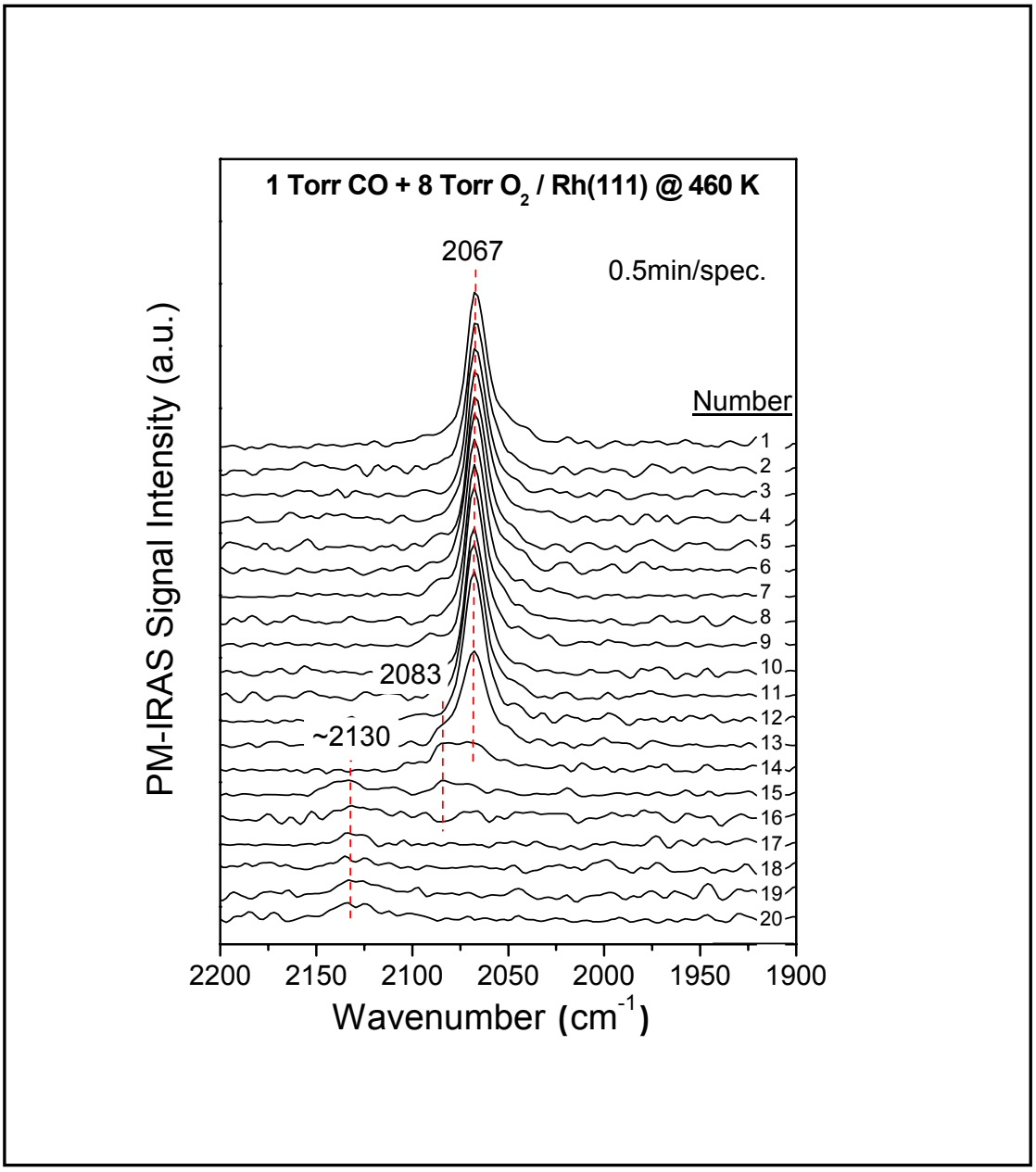

Fig. 35. PM-IRA spectra acquired at 460 K on Rh(111) in 1 Torr CO and 8 Torr O_2 mixture.

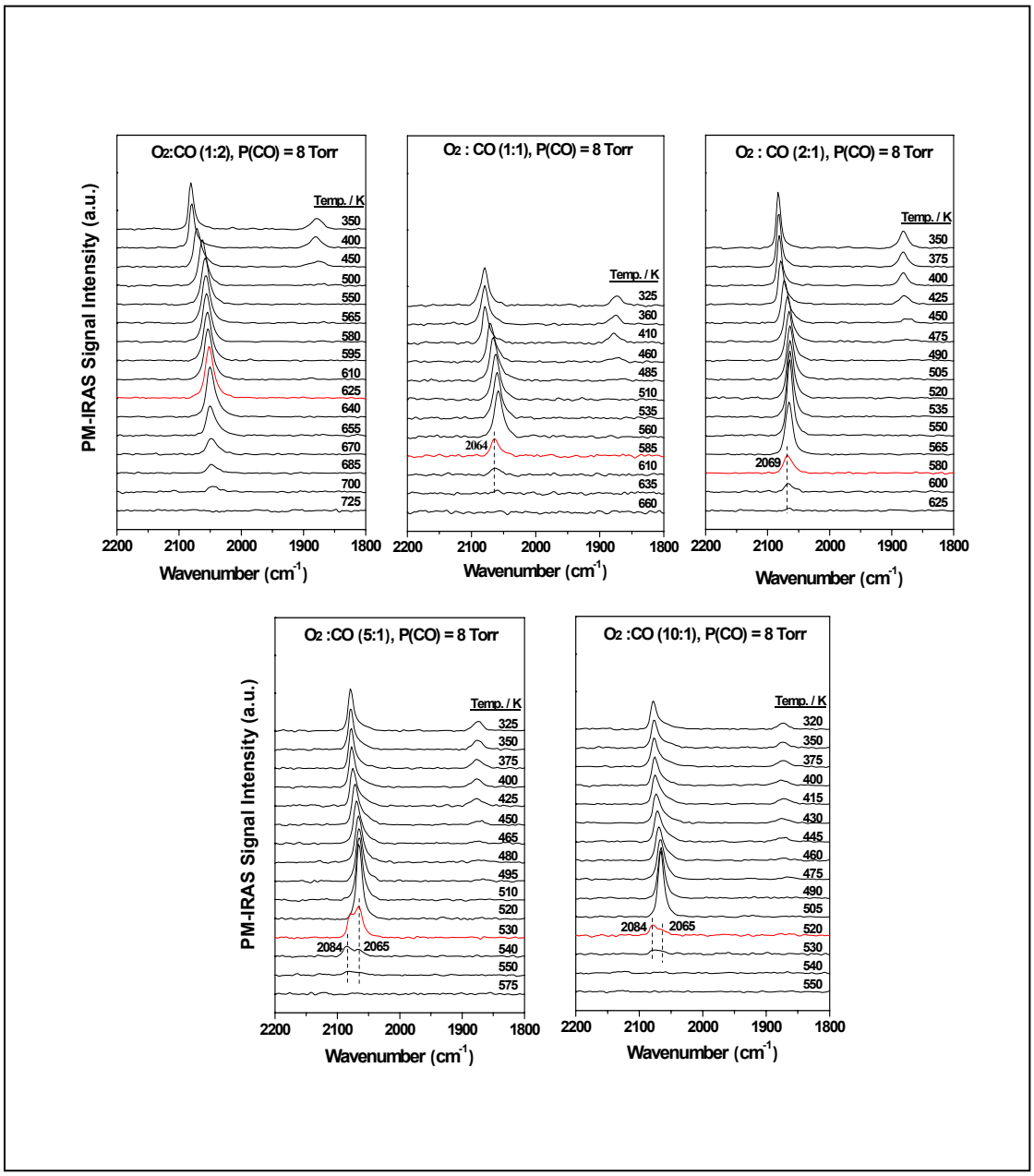

Fig. 36. PM-IRA spectra of CO oxidation on Rh(111) in various gas compositions. The detailed gas compositions and reaction temperatures are as indicated. The spectrum taken right after the occurrence of the maximum rate was marked in red.

The reaction rates represented as TOF corresponding to experiments in Fig. 36 are summarized in Fig. 37. The spectrum taken right after the rollover ("jump") in the reaction rate is marked in red in Fig. 36. Tthe solid data points displayed in Fig. 37 are the actual rates measured, while the arrow above the maximum rate is plotted as an indication that the rate could be much higher if there were no mass transfer limitation effect which will be addressed later in another chapter.

Below 450 K, all five mixtures display low TOF regardless of temperature (not shown), suggesting the reaction barely occurs before the desorption of CO. From 475 K to the rollover temperature, the reaction rate displays a positive order in O_2 pressure. This situation is no longer observed at the higher temperatures. It can be seen that in 1:2 O_2/CO mixture, the reaction rate rolls over at 625 K, and then remains constant at higher temperatures. At 625 K, the infrared spectrum indicates that the surface is covered by ~ 0.5 ML of CO, suggesting the surface is free of oxygen or with little oxygen staying at the surface. The same phenomena is observed in Ref. [139] as well. It can also be inferred that under high temperature, high pressure conditions, the high mobility of the reactants maintains the high reaction rate, while the absolute rate depends on the amount of CO arriving at the surface.

In the cases of higher O_2/CO ratios (not 1/2), transient rate increases ("jumps") were observed. Right after the jump, the blue-shift of the CO stretching frequency occurs. The vibrational frequency of CO shifts to higher wavenumber in higher O_2/CO ratio gas composition. Moreover, two atop CO features appear in the reactions in 5:1 and 10:1 O_2/CO mixtures. In the case of O_2/CO from 1:2 to 2:1, the reaction rates after the

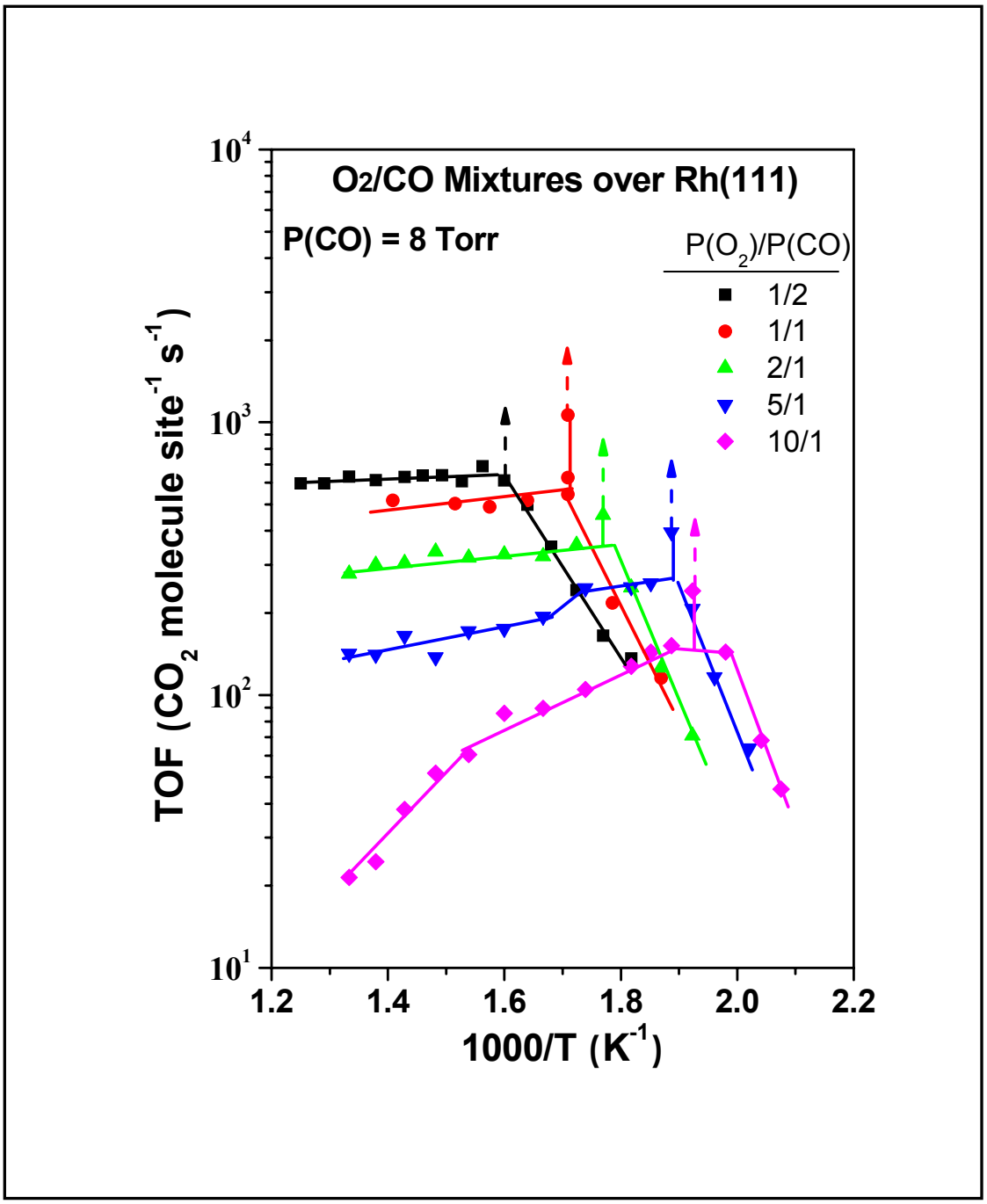

Fig. 37. Arrhenius plot of CO_2 formation rate (represented as TOF) on Rh(111) at various O_2/CO ratios.

rollover points remain constant, although their absolute rate decreased with the increase of the O_2/CO ratio. For the reactions in 5:1 and 10:1 O_2/CO mixtures, the reaction rate decreases after rollover temperature, and drops more at higher temperatures. Based on the correlation between infrared spectra and kinetic data, it can be inferred that the oxygen species related with atop-CO vibrational feature at 2084 cm^{-1} deactivate the surface.

It is noteworthy that the transient rate increase ("jump") only occurs from CO-rich surface to CO-deficient surface. Once the vibrational feature of 2084 cm^{-1} or 2130 cm^{-1} shows up in the spectrum, the reaction rate decreased. From the analysis of the low pressure reaction, it is known that the reaction accelerates when vacancies at the surface are available for the adsorption of oxygen. Therefore, on the one hand, chemisorbed oxygen plays a role in activating the reaction. On the other hand, the oxygen species associated with the adsorption bands at 2084cm^{-1} or 2130cm^{-1} deactivate the reaction.

Since oxygen species play such an important role in the reaction, it is of great importance to understand the interaction of oxygen with the Rh(111) substrate. Oxygen adsorption and reaction have been investigated extensively on Rh(111). At low O_2 exposures and under UHV conditions, a (2 × 2) structure forms at an oxygen coverage of 0.25 ML, and a (2 × 1) structure forms at an oxygen coverage of 0.5 ML [134]. Even at these low coverages, oxygen penetration into subsurface occurs between 390 and 800 K [140]. As pointed out by Over et al. [134], O penetration into Rh(111) is energetically more favorable than adsorption on the surface, even for a small first Rh layer expansion

(of ~ 3%, occurs when O coverage reaches ~0.5 ML). This explains why a (1 × 1)-O structure with a coverage of 1.0 ML decays at 400 K and above, although it can be formed using atomic oxygen at room temperature [141]. Using 10^{-3} mbar of O_2 at 400 K for 5 min, Kohler *et al* prepared a (2 √ 3 × 2 √ 3)R30˚structure that has an oxygen coverage of 0.66 ML [142]. In this case, no subsurface oxygen was found with high resolution core-level photoemission. However, under similar conditions, subsurface oxygen was indeed detected using X-ray photoelectron diffraction [143]. Using 2×10^{-4} mbar of O_2 at 800 K, a trilayer surface oxide can be formed on Rh(111) where half the oxygen stays on the surface while the other half stays in the third layer [144]. In situ CO titration probed with XPS revealed that this phase is far less reactive than chemisorbed oxygen [145], consistent with the reactivity order of Pd-O species, i.e. chemisorbed O > surface oxide > bulk oxide, determined using the same method [146]. In fact, oxygen inhibition of CO oxidation on rhodium has long been recognized by White et al. [147]. The reason, at least partially, is due to CO adsorption inhibition.

From the above literature results, it can be deduced that the adsorption band at 2084 cm^{-1} is probably related to the subsurface oxygen or surface oxide which attracts electrons from the Rh substrate. As a result, the CO-metal bond is weakened due to the less back-donation from Rh.

CO Titration of Oxygen-Covered Rh(111) Surfaces

To explore the extra atop species, i.e., 2130 and 2084 cm^{-1}, which are evidently associated with oxygen species on/under the surface, XPS experiments were carried out to correlate the vibrational features with the oxygen coverage on the surface. Under many reaction conditions during this study, i.e., the total gaseous pressure exceeds ~2 × 10^{-6} Torr, monitoring surface CO and O coverages *in situ* with XPS becomes impossible. In these cases, especially during high-pressure reactions, surface CO coverage can only be derived from estimation using vibrational frequency, peak area, and lineshape of CO peaks with known coverages. The estimation of surface O coverage is more difficult, and sometimes impossible. Note from Fig. 34 that for the 5:1 O_2/CO mixture, at high pressures, two atop CO features coexist at 530 and 540 K, indicating the existence of the nonequivalent surface sites for CO. However, this phenomenon was not found either at low pressures or in 1:1 and 2:1 O_2/CO mixtures at high pressures. In order to gain more information on surface oxygen coverage and its effect on CO adsorption, oxygen-covered surfaces were prepared with known coverages. The oxygen-covered surfaces then were titrated with 1:1 O_2/CO mixtures. As shown in Fig. 38a, three O-covered surfaces were prepared. In the first case, clean Rh(111) was exposed to 1 × 10^{-7} Torr of O_2 at room temperature until the O 1s signal reached a constant, exhibiting an O 1s/Rh $3d_{5/2}$ signal intensity ratio of ~0.05. According to previous studies, this leads to an O coverage of 0.5 ML [134]. Two other O-covered surfaces were made by reacting clean Rh(111) with 3000 and 12000 L of O_2 at 800 K, respectively. By measuring their O 1s/Rh $3d_{5/2}$ ratios, oxygen coverages were easily derived to be ~0.83

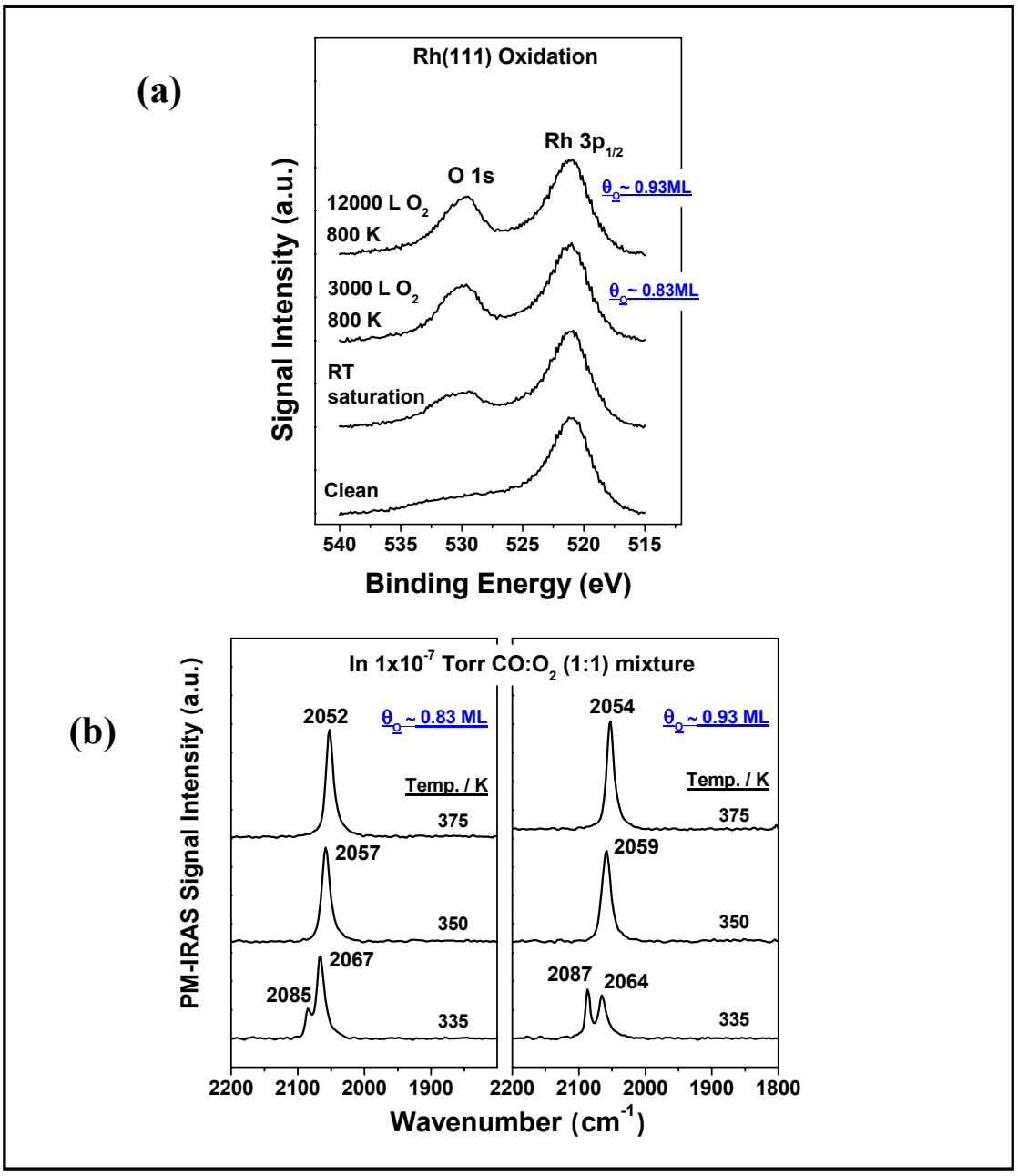

Fig. 38. CO titration on oxygen-covered Rh(111) surfaces. (a) O 1s and Rh 3p XPS spectra for different O-covered surfaces. Oxidation conditions are marked adjacent to each spectrum. (b) PM-IRA spectra acquired by exposing the O-covered surface to 1:1 O_2/CO mixture at a total pressure of 1×10^{-7} Torr at 335, 350 and 375 K.

and ~0.93 ML, respectively. Note that under these reaction conditions oxygen penetration into subsurface already occurred [134, 140]. So it is not possible to measure oxygen coverage of the topmost layer. The same oxygen-covered surfaces, i.e., $\theta_O = 0.83$ and 0.93 ML, were prepared in PM-IRAS chamber. These two surfaces were then exposed to 1:1 O_2/CO mixture at a total pressure of 1.0×10^{-7} Torr at 335, 350 and 375 K. PM-IRA spectra were acquired concurrently right after the introduction of O_2, CO mixtures. Upon exposing the O-covered surfaces to O_2/CO mixtures, surface reduction occurred immediately. The acquired PM-IRA spectra are shown in Fig. 38b. Note that in both cases, spectra acquired at 335 K displayed two atop features, while at higher temperatures only one CO peak was obtained, indicating the reduction of the surface.

An Overlook at CO Oxidation on Rh(111)

Fig. 39 depicts the Arrhenius plots of CO oxidation reactions on Rh(111) in 1:1 O_2/CO mixture at the partial pressure of CO from 1×10^{-8} to 8.0 Torr, in which the experimental data in this study are represented as solid circles, while the empty circles represent the data from Peden's work (Ref. [148]) in 8.0 Torr CO and 8.0 Torr O_2 mixture. Flux lines as marked in Fig. 39a represent the maximum reaction rates that can be achieved at each partial pressure of CO; the value was calculated based on the Hertz-Knudsen equation [149]. Fig. 39b illustrates the reaction probability at the maximum rate as a function of the partial pressure of CO.

At the partial pressure of CO higher than 0.01 Torr, the Arrhenius plots coincide with each other until the rate rolls over. A linear line can thus be drawn with an apparent

activation energy of ~ 110 kJ/mol. The value is close to the CO binding energy on Rh(111), suggesting a saturation coverage of CO at high pressure conditions, which also agrees with the results from the infrared experiments. In the case of CO partial pressures less than 10^{-4} Torr, however, the Arrhenius plot deviates from the above linear curve indicating an unsaturated CO coverage on the surface in low pressure conditions.

The reaction probability curve (Fig. 39b) shows that at CO partial pressures less than 10^{-4} Torr, the reaction probability remains at a constant of ~0.25. With an increase of the CO partial pressure, the reaction probability decreases linearly. At P_{CO}=1.0 Torr, only ~0.3% of the colliding CO is reacted. It is clear that at pressure above 10^{-4} Torr, mass transfer limitation begins to influence the reaction rate.

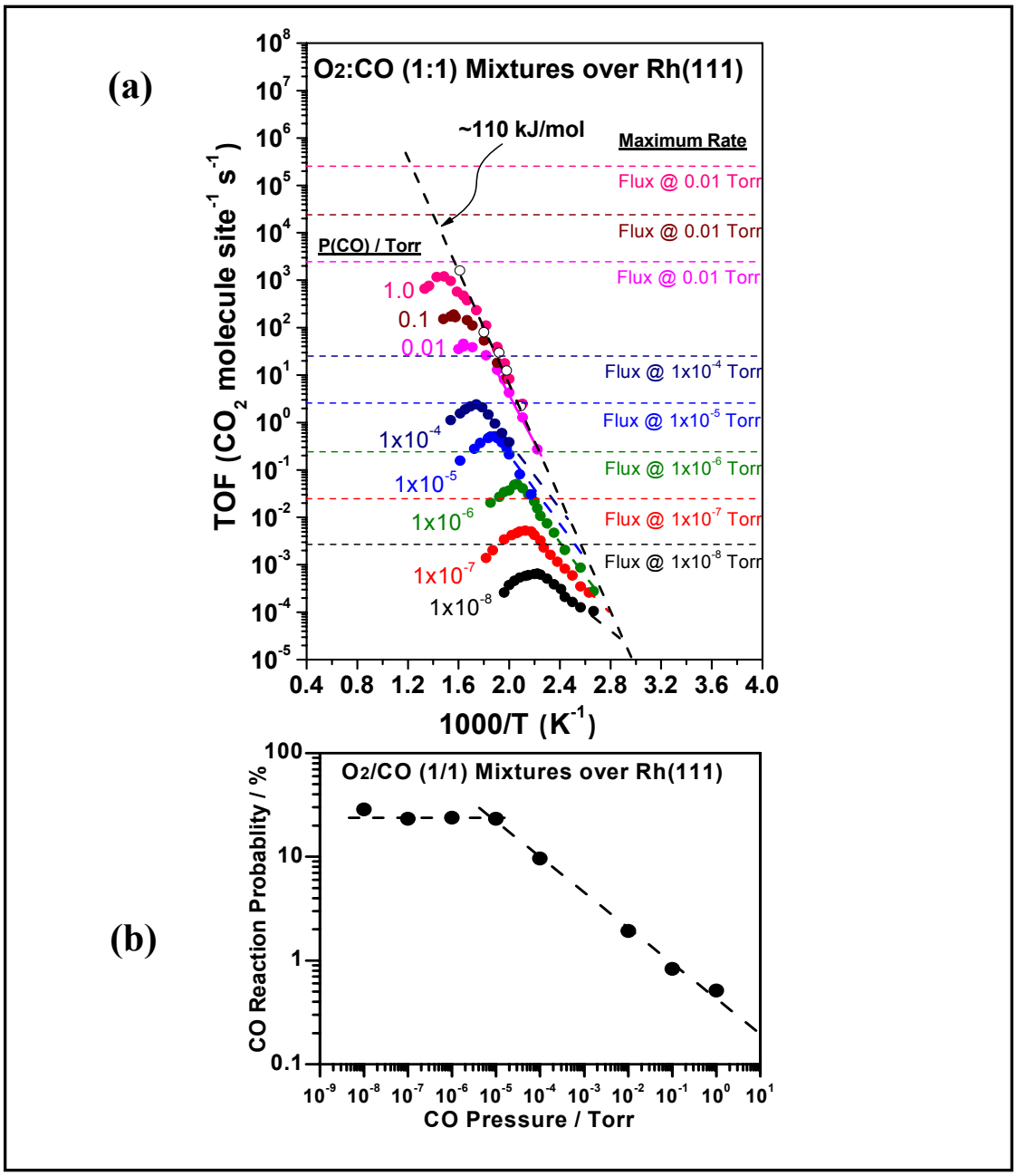

Fig. 39. CO oxidation on Rh(111) in 1:1 O_2/CO mixtures from low to high CO partial pressures. (a) Arrhenius plot. Partial pressures of CO are marked adjacent to each curve. The empty circle are data from Ref. [148]. (b) The reaction probability at the maximum reaction rate as a function of CO partial pressure.

CHAPTER VI

CO OXIDATION ON Pd AND Pt

In the preceding chapter, the concurrent PM-IRAS investigations and kinetic rate measurements on Rh(111) have revealed that CO oxidation reaction at both low pressure and high pressure follow the Langmuir-Hinshelwood mechanism, and the reaction at low pressures can be extrapolated to high pressures. Moreover, the role that oxygen plays in the reaction and the effect of mass transfer limitation on the maximum reaction rate have also been observed. In this chapter, CO oxidation studies of Pd and Pt single crystals are presented, and the mass transfer limitation issue is also demonstrated.

This chapter starts with literature reviews of CO adsorption and oxygen adsorption on Pd single crystals. Studies of high pressure CO adsorption on clean and oxygen pretreated Pd(110) surfaces are also presented. Furthermore, CO oxidation experiments on Pd and Pt are discussed and compared.

Literature Review of CO, O_2 Adsorption on Pd(100) and Pd(111)

CO adsorption on Pd(100)

CO adsorption on Pd(100) has been studied from low pressure to high pressure (up to 10 Torr), and only one single adsorption band, bridge-site adsorption, has been observed through the entire coverage range [32, 150-156]. From the lowest coverage to the saturation coverage of 0.8 ML, the CO stretching frequency shifts continuously from 1895 to ~1997cm^{-1}. At θ_{co} = 0.5 ML, an ordered overlayer structure $c(2\sqrt{2} \times \sqrt{2})R45^{o}$ forms, with a corresponding vibrational frequency of ~1950 cm^{-1} at 300 K [151, 153]. At coverages higher than 0.5 ML, an incommensurate layer, due to the uniaxial compression of the adsorbed CO layer, has been observed. The transition between commensurate-incommensurate layers introduces a broadening of the peak and a sharp increase in the vibrational frequency (~10 cm^{-1}) upon increasing the CO coverage above 0.5 ML [151, 153]. Isotopic substitution experiments revealed that vibrational dipole coupling accounts for the frequency shift at coverages less than 0.5 ML, whereas both chemical and electrostatic effects and vibrational coupling are responsible for those at θco > 0.5 [151]. At low CO coverages, the isosteric heat of adsorption was determined as ~38 kcal/mol [153, 156]. TPD studies [151, 153] showed that below 0.5 ML of CO coverage, only one desorption peak appears with a maximum at ~500 K; above 0.5 ML, another peak at ~ 370 K appears, indicating a decrease in adsorption energy in the transition from the $c(2\sqrt{2} \times \sqrt{2})R45^{o}$ structure to the incommensurate overlayer.

Oxygen adsorption on Pd(100)

Oxidation on Pd(100) is believed to proceed through four stages, involving up to five distinct surface oxygen species [157]. At room temperature, oxygen first dissociatively adsorbs onto surface and into $p(2 \times 2)$ islands for coverages above 0.05 ML [32]. A fully developed $p(2 \times 2)$ structure forms at a coverage of 0.25 ML, a phenomenon first reported by Ertl and Koch [20, 158]. The initial sticking coefficient, 0.4 at $\theta = 0$ [20], decreases significantly at $\theta = 0.25$ ML [157, 159]. Another chemisorbed oxygen phase, $c(2 \times 2)$O-Pd, first illustrated by Orent and Bader [159], starts to develop and coexists with $p(2 \times 2)$ at coverages higher than 0.25 ML, and the surface is completely converted to $c(2 \times 2)$ at $\theta = 0.5$ ML. For both adsorption states, O preferentially remains in the four-fold hollow sites. Upon dosing oxygen at higher temperature ($T > 400$ K [159, 160]), the Pd substrate undergoes reconstruction, ejecting Pd atom onto the terraces [157]; meanwhile, oxygen starts to penetrate into the subsurface. Consequently, a (5×5) phase is formed and followed by a $(\sqrt{5} \times \sqrt{5})R\ 27^{o}$ reconstructed structure. The formation of these reconstructed structures is associated with an increase in the oxygen sticking coefficient [160]. The ideal oxygen coverages of (5×5) and $(\sqrt{5} \times \sqrt{5})R\ 27^{o}$ surface oxide are ~0.64 and 0.8, respectively [159]. Currently, there is no well-defined structure model for the (5×5) phase, whereas the structure of $(\sqrt{5} \times \sqrt{5})R\ 27^{o}$ has been clearly identified recently as a PdO(101) trilayer on Pd(100) containing four Pd atoms and four O atoms in each unit cell [161, 162]. Two Pd atoms are fourfold coordinated with O atoms, while the other two Pd atoms are twofold coordinated. Two of the O atoms sit on top of a Pd atom but the other two are

embedded below the first Pd layer, forming the so-called trilayer structure. In the final stage, after the formation of multilayer or bulk oxide, the LEED pattern fades away and three-dimensional clusters appear in the STM image [157]. TPD investigations showed that *p*(2 × 2) oxygen desorbs at ~800-850 K [32, 157, 160], whereas *c*(2 × 2) oxygen desorbs at ~700 K [32, 157]. The reconstructed structures (5 × 5) and (√5 × √5)R27^{o} give rise to a new sharp peak in the TPD spectrum at 650 K, which shifts to above 700 K at saturation [157, 160]. The desorption temperature of these surface oxides are lower than that of chemisorbed oxygen (~800 K), but much higher than that from bulk oxide decomposition. These facts suggest that the Pd-O bonding strength of the surface oxides are between chemisorbed oxygen and bulk PdO. The surface XRD and DFT studies from Lundgren et al. demonstrated that (√5 × √5)R27^{o} surface oxide can be stable in a wide temperature and pressure range. Furthermore, the formation of this surface oxide kinetically hinders the formation of bulk oxide at temperatures up to 675 K [163].

CO adsorption on oxygen-adsorbed Pd(100)

Low temperature CO adsorption on a *p*(2 × 2) surface exhibits two adsorption bands at ~2125 and ~1990cm^{-1} in IRAS [164] and HREELS [32]. The adsorption of CO on (√5 × √5)R27^{o} surface oxide below 40 K shows two peaks at 2130 and 1940 cm^{-1} [164]. The high frequency vibrational feature was assigned in Ref. [32] as a CO-Pd-O complex. The adsorption band at around 1990 cm^{-1} was also observed on a CO saturated Pd(100) surface, while 1940 cm^{-1} was denoted in Ref. [164] as the characteristic adsorption band on the (√5 × √5)R27^{o} surface. Zheng et al. [165] found that when the

highly oxidized surface on which bulk PdO or surface oxide forms is exposed to CO, a lag in CO_2 production is detected, and the CO_2 formation rate increases as the ($\sqrt{5} \times \sqrt{5}$)R27^o phases are replaced by (2 × 2) domains. STM data revealed that upon CO exposure, rapid transport of oxygen from bulk PdO to ($\sqrt{5} \times \sqrt{5}$)R27^o domain occurs, and in turn, the ($\sqrt{5} \times \sqrt{5}$)R27^o islands decompose to replenish the oxygen loss of neighboring (2 × 2) domains due to the reaction with CO.

CO adsorption on Pd(111)

LEED [150] and STM [166] studies have observed that, on a clean Pd(111) surface, CO first preferentially adsorbs on three-fold hollow sites, and the CO overlayer forms a ($\sqrt{3} \times \sqrt{3}$)R30^o structure which completes at a coverage of 0.33 ML. The initial isosteric adsorption energy of CO on Pd(111) was reported by Conrad as 34 kcal/mol [150], which remains constant at CO coverages up to 0.33 ML (1 ML corresponds to the density of atoms in the surface layer of Pd(111) and is equal to 1.53 $\times 10^{15}$ atom/cm^2) due to the weak attractive interaction between CO molecules [150]. The sticking coefficient also remains at unity until 0.33 ML is reached [167]. At coverages above 0.33 ML, the CO overlayer is compressed. CO starts to populate on two-fold bridge sites and forms a *c*(4 × 2)-2CO structure at θ = 0.5 ML. The isosteric adsorption energy of CO decreases at coverages above 0.33 ML [150]. The further increase of CO coverage enables the adsorption of CO on atop sites and reaches a saturation coverage of 0.75 ML with an overlayer of a (2 × 2)-3CO structure (two molecules adsorb on three-fold hollow sites and one molecule on atop site). The CO vibrational frequency at

90 K from Ref. [56] is ~1850 cm^{-1} at $\theta = 0.33$ ML [167], ~1920 cm^{-1} [34, 167] at $\theta = 0.5$ ML, and 2110 and 1895 cm^{-1} at saturation coverage of 0.75 ML. Subsequent vibrational spectroscopic experiments agree with the above results. Elevated pressure (up to 700 Torr) CO adsorptions on Pd(111) carried out by PM-IRAS [19] and SFG [35] show that CO adsorption follows the same trend as that at low pressures, thus indicating that no new pressure-induced species occur [152].

Oxygen adsorption on Pd(111)

At room temperature, adsorption of oxygen saturates at a coverage of 0.25 ML by forming a $p(2 \times 2)$ overlayer structure [38-40]. Deposition of oxygen at higher temperatures enables an increase of the oxygen coverage. When θ_O exceeds 0.25 ML, the adsorption rate into the chemisorbed state becomes small and oxygen starts to penetrate into the subsurface, causing the reconstruction of the Pd substrate [39-41]. At higher oxygen coverages, a two-dimensional surface oxide is formed. The stoichiometry of the most stable surface oxide was identified as Pd_5O_4 by Lundgren, and reported to be an incommensurate overlayer resembling a $\sqrt{6} \times \sqrt{6}$ arrangement [42]. The oxygen coverage of Pd_5O_4 was measured to be 0.58 ML [41]. The Pd_5O_4 2D oxide is regarded as the well-ordered intermediate state between chemisorbed oxygen and bulk PdO phase. A precursor state toward PdO formation was found by Weaver to be oxygen atoms adsorbed on top of a 2D oxide surface [168]. Dissolution of oxygen into the bulk occurs at elevated pressures and temperatures, followed by the formation of bulk oxide PdO, which results in an increase of the inter-planar spacing between the first two layers [43].

The bulk oxide forms a “cauliflower-like” structure; the single crystal surface area increases, as well, during oxidation [43].

CO adsorption on O-Pd(111)

On an oxygen-adsorbed Pd(111) surface, the adsorption of CO causes a series of phase transitions of oxygen overlayer as evidenced by STM [169], LEED [28, 169, 170], and XPS [171]. Theoretical calculations, such as ab initio [172], DFT [170, 173], and Monte Carlo method [174] also support the experimental results. In brief, CO adsorption on $p(2 \times 2)$O-Pd(111) at first compresses the (2×2)O structure into a $(\sqrt{3} \times \sqrt{3})R30^{o}$ O phase, and then into a $p(2 \times 1)$O structure at a higher CO exposure. XPS studies show that the $p(2 \times 2)$-O phase is inert to CO at temperatures less than 290K, while in the $(\sqrt{3} \times \sqrt{3})R30^{o}$ O phase, the CO reaction with O occurs exclusively at island peripheries with a small apparent activation energy [171]. STM data also reveal that CO_2 formation only starts after the completion of the $(\sqrt{3} \times \sqrt{3})R30^{o}$ O structure [169]. CO was observed to adsorb on the bare Pd(111) surface instead of the oxygen island, different from Pt(111) and Rh(111) [169]. The $p(2 \times 1)$O phase was observed mostly at low temperatures (<200 K) of CO and is responsible for the reaction within this temperature range, while the reaction at the $(\sqrt{3} \times \sqrt{3})R30^{o}$ O phase mainly occurs at temperature higher than 200 K [171].

CO Adsorption on Pd(110)

Low-pressure CO adsorption

Low pressure CO adsorption on Pd(110) has been extensively studied for decades [34, 153, 175-184], especially by Raval et al. [178-182] . In brief, at low temperatures, for example at 180 K, the IRA spectra of CO adsorption display a single peak shifting to higher frequencies from low coverage to saturation [181]; at the saturation coverage ($\theta_{CO} = 1$), CO displays a vibrational frequency at 2003 cm^{-1} and a (2 × 1)-p1g1 LEED pattern. CO adsorption at 300 K, however, produces significantly different IRA spectra due to a reconstruction of the Pd (1 × 1) substrate into a missing-row (1 × 2) structure [176-178, 180]. It was reported that, at a critical coverage (θ_{CO}) of 0.3, a CO-induced structural alternation of the Pd substrate occurs and continues until θ_{CO} reaches 0.75. At a CO coverage between $0.3 < \theta_{CO} < 0.75$, the reconstructed and un-reconstructed Pd surfaces co-exist, resulting in a complicated infrared spectrum with multiple adsorption features over a nearly 300 cm^{-1} range. The reconstruction completes at $\theta_{CO} = 0.75$, exhibiting a sharp (4 × 2) LEED pattern. A further increase of CO coverage to $\theta_{CO} = 1.0$ lifts the reconstruction and the Pd surface reverts to the bulk (1 × 1) structure with a dominant CO feature at 2002 cm^{-1} in the IRA spectrum. However, when a (4 × 2)-CO surface formed at 300 K is cooled to 180 K, with further CO adsorption, a different spectrum is obtained with two CO stretching modes at 2108 and 1998 cm^{-1}, leading to a total coverage of 0.95 determined with TPD [183]. This is because at least 250 K is needed to convert the (1 × 2) substrate into (1 × 1) by CO adsorption [181].

Elevated-pressure CO adsorption

In spite of the large number of studies on CO adsorption at low pressures, there have been no vibrational spectroscopic studies of high pressure CO adsorption on Pd(110). PM-IRAS and SFG investigations of elevated pressure of CO adsorption on Pd(111) and SFG studies of Pd(100) have revealed that CO adsorption at high pressures is similar to that at UHV conditions and thus it can be inferred that no pressure-induced surface rearrangement occurs [19, 35]. In other words, there is no pressure gap of CO adsorption on Pd(111) and Pd(100) surfaces. Whether or not the same conclusion can be made on Pd(110) is investigated in the following section.

Fig. 40 displays PM-IRA spectra of CO on Pd(110) at 300 K at CO pressures from 0.03 to 10 Torr. At the lowest pressure, a strong bridging CO feature is found at 2000 cm^{-1}, accompanied by two much weaker atop features at 2099 and 2080 cm^{-1}. As the CO pressure increases, the intensity of the peaks remains almost unchanged and only slight shifts of these features are apparent. For instance, at a CO pressure of 10 Torr, the bridging CO is located at 2002 cm^{-1}, and the 2099 cm^{-1} feature shifts to 2103 cm^{-1}. The intensity of the feature at 2002 cm^{-1} increases a little, while the 2080 cm^{-1} signal bocames less resolved. Compared with the spectra obtained by Raval et al.[180-182], it is evident that CO adsorption at elevated pressures is very similar to that at UHV conditions. In addition, the spectra indicate that for all the pressures in Fig. 40, a saturation coverage (θ_{CO} = 1.0) is reached and no Pd substrate reconstruction occurs. The two more distinct atop features may be attributed to either the disorder of CO overlayer or the mismatch between compressed CO (4 × 2) overlayer and the Pd substrate.

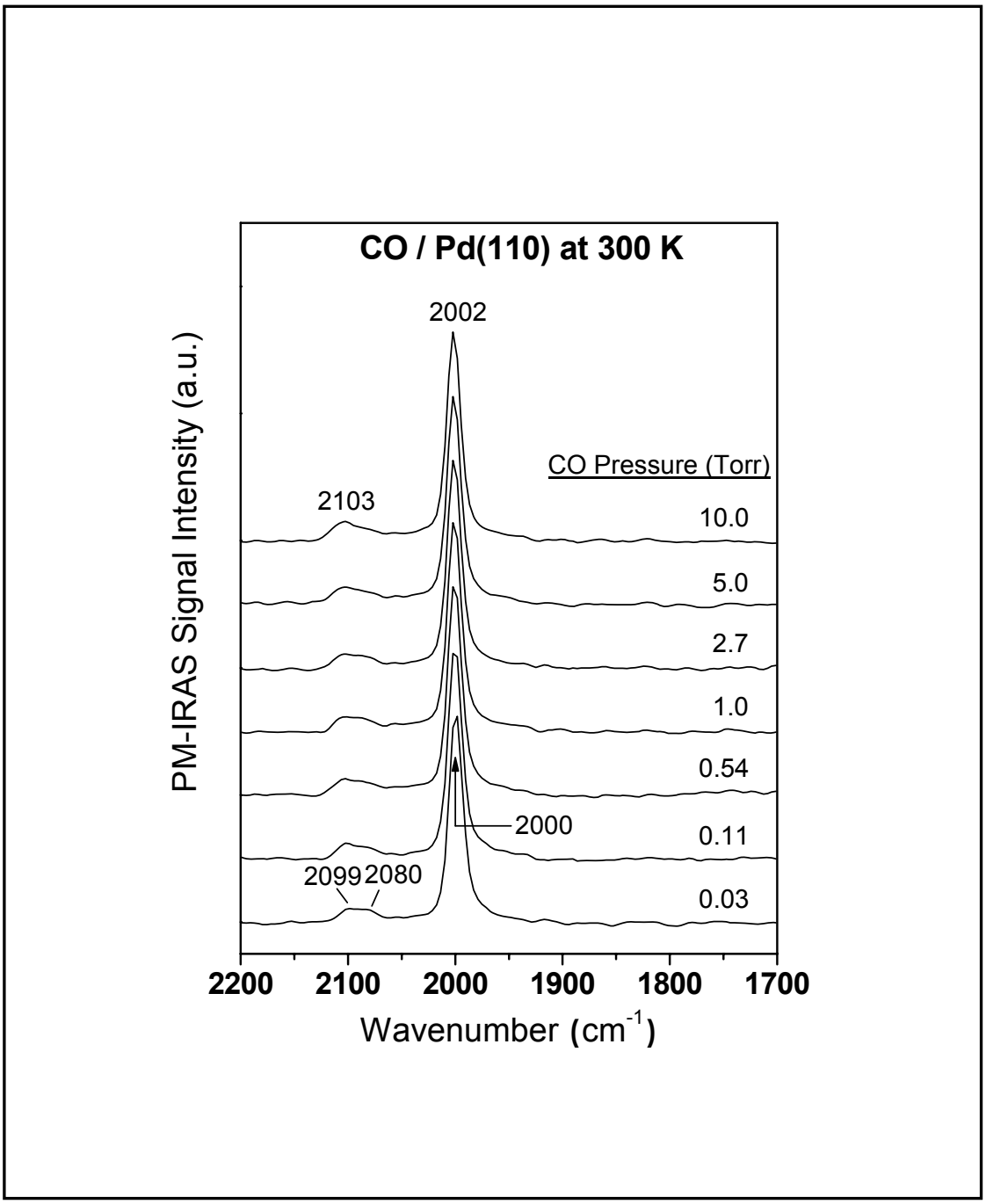

Fig. 40. PM-IRA spectra of CO adsorption on Pd(110) at 300 K. CO pressure is as indicated.

Similar phenomena were observed for high pressure CO adsorption on Pd(111) and Pd(100) [19, 34, 35, 153].

Fig. 41 shows the spectra for Pd(110) at 525 K, a temperature more relevant to practical CO oxidation, at various CO pressures ranging from 10^{-7} to 71 Torr. At CO pressures of 10^{-7} and 10^{-6} Torr, CO merely occupies two-fold short- the bridged sites with a coverage estimated at around 0.3. At a CO pressure of 10^{-5} Torr, the bridging feature blue-shifts to 1905 cm^{-1} and an atop CO signal develops at 2057 cm^{-1}. The comparison of the spectra at 525 K (Fig. 41) with one of known coverage (Fig. 40) suggests that a CO pressure of 10^{-5} Torr at 525 K leads to a coverage of 0.75 and a $c(4 \times 2)$ overlayer on a missing-row (1×2) Pd surface. As the CO pressure is increased to 10^{-4} Torr, the CO vibrational feature at 1909 cm^{-1} shifts further to higher frequencies and another bridging feature appears at around 1950 cm^{-1}. As is known from studies by Raval [180-182], at a CO coverage higher than 0.75, the Pd(110) substrate reverts from the (1×2) missing row structure back to the (1×1) structure. The appearance of the two bridging features suggests that the Pd substrate may undergo a phase transition which results in the coexistence of CO islands with different arrangements. With a further increase of the CO pressures, a general trend follows where both the bridging and atop CO signal frequencies increase as the CO pressure increases. Finally, at a CO pressure of 72 Torr, the atop and bridging CO features are found at 2073 and 1990 cm^{-1}, respectively. It was also found that the signal intensities for bridging CO are always stronger than those for atop species at any given CO pressure measured. From the ratio of infrared intensities of atop and bridging features, it may be safe to estimate the coverage of CO at

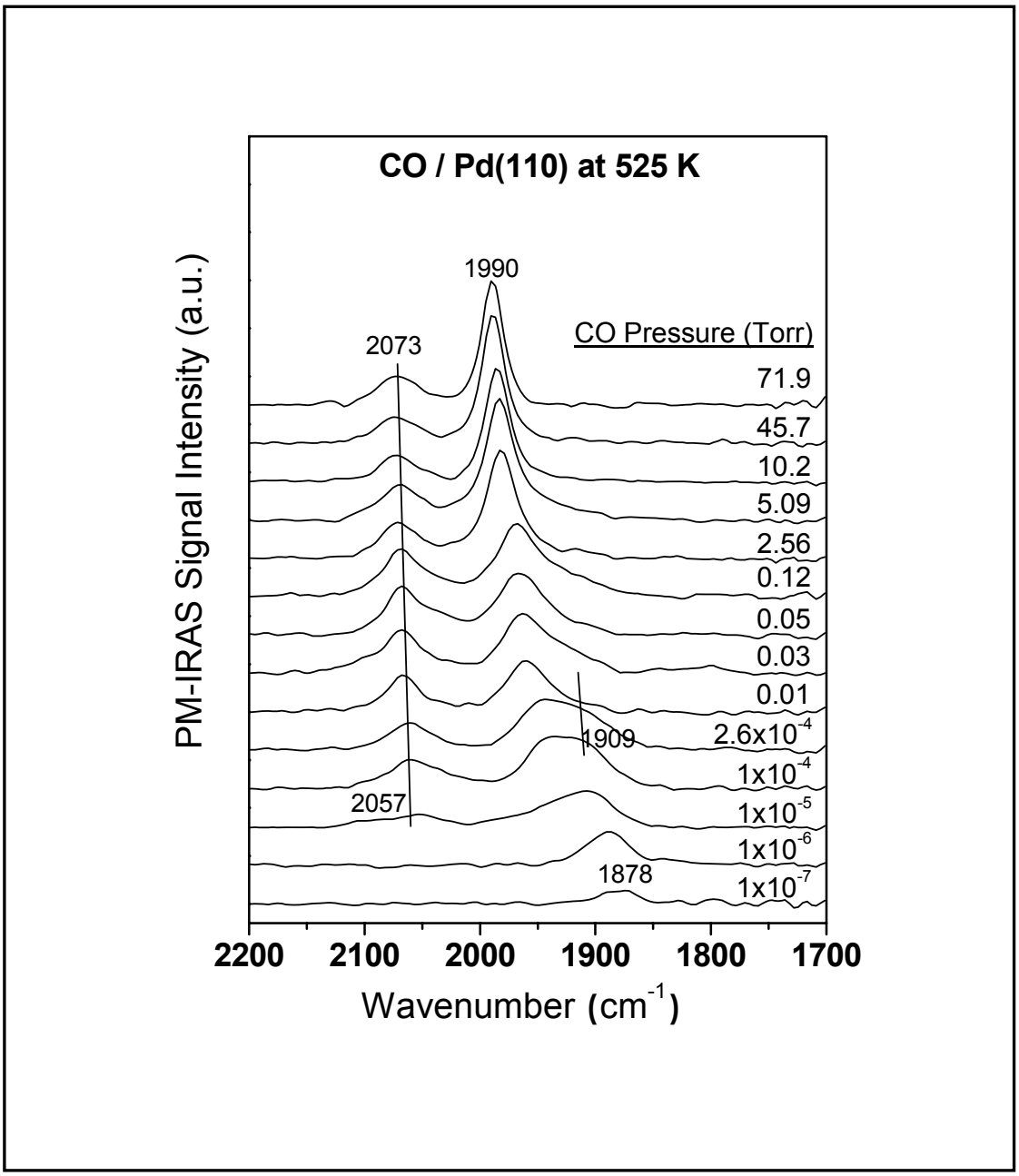

Fig. 41. PM-IRA spectra of CO adsorption on Pd(110) at 525 K. CO pressure is as indicated.

around 0.9 ML at 525 K under pressures up to 70 Torr.

CO Titration on Oxidized Pd(110)

Fig. 42 displays AES spectra acquired at room temperature following oxidation of Pd(110) with 10 Torr of O_2 for 5 min at various temperatures. In the above oxidation process, the sample was heated and cooled in the presence of oxygen. The oxygen amount left on the surface would be much less if oxygen was pumped out during the cooling. The corresponding peak-to-peak O/Pd ratio is marked adjacent to each spectrum. As shown, at low reaction temperatures 300 and 450 K, low O/Pd ratios are found. However, when the sample temperature was held at 525 K and above, the O/Pd ratio becomes much higher. Note that chemisorbed oxygen, for example, $c(2 \times 4)$-O formed by reacting 30 L of O_2 with clean Pd(110) at 450 K (O coverage 0.5 ML), is almost undetectable with AES since it is easily removed from the surface by the high-energy electrons (data not shown). Therefore, it is clear, since under all oxidation conditions oxygen was detected with AES, that oxygen penetration into the subsurface region must have occurred. As previously described, the formation of stoichiometric PdO is characterized by 1) a decrease of oxygen uptake rate, 2) the complete attenuation of the metallic Pd LEED pattern, 3) the 0.15-0.7 O/Pd atomic ratio with AES, and 4) the 1.8 eV binding energy shift for the core-level Pd $3d_{5/2}$ peak [43, 185]. Accordingly, it is concluded that at reaction temperatures of 300 and 450 K, surface oxides are formed, while at 525 K and above, bulk-like PdO films are generated.

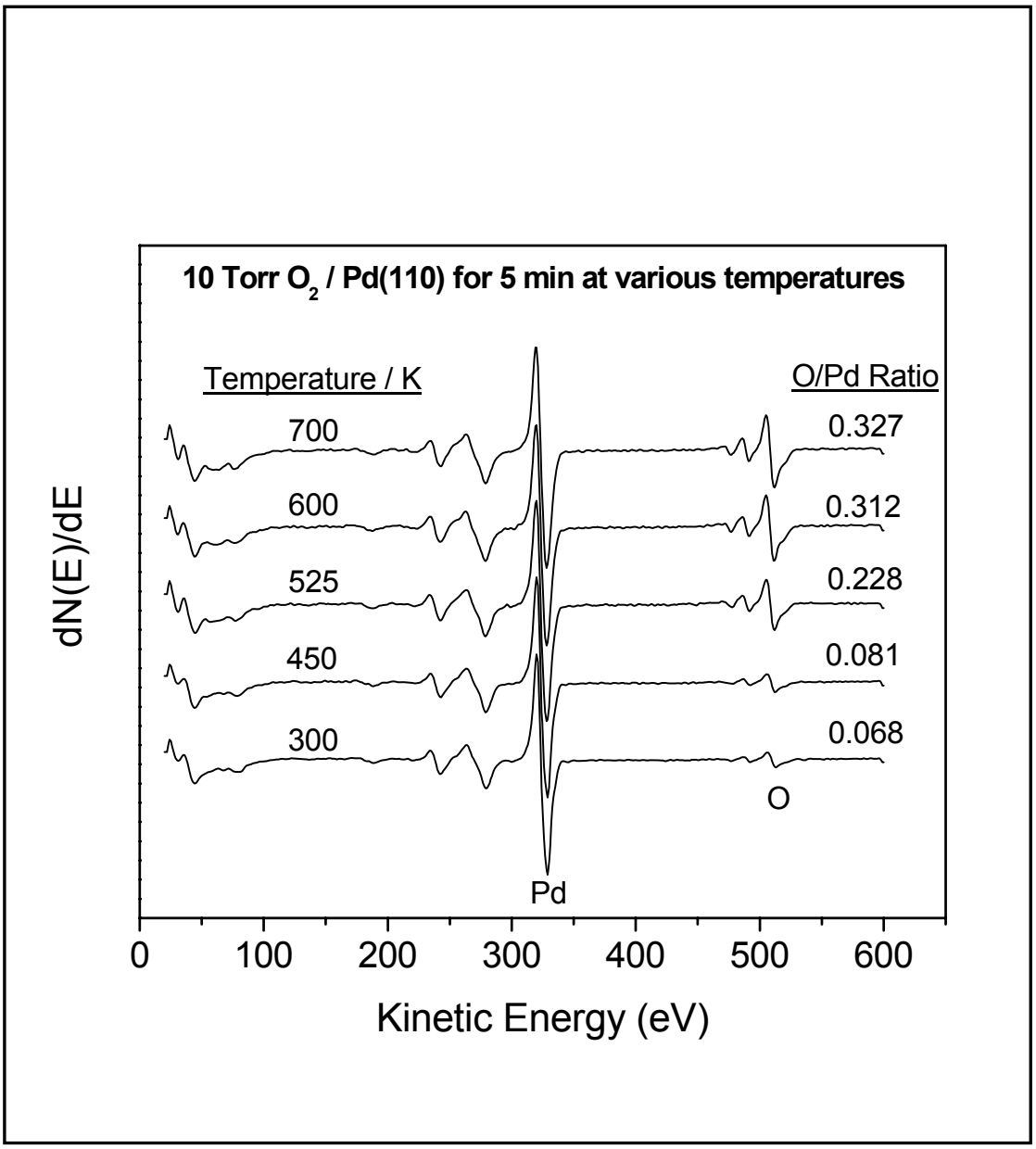

Fig. 42. Auger Electron Spectra of Pd(110) surface after oxidation in 10 Torr oxygen for 5 min at various temperatures.

The reactivity of the surface and bulk oxides on Pd(110) were examined with CO titration. Fig. 43 displays the results with a surface oxide formed by reacting 10 Torr of O_2 with clean Pd(110) at 300 K for 5 min (O/Pd Auger ratio 0.068, Fig. 42). Following exposure of CO at 100 and 125 K, a strong atop CO band is found at 2139 cm^{-1}. Meanwhile, there might also be some extremely weak CO feature between 1950 and 2000 cm^{-1}. The high frequency CO feature is often observed in oxide supported metal catalysts, for example, ν(CO) at 2135 cm^{-1} on Pd/Al_2O_3 [186]. On single crystal surfaces, 2130 cm^{-1} was observed on Rh(111) (in previous chapter), and 2125 cm^{-1} was observed on Pd(100) which was attributed to the CO-Pd-O complex. The 2139 cm^{-1} feature was also found by Iwasawa et al. [183] on a Pd(110)-*c*(2 × 4)-O surface where it was assigned to a CO species linearly bound to a first layer Pd atom, which is directly coordinated by oxygen atoms. From the above assignments, it can be inferred that 2139 cm^{-1} in Fig. 43 is associated with CO on Pd surface oxide as described by Iwasawa. The CO vibrational feature does not change upon further exposure of the surface oxide to CO at 125 K, suggesting that no reaction between CO and the surface occurs at this temperature. However, when the sample was annealed to 180 K in 0.1 Torr of CO, new features appear at 2114 and 1990 cm^{-1}. The 1990 cm^{-1} feature can clearly be assigned to a bridging CO band and the 2114 cm^{-1} peak can be assigned to an atop CO adsorbed on Pd atoms that are not coordinated to oxygen atoms [183]. This clearly demonstrates that the reduction of the surface oxide occurs as low as 180 K. As shown in Fig. 43, exposing the surface oxide in 0.5-5 Torr of CO at 200-210 K partially reduces the surface as

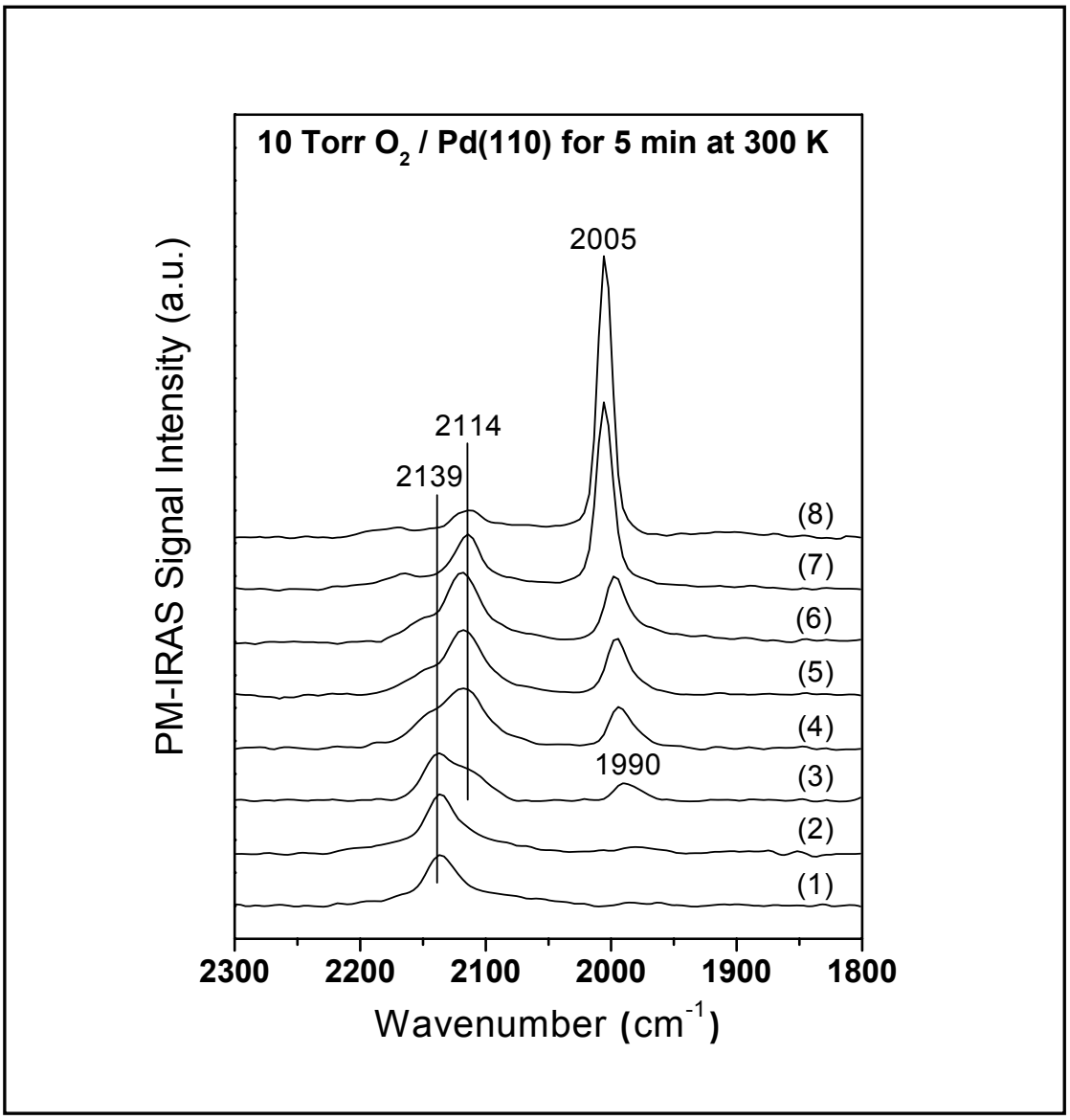

Fig. 43. CO adsorption on Pd(110) pretreated in 10 Torr oxygen at 300 K for 5 min. (1) 100 K, 10^{-5} Torr; (2) 125 K, 0.01 Torr; (3) 180 K, 0.1 Torr; (4) 200 K, 0.5 Torr; (5) 200 K, 1 Torr; (6) 210 K, 2.5 Torr; (7) 300 K run 1 min, cool to 210 K; (8) 350 K run 1 min, cool to 210 K.

evidenced by the growth of νCO at 2114 cm^{-1} at the expenses of the peak at 2139 cm^{-1}. However, the sample cannot be completely reduced to metallic Pd until it was heated to 300K. This means that the barrier for subsurface oxygen to diffuse to the topmost of the surface cannot be overcome at these temperatures. Rather, by keeping the sample at 350 K for 1 min, the Pd sample is completely reduced. Again, this temperature is still relatively low, demonstrating the high reactivity of the Pd surface oxide.

Fig. 44 displays the adsorption and reaction of CO on a bulk oxide formed by reacting 10 Torr of O_2 with clean Pd(110) at 525 K for 5 min (O/Pd Auger ratio 0.228, Fig. 42). First, the sample surface is unable to adsorb CO even at a temperature as low as 100 K. Comparing the results shown in Figs. 43 and 44, it can be immediately concluded that a surface oxide is substantially more reactive than a bulk oxide. By warming the sample to 170 K in 0.05 Torr of CO, a very weak CO band occurs at 2140 cm^{-1}. The weakness of this band indicates that the concentration of surface sites where CO can adsorb is low and likely to be surface defects. The possible origin of the occurrence of the 2140 cm^{-1} is thus explained as the follows: 1) CO reacts with the more reactive surface defect sites at 170 K to form CO_2, which desorbs immediately; 2) the open sites generated are then occupied by CO molecules, giving rise to the 2140 cm^{-1} signal. The high vibrational frequency indicates that surface Pd atoms where the CO molecules adsorb onto are coordinated directly with oxygen [183]. By warming up the sample to 210 K and increasing the CO pressure to 1 and 5 Torr, no change of the 2140 cm^{-1} feature is observed. In the meantime, no other CO species are found on the surface. This means the CO adsorbed on the surface does not continuously react with

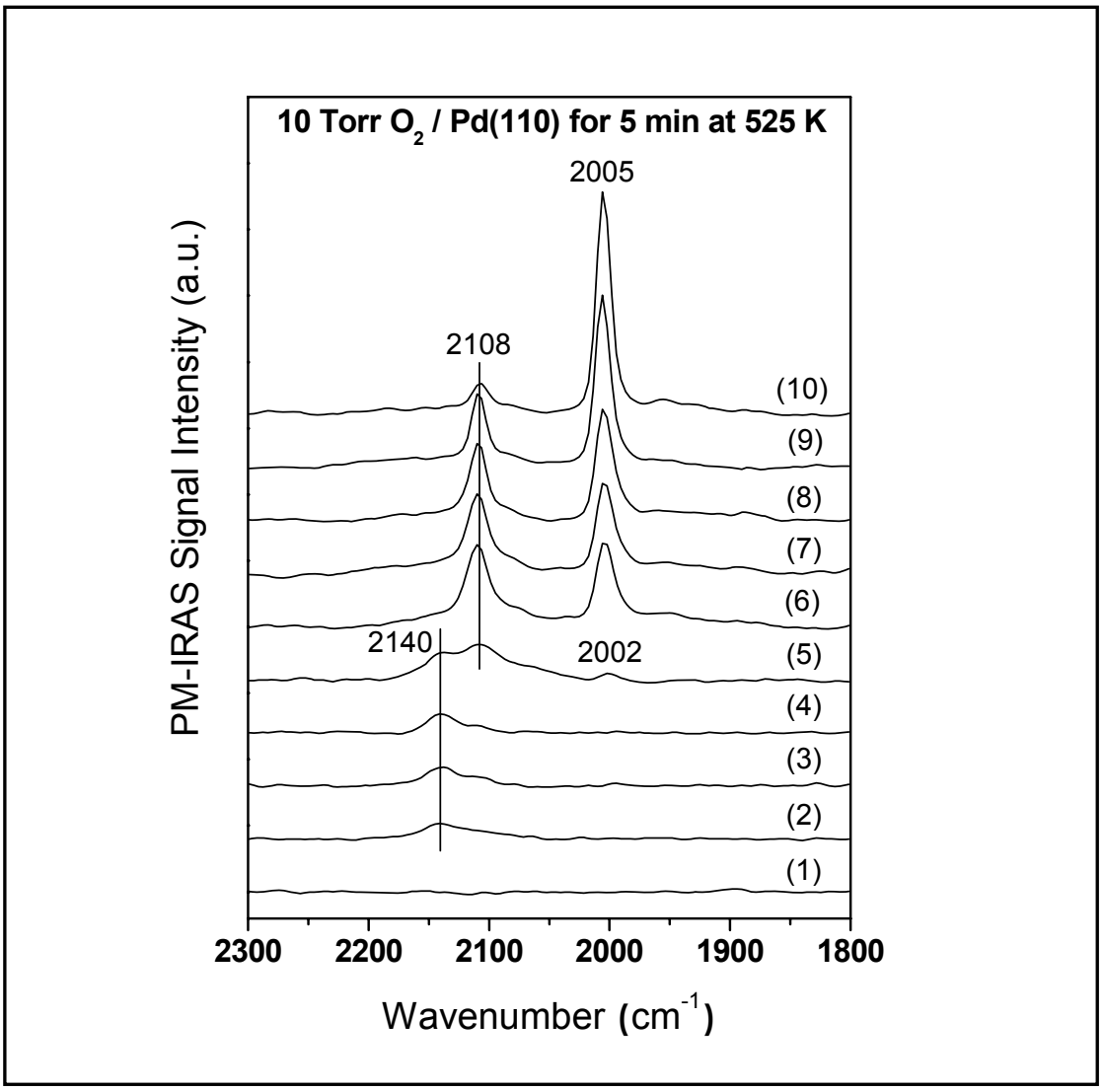

Fig. 44. CO adsorption on Pd(110) pretreated in 10 Torr oxygen at 525 K for 5 min. (1) 100 K, 10^{-5} Torr; (2) 170 K, 0.05 Torr; (3) 210 K, 1 Torr; (4) 210 K, 5 Torr; (5) 300 K run 1 min, cool to 210 K (6) 350 K run 1 min, cool to 210 K; (7) 2^{nd} 350 K run 1 min, cool to 210 K; (8) 3^{rd} 350 K run 1 min, cool to 210 K; (9) 400 K run 1 min, cool to 210 K; (10) 450 K run 1 min, cool to 210 K.

surface oxygen at this temperature. Further reduction of the sample occurred when the sample was annealed to higher temperatures in CO (5 Torr). This is evidenced by the appearance of new CO features at 2108 and 2002 cm^{-1} when the sample was kept at 300 K for 1 min. The sample is reduced further by warming to 350 K for 1 min, where the 2140 cm^{-1} signal disappears completely. However, the reduction did not sustain a high rate at 350 K. As shown in the figure, the intensity of the CO features at 2108 and 2005 cm^{-1} does not vary much when the sample was kept in 350 K and 5 Torr of CO for two more minutes. Only when the sample temperature was increased to 450 K did the sample completely reduce to metallic Pd within 1 min as evidenced by the characteristic CO adsorption spectrum at saturated coverage.

CO adsorption and reaction on a bulk oxide formed by oxidizing in 10 Torr O_2 for 5 min at 700 K (O/Pd Auger ratio 0.327) was also studied and the results are shown in Fig. 45. No CO adsorption is found when the sample is exposed to 5 Torr of CO at 210 K. Note that this situation is different from the bulk oxide formed at 525 K, where atop CO does appear at 170 K (Fig. 44). It is possible that the bulk oxide formed at 700 K is "defect free," i.e., no surface sites appear for CO occupation at low temperatures.

Following the same reduction procedure shown in Fig. 44, this bulk oxide can also be reduced to metallic Pd by CO. However, this bulk oxide is apparently more difficult to reduce. Most evidently, the bridging CO feature at ~2000 cm^{-1} only appears, still rather weak, after the reaction at 400 K. For the bulk oxide formed at 525 K, this feature appears as low as 300 K. At least two new CO species at 1955 and 1892 cm^{-1} appear during the reduction of this bulk oxide, indicating that the surface becomes rather

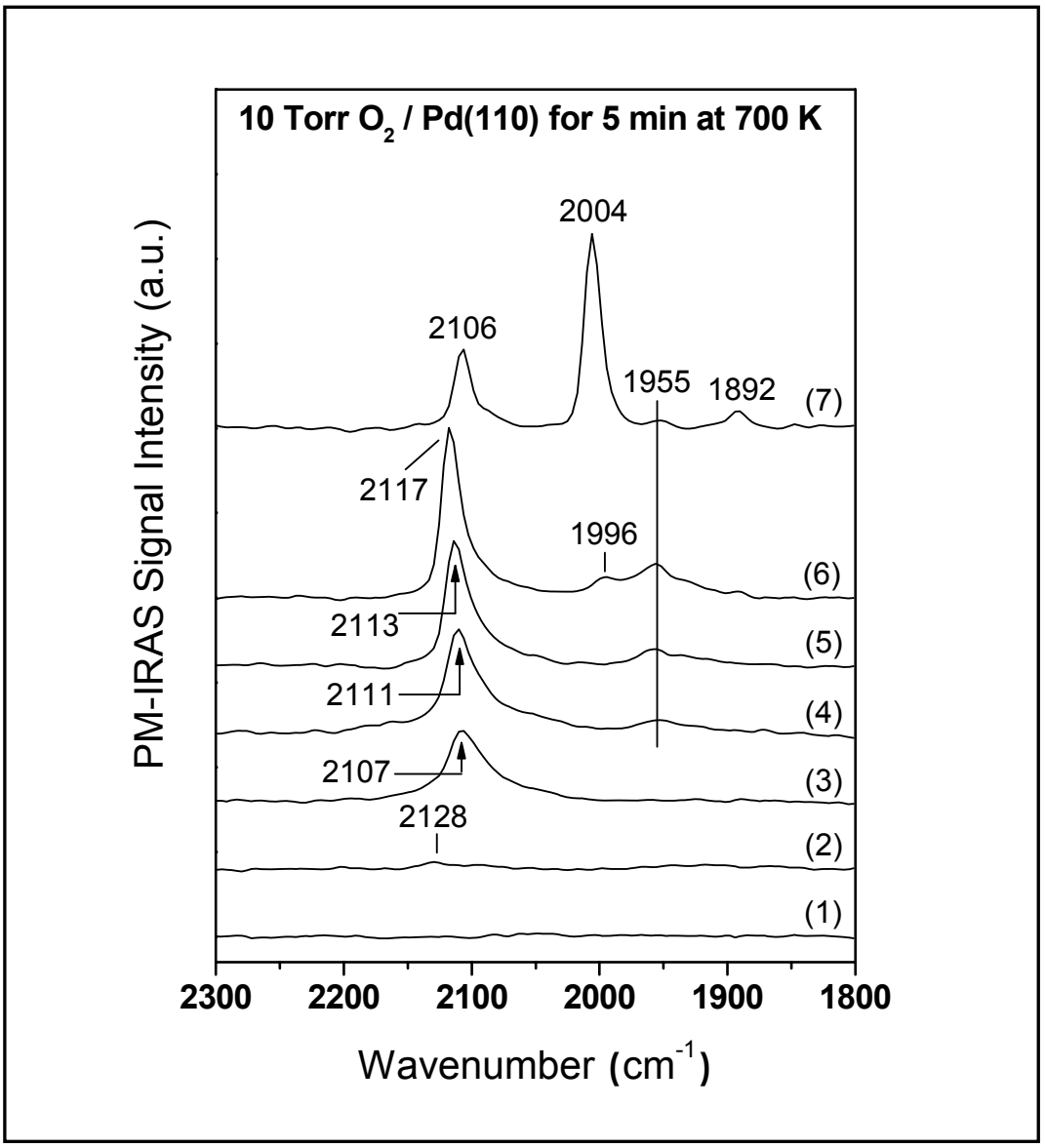

Fig. 45. Five Torr of CO adsorption at 210 K on Pd(110) pretreated in 10 Torr oxygen at 700 K for 5 min. Pretreatment: (1) 210 K; (2) kept at 300 K 1 min; (3) kept at 350 K 1 min; (4) 2nd kept at 350 K 1 min (5) 3rd kept at 300 K 1 min; (6) kept at 400 K 1 min; (7) kept at 450 K 1 min.

inhomogeneous during the oxidation-reduction process.

AES data shown in Fig. 42 are only of qualitative significance that allows for the identification of surface and bulk oxides. In terms of oxygen coverage and film thickness, other techniques such as XPS, LEED, and TPD are needed to obtain more detailed surface information. Fortunately, much previous work allows a relatively clear picture to be drawn [185]: At low oxygen exposures, (1 × 2) reconstruction on a Pd substrate occurs and a *c*(2 × 4)-O structure is formed at $\theta = 0.5$. When the amount of adsorbed oxygen increases from 0.5 to 1.7 ML, oxygen penetrates into the subsurface region to a depth exceeding 15-20 Å while remaining the *c*(2 × 4)-O structure. When the amount of adsorbed oxygen is between 2-5 ML, the surface is subjected to reconstruction with the formation of a surface oxide with $\theta \sim 0.8$. Further increase of the amount of adsorbed oxygen beyond 5 ML leads to oxygen location in the subsurface region, forming PdO clusters. Finally, the clusters grow to form a continuous layer of PdO.

In Fig. 43, one important feature of the surface oxide formed at 300 K is that the surface is able to adsorb CO at low temperatures; moreover, the CO vibrational frequency at 2139 cm^{-1} is identical to that on a Pd(110)-*c*(2 × 4)-O surface [183]. This indicates that the topmost of the surface remains a *c*(2 × 4)-O structure, or at least some *c*(2 × 4)-O domains are still present. Judging from this, the amount of adsorbed oxygen is below 5 ML and the surface oxygen coverage should be between 0.5 and 0.8. The CO titration results demonstrate that this surface is very active towards CO oxidation reaction in that the reaction starts as low as 180 K and full reduction finishes at 350 K. Note that surface oxide formed at 450 K (Fig. 42) has very similar reactivity (data not

shown).

In contrast, both bulk-like oxides are much more difficult to reduce, i.e., they show much reduced reactivity for CO oxidation (Fig. 44 and 45). Although this is a known phenomenon [183, 187], several points are still worth discussing. First, although the bulk oxide formed at 525 K is unable to adsorb CO at 100 K, it becomes capable of adsorbing a small amount of CO at 170 K (Fig. 44). The vibrational frequency of 2140 cm^{-1} indicates that CO stays on top of Pd atoms that are coordinated directly with oxygen. The fact that these sites are unavailable at 100 K clearly indicates that these are created at 170 K, presumably due to the reaction between CO and reactive surface defect sites. On the other hand, bulk oxide formed at 700 K cannot adsorb any CO even at 210 K (Fig. 45). It can thus be concluded that in the latter case, as the oxide is formed at a higher temperature, the concentration of surface defects is extensively reduced. Although there could be other explanations, this is certainly one reason that makes bulk oxide formed at 525 K easier to reduce than the bulk oxide formed at 700 K. Recently it has been shown that a Pd surface oxide with richer defect sites is more reactive towards CO [164].

The PM-IRA spectra also reveal more detailed differences on the reduction process of the two bulk oxides. In Fig. 44, CO bands at 2108 and 2002 cm^{-1} appear concurrently at 300 K (spectrum 5). Since these two bands also exist on a clean Pd(110) surface [183], it can be inferred that clean Pd domains have already formed, or at least domains with very low oxygen coverages have formed. The increase of the signal intensity at higher reduction temperatures indicates the expansion of these domains,

which continues until the whole sample is reduced to clean Pd(110). In contrast, as displayed in Fig. 45, the reduction of the bulk oxide formed at 700 K is very different. First, an extremely weak CO band never seen on other surfaces appears at 2128 cm^{-1} at 300 K. This band could be analogous to the 2140 cm^{-1} band seen in Fig. 44 that occurs at 170 K, i.e., caused by the reaction on surface defects. This means the surface defects only become active at 300 K. When the sample was subjected to CO reduction at 350 and 400 K, the dominant surface species is atop CO at 2107-2117 cm^{-1}. In the meantime, broad and weak bridging CO species were detected at lower frequencies. The fact that CO predominately stays at atop sites with rather high vibrational frequency strongly indicates that the reduced surface Pd atoms are profoundly affected by subsurface oxygen. Finally, the appearance of the stronger bridging CO species at 2004 cm^{-1} at 450 K indicates that the bulk oxide has been largely reduced to metallic Pd. On this surface at least four different CO species are apparent, indicating that the surface becomes rather inhomogeneous, consistent with previous STM studies [188] where an amorphous metallic surface was produced after H_2 reduction at 373 K.

CO Oxidation on Pd and Pt

Steady-state reactions at low pressures

Low pressure CO oxidation on Pd and Pt surfaces has been extensively studied previously and reaction mechanism and kinetics are very well understood [20]. Nevertheless low pressure reaction kinetics was performed in the present study to make

correlations between low- and high-pressure regimes.

Fig. 46 displays such an example using Pd(100) as the model catalyst and reacting in an 1:1 O_2/CO mixture at a CO partial pressure of 1×10^{-6} Torr. The CO_2 formation rate (represented as TOF) at various temperatures is plotted in Fig. 46a. Fig. 46b presents the corresponding PM-IRA spectra at different temperatures. Under this reaction condition, only bridging CO features that red-shift with increasing temperature were detected. In these figures several points need to be discussed. First, the reaction can be roughly divided into two regimes: a low-rate regime on a CO-dominant surface and a high-rate regime (>= 500 K) where surface CO coverage is below the detection limit of IRAS, i.e., below ~0.01 monolayer. Second, it is seen that at any given reaction temperature, the reaction rate maintains very constant with time. Note that this is rather distinct from Rh(111), for which under the same reaction conditions, the reaction rate does drop with time at relatively high temperatures. This suggests that oxygen inhibition found with Rh(111) does not exist with Pd. Finally, CO PM-IRA spectra display lineshapes and vibrational frequencies similar to CO on clean Pd(100) at 475 K and below at the same gas pressure (1×10^{-6} Torr) [153] . This suggests that under steady-state conditions, at temperatures lower than 475 K, enough CO is still present on the surface and the oxygen coverage is not high enough to alter the adsorption of CO. At temperatures higher than 550 K, the reaction rate starts to drop slowly due to a reduction of the sticking probabilities of both CO and O_2.

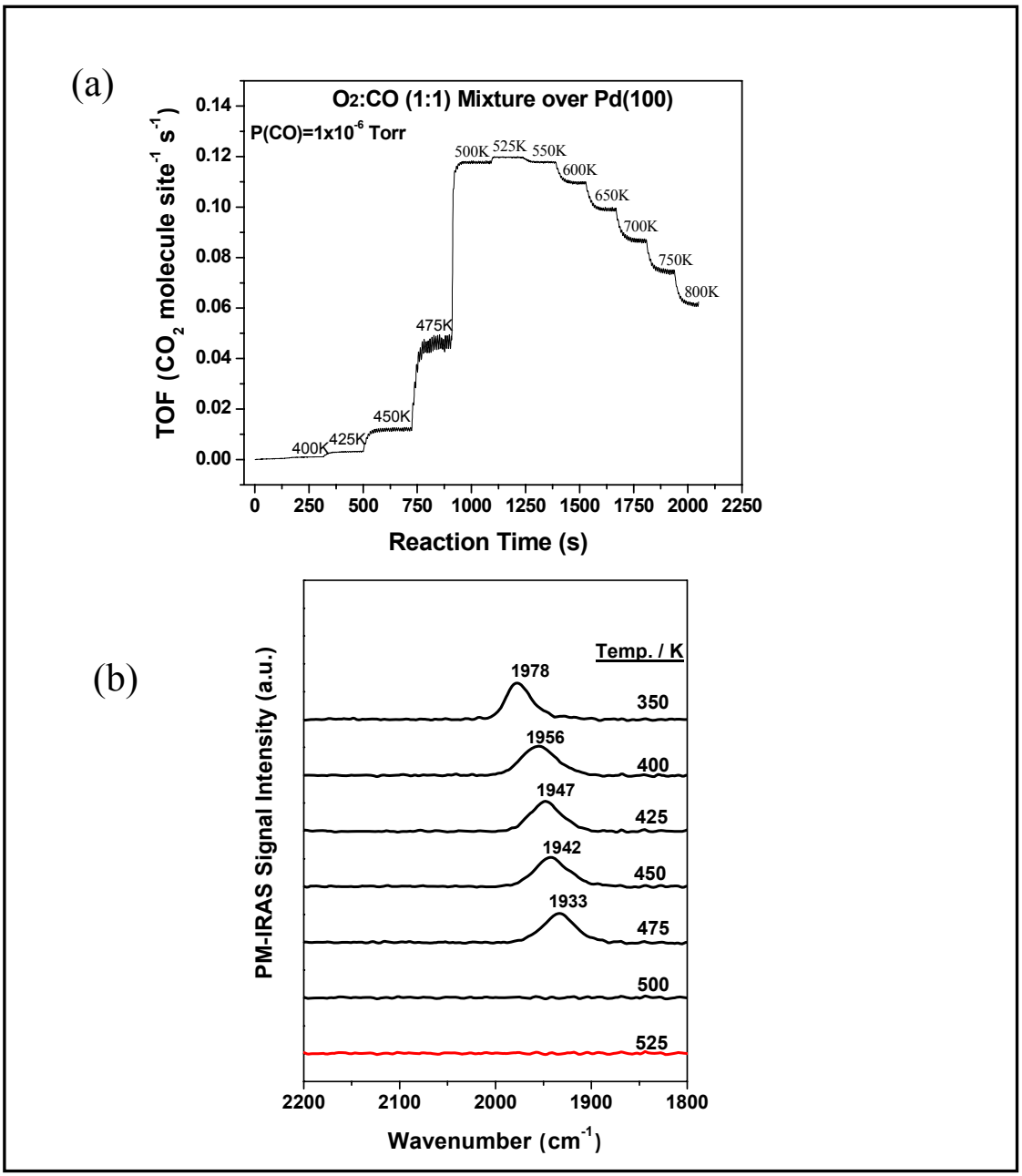

Fig. 46. CO oxidation on Pd(100) in 1:1 O_2/CO mixture at a CO partial pressure of 1.0×10^{-6} Torr. (a) CO_2 formation rate as a function of reaction time on. (b) PM-IRA spectra corresponding to (a).

Fig. 47 displays the steady-state reaction on Pd(110) in 10:1 O_2/CO mixture at the CO partial pressure of 1.0×10^{-8} Torr. A very prominent increase in the rate occurs during the transition from the low rate to the high rate regime. Similar phenomena were observed on Rh(111) and Pd(100), but those on Pd(110) were more pronounced. Again, as mentioned in the previous chapter, at higher partial pressures of CO, this sharp increase in rate is not observed or is less apparent. Hence, it is reasonable to deduce that this rate surge is associated with the supply of CO to the surface. Another noticeable phenomenon is the hysteresis in rate and the concurrent change in the infrared spectrum (Fig. 47b). In the course of heating, at 370 K the sample surface is covered by CO and the reaction rate is low. During the cool down, at 370 K the reaction rate is still high and no detectable CO is found. Again, these data demonstrate a correlation between the reaction rate and the surface states, i.e., on Pd catalysts, surfaces with no detectable CO (presumably oxygen-covered surfaces) exhibit a higher rate than CO-covered surfaces.

Similar steady-state experiments were also performed with reactants of various O_2/CO ratios (from 1/2 to 10/1) and various CO pressures (from 1×10^{-8} to 1×10^{-3} Torr) over Pd(100), (111), (110), and Pt(110) surfaces. Similar results were obtained. As an example, Fig. 48 shows the ratio of CO signal area (normalized by the maximum signal intensity) (y on the left, represented as solid circles) and reaction rate (y on the right, represented as empty triangles) as a function of reaction time on Pd(100), Pt(110), and Rh(111). The results displayed in Fig. 48 are all under the same gas composition, i.e., 1:1 O_2/CO and a CO partial pressure of 1×10^{-6} Torr. It is evident that on all three single crystals, CO_2 formation rate maximizes when the CO signal is close to zero, in full

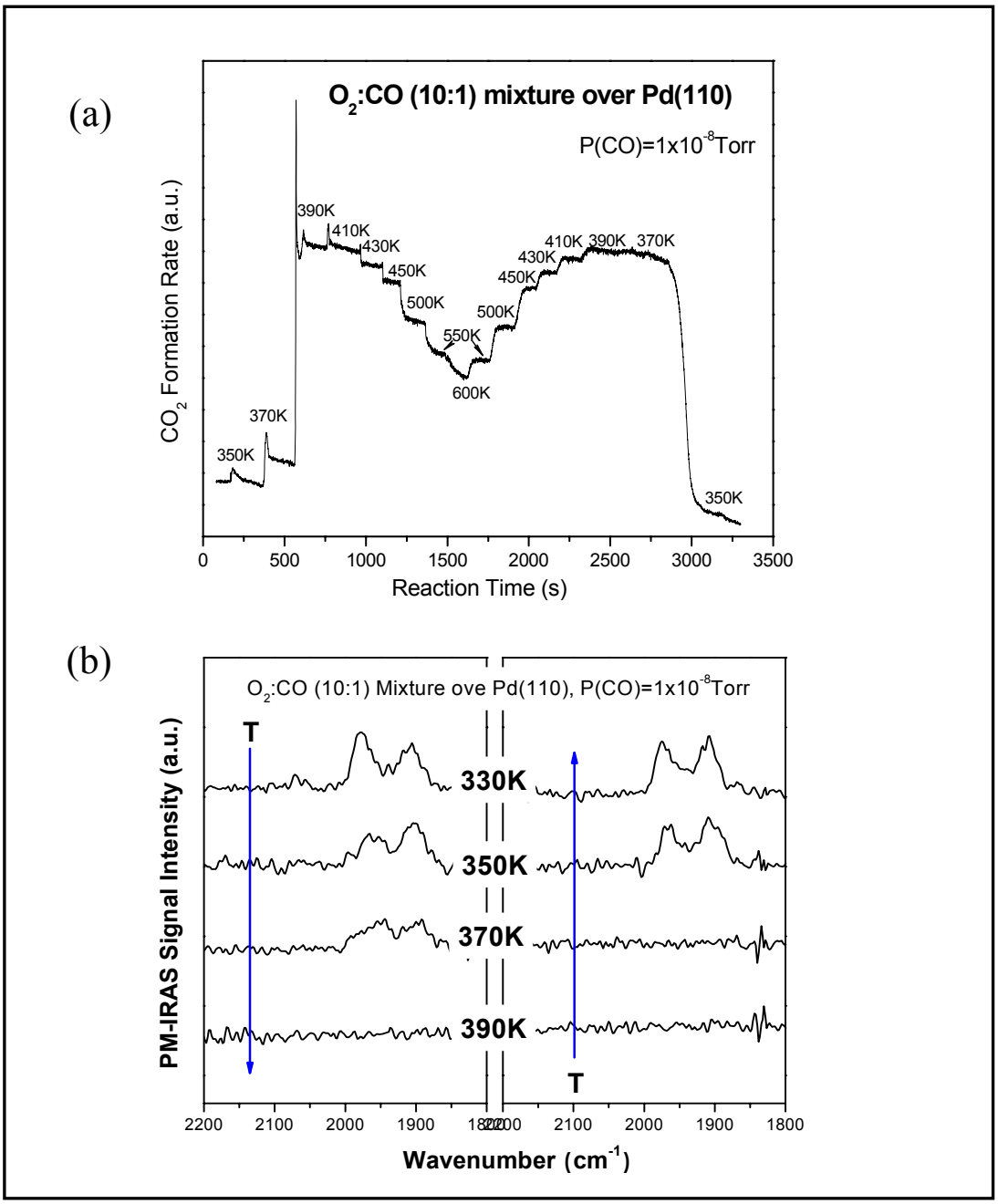

Fig. 47. CO oxidation on Pd(110) in 10:1 O_2/CO mixture at a CO partial pressure of 1.0 × 10^{-8} Torr. (a) CO_2 formation rate as a function of reaction time at different temperatures. (b) PM-IRA spectra corresponding to (a). Blue arrows indicate the directions that the experiments were performed.

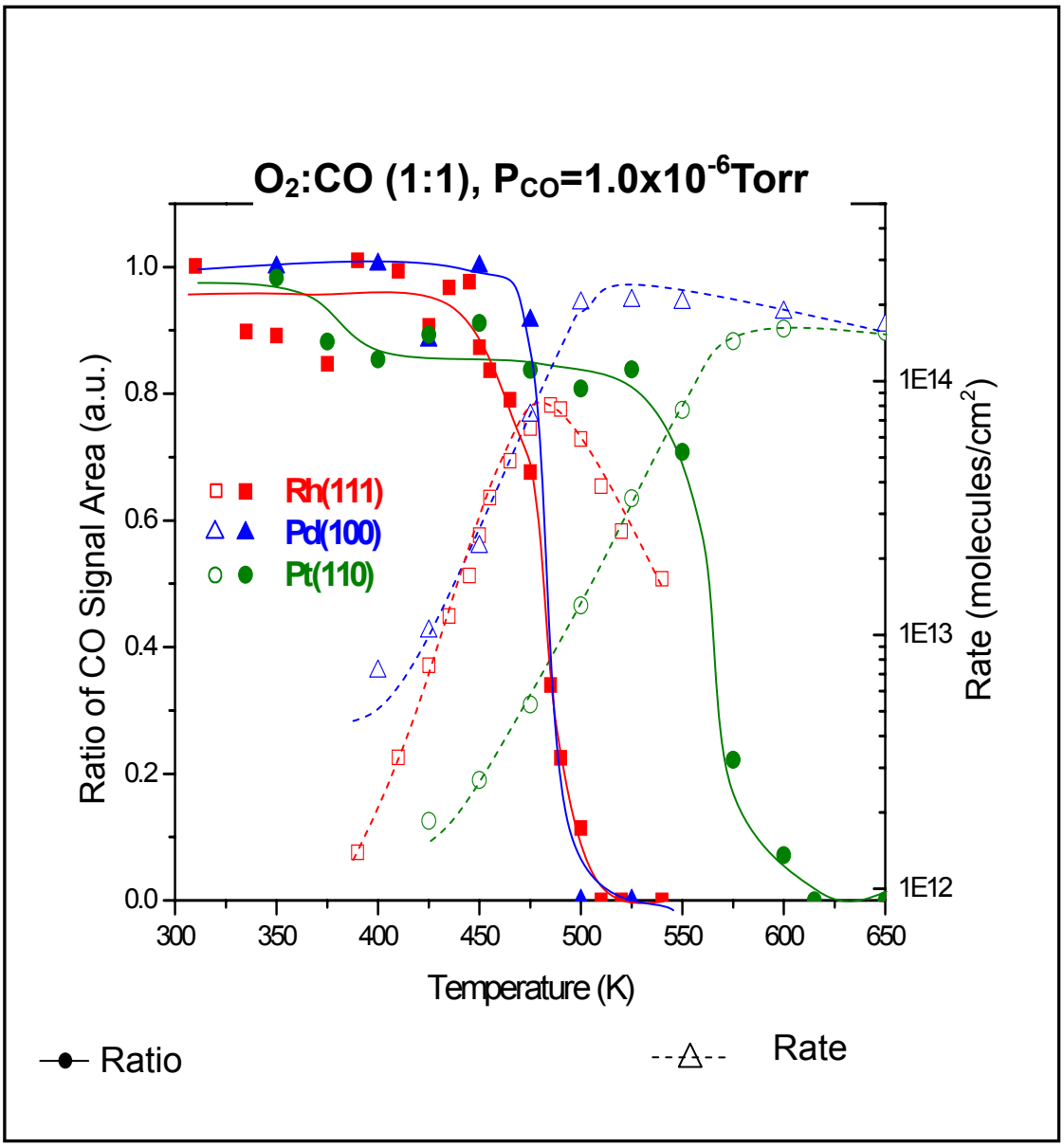

Fig. 48. Ratio of CO signal area and reaction rate as a function of reaction temperature on Pd(100), Pt(110), and Rh(111) in 1:1 O_2/CO mixture at a CO partial pressure of 1 × 10^{-6} Torr.

agreement with Schwartz's results [140]. Moreover, the reaction data on Pd, Rh, and Pt can be explained by the sequence of CO binding energies to these metals [20]. Note that for reactants of other O_2/CO ratios, similar results were found.

Fig. 49 represents the reaction probabilities at various partial pressures of CO. As shown, as the CO partial pressure is increased from 1×10^{-8} to 1×10^{-4} Torr, the maximum reaction probability remains constant with a value around 38%. At a CO partial pressure of 1×10^{-3} Torr, however, the reaction probability at the maximum rate dropped to ~23% and dropped still further at higher CO partial pressures, which will be shown later. Hence, it can be inferred that at 10^{-3} Torr of CO partial pressure, mass transfer limitation begins to affect the reaction and needs to be taken into account in the interpretation of data above this pressure. It is also noteworthy that it requires more than 150 K change in temperature to reach the maximum rate at $P_{CO} = 10^{-3}$ Torr, while only 100 K is required for other partial pressures of CO.

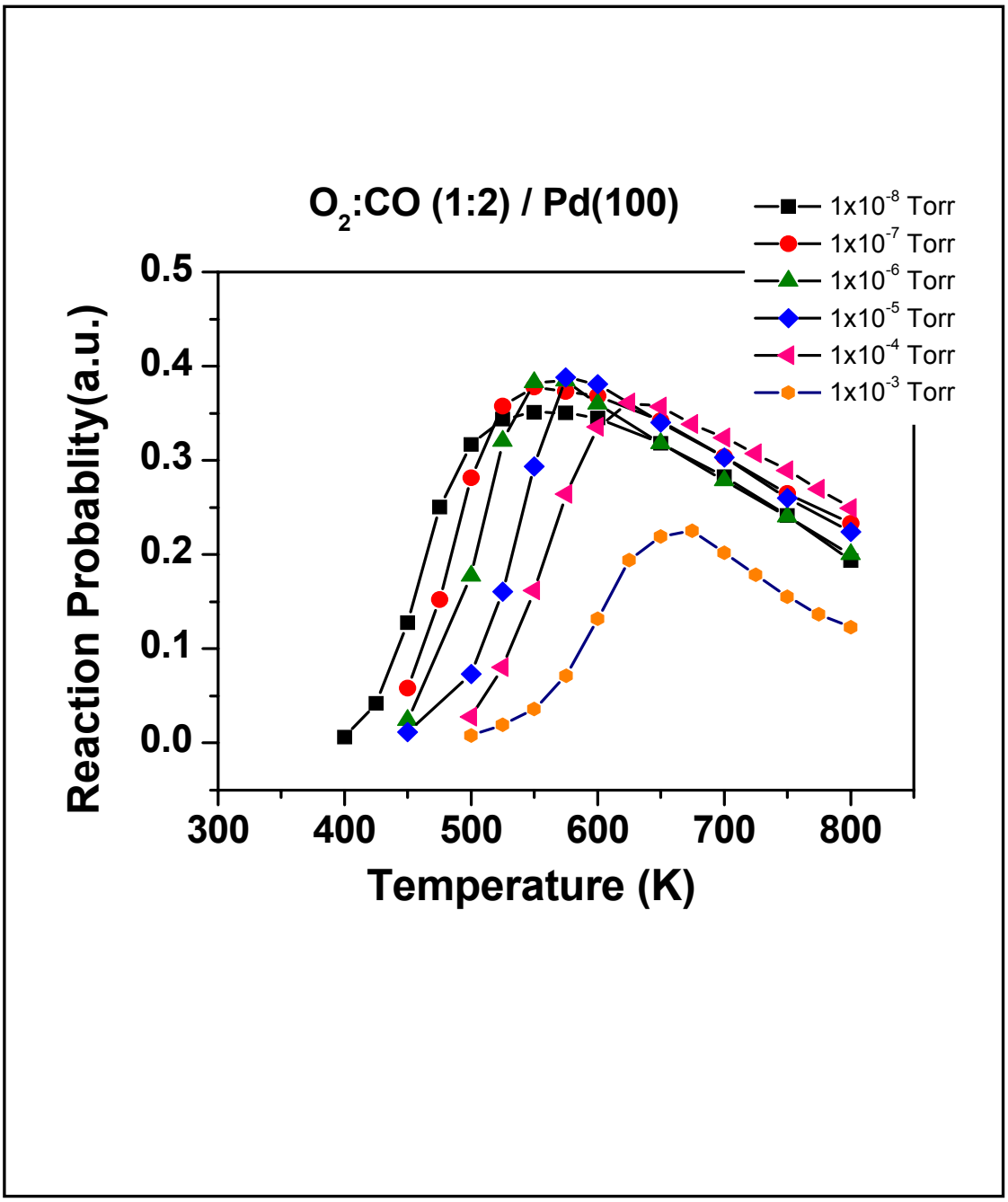

Fig. 49. Reaction probability of CO oxidation as a function of temperature on Pd(100) in 1:2 O_2/CO mixture at various partial pressures of CO.

High pressure batch reactions

Most high pressure reactions were performed by pressurizing the whole UHV chamber (61.6 L) with O_2/CO gaseous mixtures; subsequently, the Pd and Pt samples (located within the infrared cell) were heated to various temperatures to carry out CO oxidation. Reaction rates were calculated using the pressure change of the gas phase, which is monitored using a Baratron gauge. PM-IRAS spectra were acquired at each reaction temperature to monitor the surface CO species. CO conversion was generally kept below 10% to main a pseudo steady-state condition.

Fig. 50 displays a typical example of such measurements in a 1:1 O_2/CO mixture at an initial CO partial pressure of 8 Torr. In Fig. 50a, the orange thick solid line represents the pressure change (as indicated by the arrow), the thin stair-shaped line represents the reaction temperature (corresponds to y-axis on the right), and the number above each stair represents the corresponding reaction rate (TOF) at that temperature. Fig. 50b presents the corresponding PM-IRA spectra at various reaction temperatures. Similar to what has been observed on Rh(111), three reaction regimes were noticed. In the first regime (reaction temperature $\leq$ 575 K), the surface is metallic and covered with CO at coverages higher than 0.5 ML (judged by the vibrational frequency, see explanation below). In this case, reaction is determined predominantly by CO desorption, evidenced by the fact that CO_2 formation rate increases with increasing reaction temperature; meanwhile, the apparent reaction activation energy based on the Arrhenius plot (not shown here) is approximately the same as desorption activation energy of CO [189]. As the sample temperature reached around 600 K, the second regime appeared.

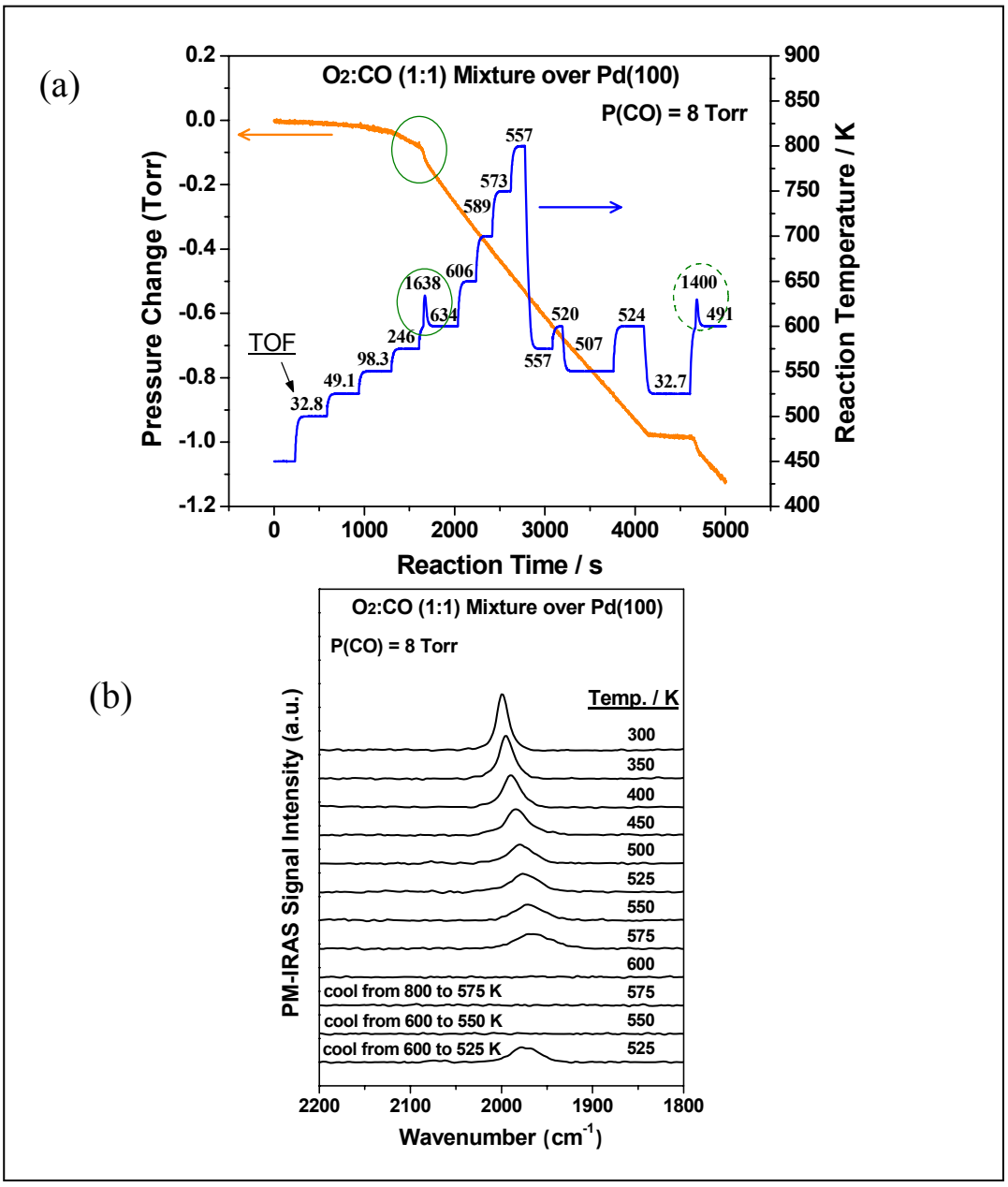

Fig. 50. CO oxidation on Pd(100) in 1:1 O_2/CO mixture at a CO partial pressure of 8 Torr. (a) Pressure change and reaction temperature as a function of reaction time; (b) the corresponding PM-IRA spectra at different temperatures.

In this case, the reaction rate increased greatly as evidenced by a sharp change in the slope of the curve (marked with a solid cycle of the pressure curve). The highest reaction rate (TOF of ~1600) was transiently reached. Because of the exothermic nature of the reaction, the sample temperature transiently increased by ~30 K. As shown later, no CO species was detected on the surface in this regime, indicating the short lifetime of CO and the surface being oxygen rich. As shown later, if CO diffusion is improved, a much higher CO_2 formation rate can be achieved. The third regime (mass transfer limited regime) was reached right after the second regime. In this case, the CO_2 formation rate decreased slowly and exhibited less dependency on reaction temperature. The concurrent infrared spectra showed no detectable CO on surface, which could be attributed to the extremely short lifetime of CO caused by rapid reaction. The reaction rate stayed high even at a temperature as low as 550 K. The reaction slowed at 525 K and CO adsorption reappeared in the infrared spectra (Fig. 50b). Another "jump" in rate was evident when the sample was heated again as indicated by a dashed circle in the pressure curve. Interesting the "jump" in rate does not occur on a CO-absent surface, and is only observed with a CO-adsorbed surface which demonstrates the sufficient diffusion of CO. This phenomenon can be reproduced as long as enough reactants are present in the gas phase.

Another example of high pressure experiments is shown in Fig. 51, in which the reaction was carried out on Pd(100) in 5:1 O_2/CO mixture with a CO partial pressure of 8 Torr. Similar results to the one in 1:1 O_2/CO mixture were obtained. For example, a transient increase in rate ("jump") is observed, except that there were two CO adsorption

features apparent in the spectra, 2142 and 2087 cm^{-1}, respectively. Based on the CO titration experiments on Pd(110), literature results of CO adsorption on O-Pd(100), as well as the discussion on Rh(111), it can be deduced that the 2142 cm^{-1} feature is associated with CO adsorbed on a Pd atom directly coordinated with O atom, whereas the 2087 cm^{-1} feature can be attributed to CO on a Pd atom next to an O atom but not coordinated. Apparently, the surface oxide has formed, giving rise to these two vibrational features. Moreover, the bulk oxide can be ruled out since no CO adsorption was observed on this phase.

From the rate measurement, it also can be seen that after the "jump," the rate is much lower than that in the case of the 1:1 O_2/CO mixture, in which no surface oxide was detected, given the spectra show no high frequency CO adsorption. In addition, at 750 K, an increase in rate was observed at 750 K, a temperature that coincides with the decomposition of surface oxide on Pd(100). Thus it can be concluded that mass transfer limitation of CO leads to the formation of the surface oxide, in turn, deactivating the reaction.

During the high pressure experiments described above, it was rather difficult to monitor the CO species of the second regime, i.e., the transient regime with high reaction rates, mainly because this regime lasted for less than one minute. In order to monitor this process as quickly as possible, continuous infrared scan were performed around the roll over point where each spectrum was acquired by superimposing only 5 scans (total collection time ~5.3 s). This is the shortest time that still allows for collecting a spectrum with reasonable quality.

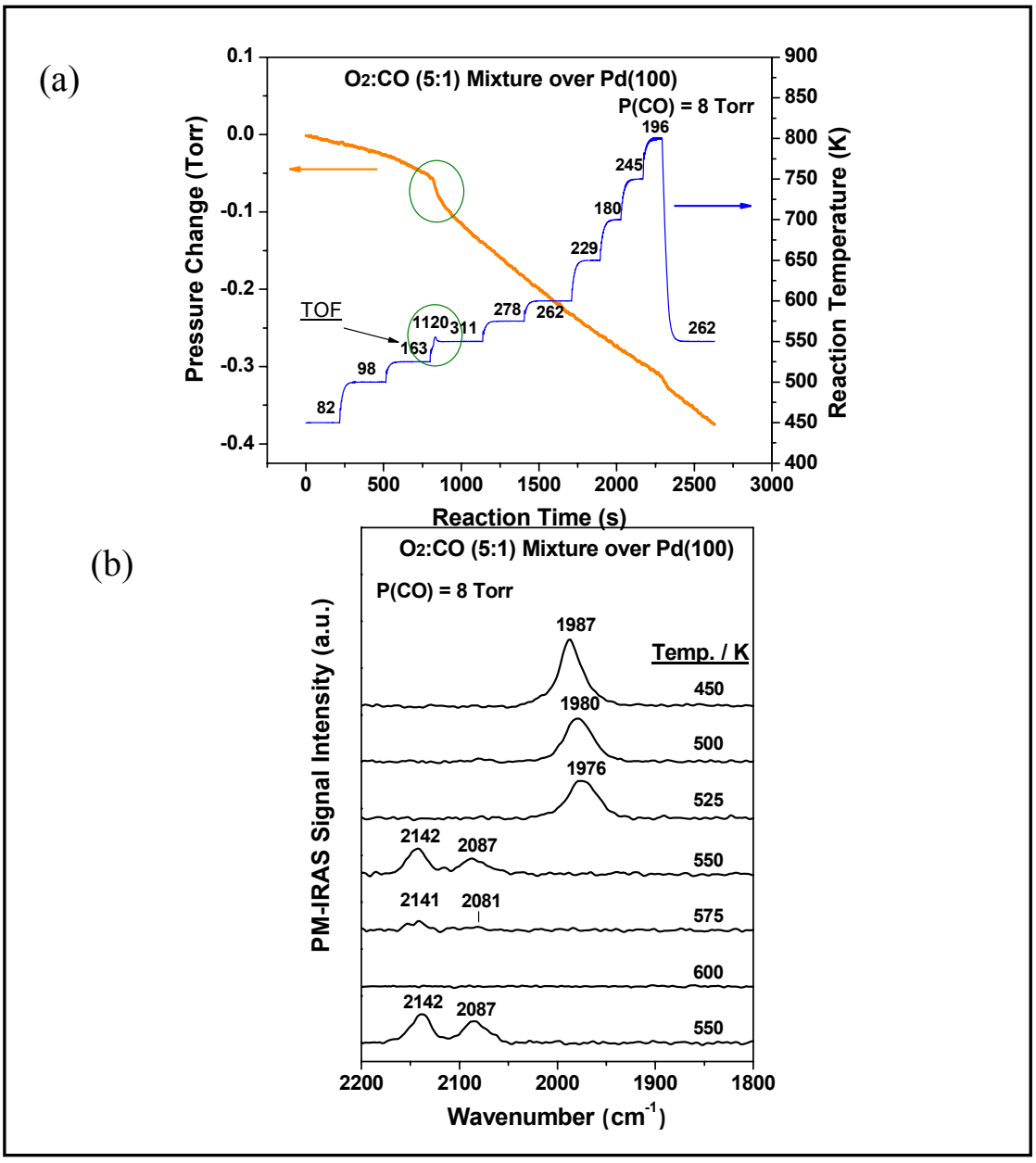

Fig. 51. CO oxidation on Pd(100) in 5:1 O_2/CO mixture at a CO partial pressure of 8 Torr. (a) Pressure change and reaction temperature as a function of reaction time; (b) the corresponding PM-IRA spectra at different temperatures.

As shown in Fig. 52, when the Pd(100) sample was kept in an O_2/CO (10/1) mixture at 500 K (CO initial pressure 2 Torr), in the first ~120 s, the surface was covered by CO with vibrational frequency at ~1980 cm^{-1}. The calculated TOF in this regime is 110 ± 30, after which the reaction rate increases rather abruptly and lasts for ~40 s during which TOF reached 1150 ± 350. Interestingly, there was no detectable CO species on the surface in this regime. Finally, the third regime comes into play, where the surface is covered with CO species at 2140 and 2087 cm^{-1}. Here the TOF was found to be 250 ± 70. This result, together with data acquired at low and high pressures at all O_2/CO ratios examined, demonstrate without any doubt that at the highest reaction rate for any given O_2/CO ratio and pressures, the surface CO coverage is extremely low. It was found that on Pd(110), there is a critical CO coverage of 0.60 ± 0.06 ML of CO adsorbed, above which oxygen dissociative adsorption is blocked. Moreover, the reaction becomes faster for CO coverages below 0.3 ML on Pd(110) [190]. It is possible that the transient rate increase occurs on a surface with a CO coverage less than 0.3 ML.

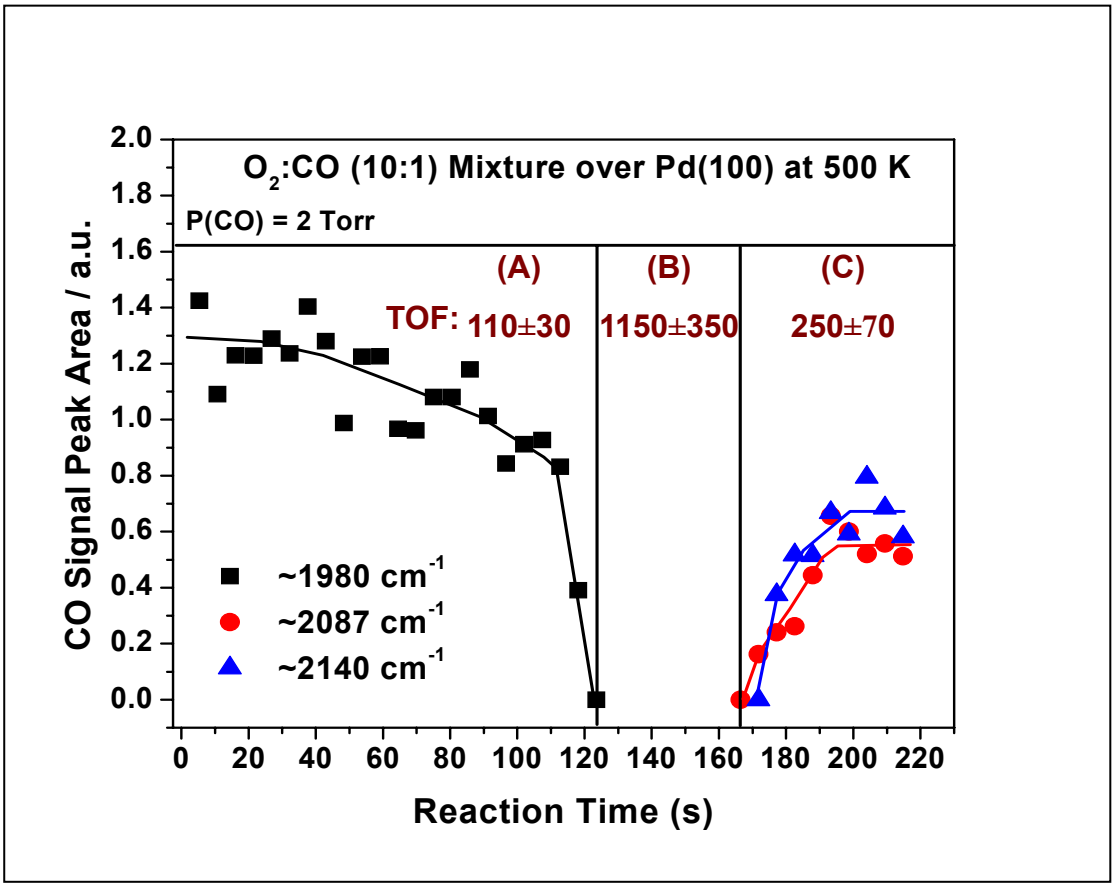

Fig. 52. A correlation between CO adsorption bands and the CO_2 formation rate in a reaction on Pd(100) at 500K in 10:1 O_2:CO mixture with a CO partial pressure of 2 Torr. CO signal peak area as a function of reaction time is plotted in a time-resolved PM-IRAS experiment in the course of the transient increase in reaction rate. Three reaction regimes are distinguished and their reaction rates (TOF) are marked.

Identical experiments were also carried out on Pt(110). Similar results were obtained, that is, the three reaction regimes are found on all Pd surfaces studied. Fig. 53 shows the corresponding PM-IRA spectra acquired in the experiments performed in various gas compositions while maintaining the CO partial pressure at 8.0 Torr. The O_2 pressure was varied from 4.0 to 400 Torr in order to maintain O_2/CO ratios ranging from 1/2 to 50/1. The surface was heated stepwise with 25 K per step. At the beginning of each set of experiments, the CO feature at 2100 cm^{-1} was observed, indicating saturation of CO on the surface [191, 192]. In all cases, spectra acquired prior to the rollover points exhibit only one adsorption band that corresponds to the atop adsorption of CO, which red-shifts monotonously with an increase in temperature. Under such conditions, CO_2 formation is totally dependent on the desorption of CO. With a increase in the oxygen fraction, additional CO is left on the surface prior to the rollover points, as evidenced by the progressive increase of the CO feature in the spectra. In the spectra acquired after the rate rollover, no CO species was detected, similar to that observed on Pd and Rh in low O_2/CO reactants. It has been shown that the adsorption of CO on an oxidized Pt(110) surface will generate a characteristic vibrational band at 2120 cm^{-1} [193]. Therefore, apparently, there is no oxide formation on Pt(110) in the experiments discussed above.

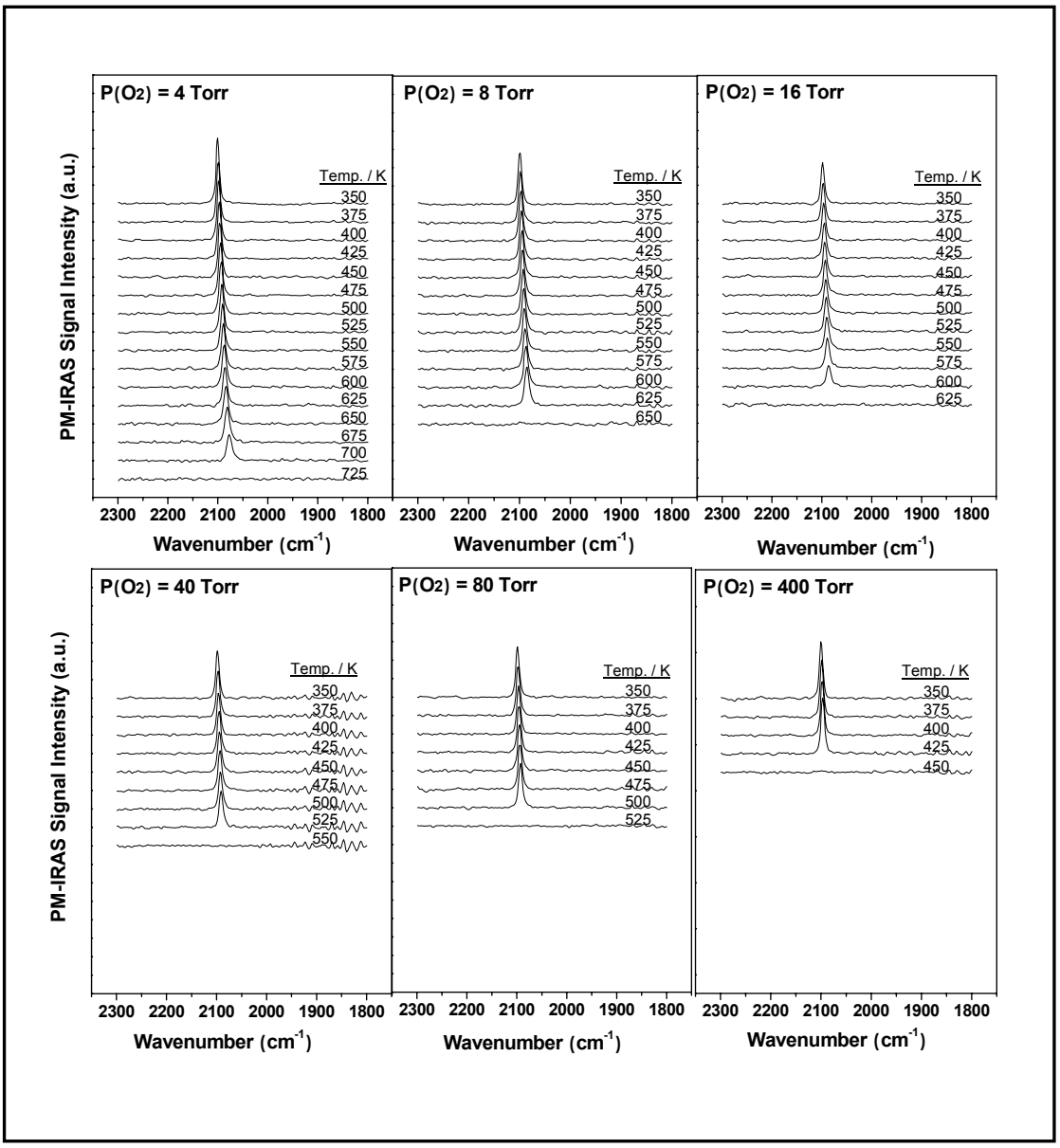

Fig. 53. In situ PM-IRA spectra for a series of CO oxidation reactions at various temperatures on Pt(110) in different gas compositions with a constant CO partial pressure of 8.0 Torr. Oxygen pressure is as indicated.

Demonstration of Mass Transfer Limitation Effect on CO Oxidation Reaction

Since mass transfer limitation effects on CO_2 formation rate were detected at the CO partial pressure above 10^{-3} Torr on all single crystals studied, efforts were made to reduce this effect to improve the diffusion of reactants by placing samples in the middle of a chamber with ~80 cm in width and ~50 cm in height. Fig. 54 displays the CO oxidation reactions on Pd(100) and Rh(111) in an O_2, CO mixture with CO partial pressure of 8.0 Torr and O_2 partial pressure of 4.0 Torr. Total pressure and reaction temperature were recorded as a function of reaction time. As shown in the figure, the reaction rate surged at a certain temperature, ~610 K on Rh(111) and ~640 K on Pd(100), for which reaction occurs vigorously, and the reaction heat thus generated boosts the temperature to 877 K on Rh(111) and 1150 K on Pd(100). The maximum reaction rate, in terms of TOF, reache 3300 on Rh(111) and 8000 on Pd(100), respectively. The experiments for the same gas composition but in a smaller reaction cell were presented in the earlier sections, and the maximum reaction rate obtained, in TOF, are ~1500 for Pd (100) and ~1050 for Rh(111). It is apparent that the position of the sample affects the progression of the reaction rate. However, before the reaction lit off, the reaction rate was close to the value obtained in a smaller reaction cell. As discussed in prior sections, before the jump, within the low rate regime, the surface is poisoned by CO and the reaction rate is dependent on the number of oxygen atom adsorbed. On CO-poisoned surfaces, the adsorption of CO becomes the rate limiting step, and the size of the reactor starts to affect the reaction rate that can be achieved due to reactant diffusion.

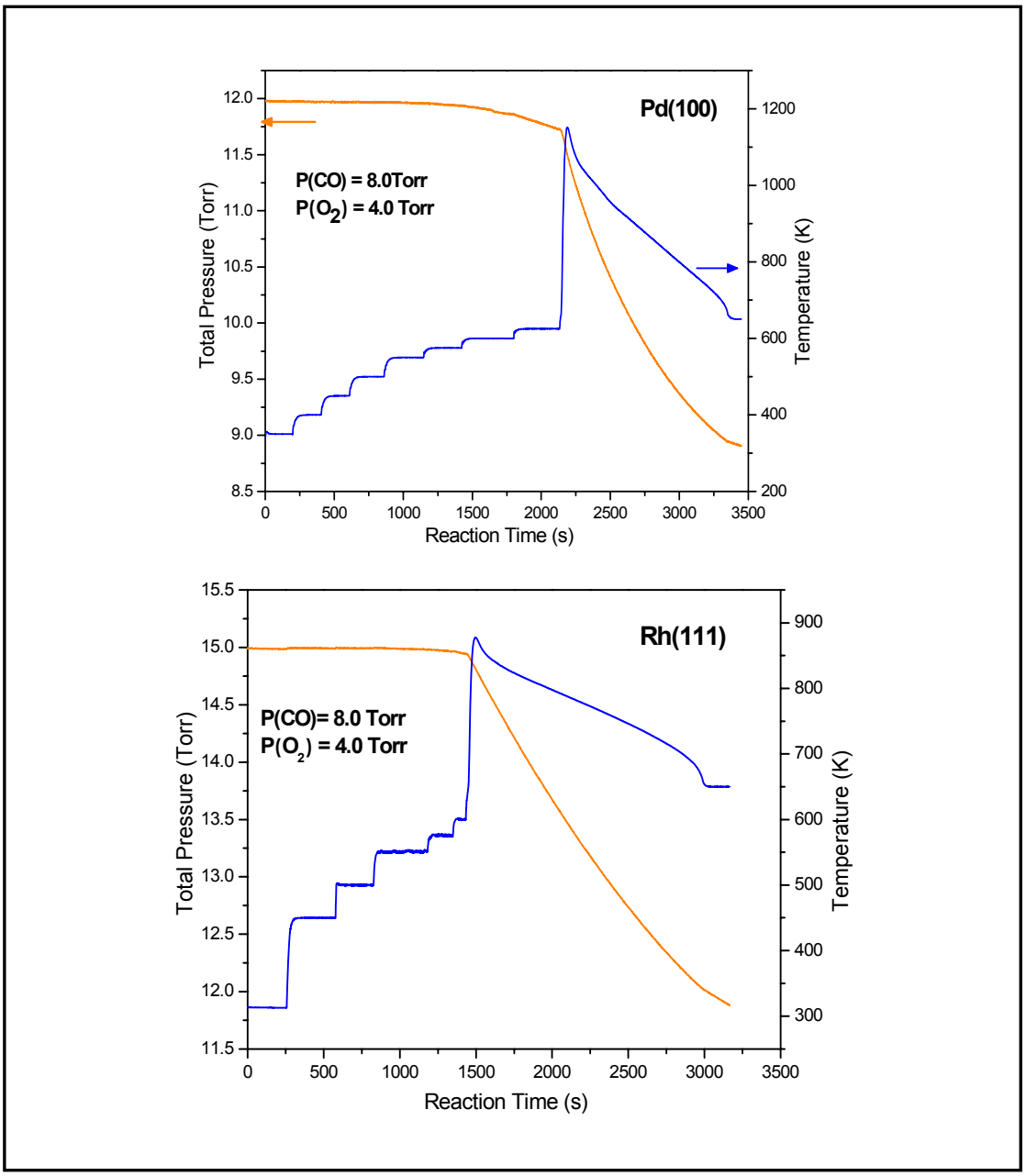

Fig. 54. Total pressure and surface temperature as a function of time for the CO oxidation reactions on Pd(100) (a) and Rh(111) (b) in 8.0 Torr CO and 4.0 Torr O_2 mixture. The single crystals were placed in the middle of a reactor with a volume of 65 L.

An Overlook at CO oxidation on Pd and Pt

Fig. 55 displays Arrhenius plots of CO oxidation on Pd(110), Pd(100), and Pt(110), respectively. The reactions were carried out in various gas compositions as indicated in the figures with a CO partial pressure of 8 Torr. As discussed in the previous sections, three reaction regimes can be distinguished: a low rate regime in which the reaction rate depends on the desorption of CO; a rate rollover regime in which a surge in rate was observed; and a mass transfer limitation regime in which the rate is independent of temperature. On all single crystals studied, it is apparent that with the increase of O_2/CO ratio, the apparent activation energy decreases as indicated by the decrease of the slope on the low rate regime in the Arrhenius plots. The temperature at which the rate surges, decreases with an increase of the oxygen fraction. On Pt(110) surface, after the rollover points, the reaction rate stays constant over a wide temperature range, regardless of the gas composition. On Pd surfaces, however, an evident decline in rate occurs at higher temperatures, a decline more apparent in higher O_2/CO mixtures. Similar phenomena were observed on Rh(111) as well. Another noteworthy fact is that at around 700 K, the reaction rate increases again. It is well-known that Pd surface oxide decomposes around 700 K, which can account for the re-activation of the Pd surface. The concern about the background effect for this rate increase can be ruled out because under the same conditions, the rate declined on the Rh(111) surface.

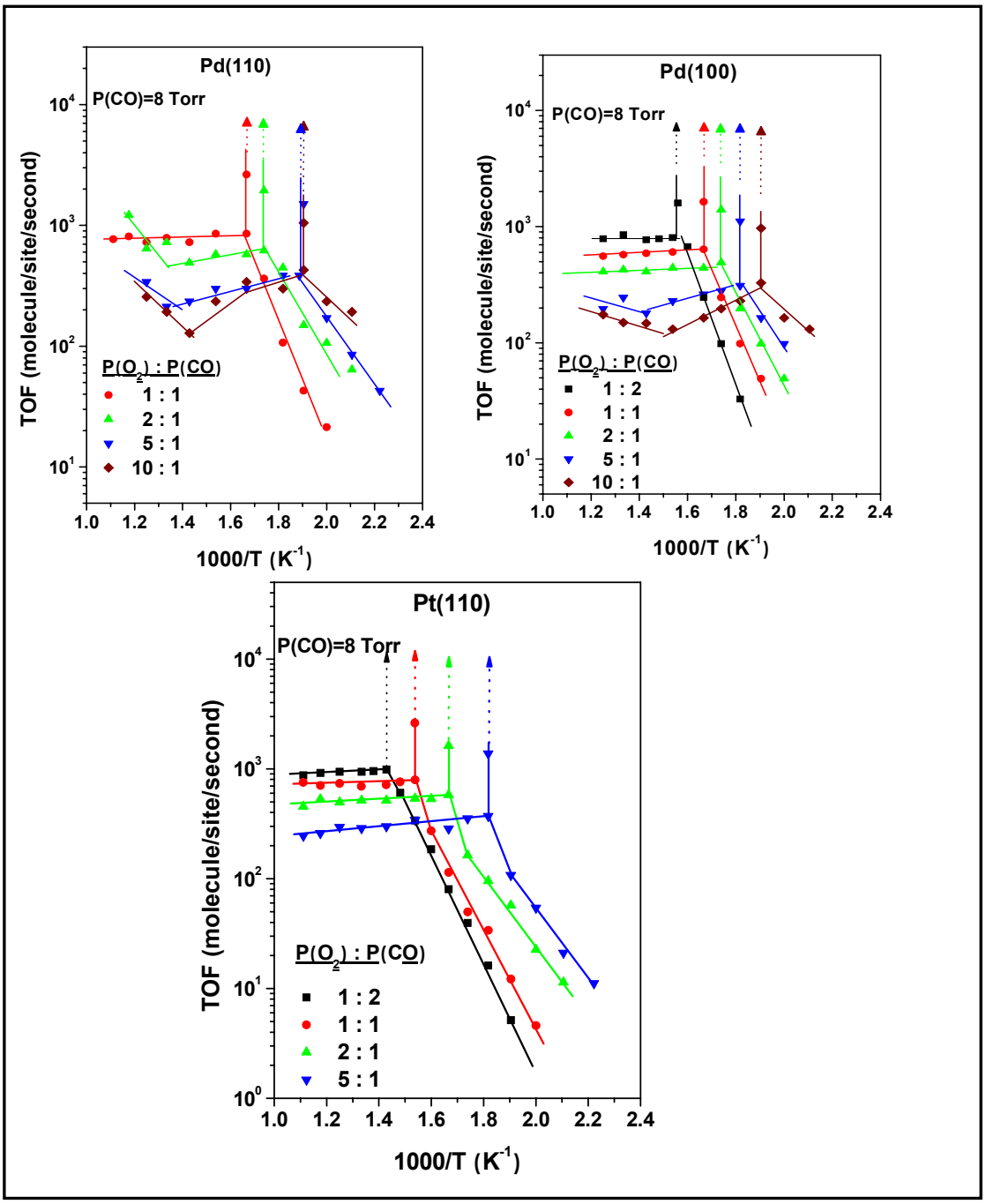

Fig. 55. Arrhenius plots of CO oxidation reactions on Pd(110), Pd(100), and Pt(110) in various gas compositions.

CHAPTER VII

SUMMARY

The primary goals of this work are 1) to employ Polarization Modulation Infrared Reflection and Adsorption Spectroscopy (PM-IRAS) to investigate heterogeneous catalytic reactions under reaction conditions, in particular, under high pressure conditions, and 2) to explore the properties of single-crystal-based catalysts in an attempt to reveal the reaction mechanism under technical reaction conditions.

Chapter I offers a brief introduction of current surface science studies on heterogeneous catalysis, and a short review and background introduction for each of the studies presented in this dissertation. Chapter II describes the major surface science techniques employed in this study and some experimental considerations. Chapter III discusses the NO adsorption and dissociation on Rh(111). Chapter IV explores the electronic properties of different Au catalysts. CO oxidation on Pt-group metals were investigated in Chapter V and VI, with Chapter V focusing on Rh(111) and Chapter VI on Pd single crystals and Pt(110).

In Chapter III, NO adsorption at moderate pressure ($\leq 10^{-6}$ Torr) and temperature (< 275 K), and high pressure (1 Torr) and temperature (≥ 300 K) has been studied. As the sample temperature increases, a transition of NO adsorption from three-fold hollow site to atop site has been observed. It was found that NO dissociation occurs at temperatures well below the temperature previously reported. The presence of NO decomposition products, particularly chemisorbed atomic O species which preferentially adsorb on

hollow sites, gives rise to the NO adsorption on atop sites. The results indicate that the transition of NO adsorption band is not due to the migration of the adsorbed NO but rather to the adsorption of gas-phase NO. The adsorption of NO on an oxygen pretreated Rh(111) surface confirmed the above conclusion. In addition, the exposure of 1 Torr NO at 300K results in only atop adsorption, which again calls into question the surface structures previously proposed at the same adsorption conditions consisting of atop and three-fold hollow sites. This study holds the important implications for understanding the interaction of NO with Rh(111).

In Chapter IV, the preparations of ordered monolayer and bilayer Au films on TiO_x /Mo(112) are introduced. The electronic and chemical properties of these Au films have been investigated using CO as a probe molecule. The Au overlayers are found to be electron-rich and to have significantly different electronic properties compared with bulk Au. The comparison of planar bilayer surfaces with supported Au bilayer nanoparticles indicates that the exceptionally high catalytic activities of the well-ordered Au bilayer structure can be attributed primarily to limited-dimensional effects and to the low degree of coordination of the topmost Au atoms.

Chapter V focuses on CO adsorption and oxidation on Rh(111). PM-IRA spectra of high pressure CO adsorption exhibit the same adsorption features as that of low pressure adsorption, suggesting that high pressure CO does not form any new adsorption layer and/or induce any reconstruction of Rh(111) substrate. In high pressure CO oxidation experiments, three reaction regimes have been found: a CO-inhibited regime, a CO-uninhibited regime, and a mass-transfer-limited regime. The first two reaction

regimes are also found in low pressure reactions. The reactions in these two regimes well represent the elementary steps in a Langmuir-Hinshelwood mechanism. However, due to mass transfer limitation effects, the CO-uninhibited regime is very limited in high pressure reactions, resulting in the appearance of a sharp peak in the plot of reaction rate as a function of reaction time. It is also found that O_2/CO ratio plays an important role in the transient increase in rate ("jump"). Reactions in higher O_2/CO ratio mixtures result in an earlier "jump" at lower temperature, and the surface deactivates faster following the "jump." The concurrent PM-IRAS experiments have demonstrated the influence of oxygen species on the CO oxidation reaction. Three CO adsorption features associated with three oxygen species have been found. The titration experiments of oxygen-covered Rh(111) surfaces show that the oxygen species associated with the CO vibrational feature at 2084 cm^{-1} is likely subsurface oxygen whose surface coverage is around 0.8 ML.

The first infrared spectroscopic study of high pressure CO adsorption on Pd(110) is reported in Chapter VI, in which the adsorption features identical to those of low pressure adsorptions have been observed. The continuum of CO adsorption on Pd(110) from low pressure to high pressure demonstrates that there is no pressure gap in CO oxidation on Pd single crystals, given the literature results for other Pd single crystals. The oxidation on Pd(110) has also been investigated by AES and PM-IRAS using CO as a probe molecule. No reaction occurs on Pd bulk oxide. CO adsorption on Pd surface 2D oxide gives rise to two vibrational features at 2140 and 2108 cm^{-1}. On the oxygen-covered Pd(110) surface, a CO vibrational feature at 2110 cm^{-1} is observed. The

experimental results clearly show that the activity of O-Pd(110) surfaces are: chemisorbed-O > 2D surface oxide > bulk oxide.

CO oxidation studies on Pd single crystals and Pt(110) are also presented in Chapter VI. Three reaction regimes as found for Rh(111) are also evident. Again, it has been observed that before reaching mass-transfer-limited regime, reactions on Pd single crystals and Pt(110) follow the L-H mechanism. In contrast to Rh(111), within the mass-transfer-limited regime, deactivated Pd surfaces become active due to decomposition of the surface oxide. For Pt(110), no oxidation of the surface has been observed, resulting in a constant rate in the mass-transfer-limited regime. The surface structures of Pd(110), Pd(111), and Pd(100) determine the accessibility of oxygen onto the surface, giving rise to varying amount of oxidation of the surface. The oxidation of the surface, in turn, influences the activity of the surface. Among three Pd single crystals, Pd(110) has the least density of atoms, i.e., the most "open" surface. On one hand, because oxygen reacts more facilely with Pd(110), the CO oxidation reaction initiates earlier. On the other hand, because Pd(110) oxidizes more easily, the surface deactivates faster, especially within the mass-transfer-limited regime.

The investigations of CO oxidation on Rh, Pd and Pt presented in this dissertation cover the pressure of CO from 10^{-8} to 8 Torr, enabling a comprehensive understanding of this reaction. The results have clearly demonstrated the continuum of CO oxidation reaction mechanism from low pressure to high pressure, i.e., CO oxidation reactions on Rh, Pd, and Pd follow the Langmuir-Hinshelwood mechanism rather than other proposed mechanisms.

REFERENCES

[1] G. Ertl, Angew. Chem., Int. Ed. Engl. 29 (1990) 1219.

[2] G. Ertl, J. Mol. Catal. A 182-183 (2002) 5.

[3] P.J. Berlowitz, C.H.F. Peden, D.W. Goodman, J. Phys. Chem. 92 (1988) 5213.

[4] K. Honkala, A. Hellman, I.N. Remediakis, A. Logadottir, A. Carlsson, S. Dahl, C.H. Christensen, J.K. Norskov, Science 307 (2005) 555.

[5] P. Stoltze, J.K. Norskov, Phys. Rev. Lett. 55 (1985) 2502.

[6] C.H.F. Peden, D.W. Goodman, J. Phys. Chem. 90 (1986) 1360.

[7] P.L. Hansen, J.B. Wagner, S. Helveg, J.R. Rostrup-Nielsen, B.S. Clausen, H. Topsoe, Science 295 (2002) 2053.

[8] T.W. Hansen, J.B. Wagner, P.L. Hansen, S. Dahl, H. Topsoe, C.J.H. Jacobsen, Science 294 (2001) 1508.

[9] S. Helveg, C. Lopez-Cartes, J. Sehested, P.L. Hansen, B.S. Clausen, J.R. Rostrup-Nielsen, F. Abild-Pedersen, J.K. Norskov, Nature 427 (2004) 426.

[10] P. Bernard, K. Peters, J. Alvarez, S. Ferrer, Rev. Sci. Instrum. 70 (1999) 1478.

[11] D.F. Ogletree, H. Bluhm, G. Lebedev, C.S. Fadley, Z. Hussain, M. Salmeron, Rev. Sci. Instrum. 73 (2002) 3872.

[12] G. Somorjai, X. Su, K. McCrea, K. Rider, Top. Catal. 8 (1999) 23.

[13] E. Laegsgaard, L. Osterlund, P. Thostrup, P.B. Rasmussen, I. Stensgaard, F. Besenbacher, Rev. Sci. Instrum. 72 (2001) 3537.

[14] X. Su, P.S. Cremer, Y.R. Shen, G.A. Somorjai, J. Am. Chem. Soc. 119 (1997) 3994.

[15] R. Kissel-Osterrieder, F. Behrendt, J. Warnatz, U. Metka, H.R. Volpp, J. Wolfrum, Proc. Combust. Inst. 28 (2000) 1341.

[16] G. Rupprechter, T. Dellwig, H. Unterhalt, H.J. Freund, J. Phys. Chem. B 105 (2001) 3797.

[17] G. Rupprechter, Adv. Catal. 51 (2007) 133.

[18] G.A. Beitel, C.P.M. de Groot, H. Oosterbeek, J.H. Wilson, J. Phys. Chem. B 101 (1997) 4035.

[19] E. Ozensoy, D.C. Meier, D.W. Goodman, J. Phys. Chem. 106 (2002) 9367.

[20] T. Engel, G. Ertl, Adv. Catal. 28 (1979) 1.

[21] I. Langmuir, Trans. Faraday Soc. 17 (1922) 621.

[22] C.T. Campbell, G. Ertl, H. Kuipers, J. Segner, J. Chem. Phys. 73 (1980) 5862.

[23] H. Conrad, G. Ertl, J. Kuppers, E.E. Latta, Surf. Sci. 65 (1977) 245.

[24] M. Wilf, P.T. Dawson, Surf. Sci. 65 (1977) 399.

[25] G. Ertl, P. Rau, Surf. Sci. 15 (1969) 443.

[26] T. Engel, G. Ertl, J. Chem. Phys. 69 (1978) 1267.

[27] P. Mars, D.W.v. Krevelen, Chem. Eng. Sci. (Special Suppl.) 3 (1954) 41.

[28] H. Conrad, G. Ertl, J. Kuppers, Surf. Sci. 76 (1978) 323.

[29] S.H. Kim, J. Mendez, J. Wintterlin, G. Ertl, Phys. Rev. B: Condens. Matter 72 (2005) 155414.

[30] M. Todorova, K. Reuter, M. Scheffler, J. Phys. Chem. B 108 (2004) 14477.

[31] X.P. Xu, D.W. Goodman, J. Phys. Chem. 97 (1993) 7711.

[32] E.M. Stuve, R.J. Madix, C.R. Brundle, Surf. Sci. 146 (1984) 155.

[33] H. Unterhalt, G. Rupprechter, H.J. Freund, J. Phys. Chem. B 106 (2002) 356.

[34] W.K. Kuhn, J. Szanyi, D.W. Goodman, Surf. Sci. 274 (1992) L611.

[35] G. Rupprechter, H. Unterhalt, M. Morkel, P. Galletto, L. Hu, H.-J. Freund, Surf. Sci. 502-503 (2002) 109.

[36] R.T. Vang, E. Laegsgaard, F. Besenbacher, Phys. Chem. Chem. Phys. 9 (2007) 3460.

[37] P.S. Cremer, X. Su, G.A. Somorjai, Y.R. Shen, J. Mol. Catal. A: Chem. 131 (1998) 225.

[38] R. Imbihl, J.E. Demuth, Surf. Sci. 173 (1986) 395.

[39] G. Zheng, E.I. Altman, Surf. Sci. 462 (2000) 151.

[40] F.P. Leisenberger, G. Koller, M. Sock, S. Surnev, M.G. Ramsey, F.P. Netzer, B. Klotzer, K. Hayek, Surf. Sci. 445 (2000) 380.

[41] H. Gabasch, W. Unterberger, K. Hayek, B. Klotzer, G. Kresse, C. Klein, M. Schmid, P. Varga, Surf. Sci. 600 (2006) 205.

[42] E. Lundgren, G. Kresse, C. Klein, M. Borg, J.N. Andersen, M. De Santis, Y. Gauthier, C. Konvicka, M. Schmid, P. Varga, Phys. Rev. Lett. 88 (2002) 4.

[43] J.Y. Han, D.Y. Zemlyanov, F.H. Ribeiro, Surf. Sci. 600 (2006) 2730.

[44] T. Lele, J. Lauterbach, Chaos 12 (2002) 164.

[45] H.H. Rotermund, G. Haas, R.U. Franz, R.M. Tromp, G. Ertl, Appl. Phys. A 61 (1995) 569.

[46] H. Over, Y.D. Kim, A.P. Seitsonen, S. Wendt, E. Lundgren, M. Schmid, P. Varga, A. Morgante, G. Ertl, Science 287 (2000) 1474.

[47] B. Hendriksen, S. Bobaru, J. Frenken, Top. Catal. 36 (2005) 43.

[48] M.A. Vannice, Catal. Today 123 (2007) 18.

[49] M. Haruta, Catal. Today 36 (1997) 153.

[50] M. Valden, X. Lai, D.W. Goodman, Science 281 (1998) 1647.

[51] D.W. Goodman, J. Catal. 216 (2003) 213.

[52] M.S. Chen, D.W. Goodman, Science 306 (2004) 252.

[53] T.V. Choudhary, C. Sivadinarayana, C.C. Chusuei, A.K. Datye, J.P. Fackler, D.W. Goodman, J. Catal. 207 (2002) 247.

[54] E. Gerhard, K. Jurgen, Low Energy Electrons & Surface Chemistry. Wiley-VCH, Weinheim, Germany, 1985.

[55] Y.J. Chabal, Surf. Sci. Rep. 8 (1988) 211.

[56] F.M. Hoffmann, Surf. Sci. Rep. 3 (1983) 107.

[57] G. Blyholder, J. Phys. Chem. 68 (1964) 2772.

[58] W.G. Golden, D.S. Dunn, J. Overend, J. Phys. Chem. 82 (1978) 843.

[59] G.A. Beitel, A. Laskov, H. Oosterbeek, E.W. Kuipers, J. Phys. Chem. 100 (1996) 12494.

[60] B.J. Barner, M.J. Green, E.I. Saez, R.M. Corn, Anal. Chem. 63 (1991) 55.

[61] L.A. Avalos, V. Bustos, R. Unac, F. Zaera, G. Zgrablich, J. Mol. Catal. A 228 (2005) 89.

[62] J.F. Paul, J. Perez-Ramirez, F. Ample, J.M. Ricart, J. Phys. Chem. B 108 (2004) 17921.

[63] C.H.F. Peden, D.W. Goodman, D.S. Blair, P.J. Berlowitz, G.B. Fisher, S.H. Oh, J. Phys. Chem. 92 (1988) 1563.

[64] F. Zaera, C.S. Gopinath, Chem. Phys. Lett. 332 (2000) 209.

[65] R.J. Baird, R.C. Ku, P. Wynblatt, Surf. Sci. 97 (1980) 346.

[66] H.J. Borg, J.F.C.-J.M. Reijerse, R.A. van Santen, J.W. Niemantsverdriet, J. Chem. Phys. 101 (1994) 10052.

[67] L.H. Dubois, P.K. Hansma, G.A. Somorjai, J. Catal. 65 (1980) 318.

[68] M.J.P. Hopstaken, J.W. Niemantsverdriet, J. Phys. Chem. B 104 (2000) 3058.

[69] N.M.H. Janssen, A.R. Cholach, M. Ikai, K. Tanaka, B.E. Nieuwenhuys, Surf. Sci. 382 (1997) 201.

[70] Y.J. Kim, S. Thevuthasan, G.S. Herman, C.H.F. Peden, S.A. Chambers, D.N. Belton, H. Permana, Surf. Sci. 359 (1996) 269.

[71] G.A. Papapolymerou, L.D. Schmidt, Langmuir 1 (1985) 488.

[72] V. Schmatloch, I. Jirka, N. Kruse, J. Chem. Phys. 100 (1994) 8471.

[73] H. Xu, K.Y.S. Ng, Surf. Sci. 365 (1996) 779.

[74] L.A. DeLouise, N. Winograd, Surf. Sci. 159 (1985) 199.

[75] D. Loffreda, D. Simon, P. Sautet, J. Catal. 213 (2003) 211.

[76] R.M. Wolf, J.W. Bakker, B.E. Nieuwenhuys, Surf. Sci. 246 (1991) 135.

[77] D.G. Castner, B.A. Sexton, G.A. Somorjai, Surf. Sci. 71 (1978) 519.

[78] C.T. Kao, G.S. Blackman, M.A. Van Hove, G.A. Somorjai, C.M. Chan, Surf. Sci. 224 (1989) 77.

[79] I. Zasada, M.A. Van Hove, G.A. Somorjai, Surf. Sci. 418 (1998) L89.

[80] T.W. Root, G.B. Fisher, L.D. Schmidt, J. Chem. Phys. 85 (1986) 4679.

[81] T.W. Root, G.B. Fisher, L.D. Schmidt, J. Chem. Phys. 85 (1986) 4687.

[82] T.W. Root, L.D. Schmidt, G.B. Fisher, Surf. Sci. 134 (1983) 30.

[83] K.B. Rider, K.S. Hwang, M. Salmeron, G.A. Somorjai, Phys. Rev. Lett. 86 (2001) 4330.

[84] K.B. Rider, K.S. Hwang, M. Salmeron, G.A. Somorjai, J. Am. Chem. Soc. 124 (2002) 5588.

[85] V.P. Zhdanov, B. Kasemo, Surf. Sci. Rep. 29 (1997) 31.

[86] C.G.M. Hermse, F. Frechard, A.P. van Bavel, J.J. Lukkien, J.W. Niemantsverdriet, R.A. van Santen, A.P.J. Jansen, J. Chem. Phys. 118 (2003) 7081.

[87] O.R. Inderwildi, D. Lebiedz, O. Deutschmann, J. Warnatz, J. Chem. Phys. 122 (2005) 154702.

[88] D. Loffreda, D. Simon, P. Sautet, Chem. Phys. Lett. 291 (1998) 15.

[89] M. Mavrikakis, J. Rempel, J. Greeley, L.B. Hansen, J.K. Norskov, J. Chem. Phys. 117 (2002) 6737.

[90] R.M. Ferrizz, T. Egami, G.S. Wong, J.M. Vohs, Surf. Sci. 476 (2001) 9.

[91] D.R. Mullins, S.H. Overbury, Surf. Sci. 511 (2002) L293.

[92] S.H. Overbury, D.R. Mullins, L. Kundakovic, Surf. Sci. 470 (2001) 243.

[93] P. Granger, H. Praliaud, J. Billy, L. Leclercq, G. Leclercq, Surf. Interface. Anal. 34 (2002) 92.

[94] T. Matsushima, I. Rzeznicka, Y. Ma, Chem. Rec. 5 (2005) 81.

[95] M.C. Daniel, D. Astruc, Chem. Rev. 104 (2004) 293.

[96] M. Haruta, M. Dat, Appl. Catal., A 222 (2001) 427.

[97] M. Haruta, N. Yamada, T. Kobayashi, S. Iijima, J. Catal. 115 (1989) 301.

[98] G.J. Hutchings, Catal. Today 100 (2005) 55.

[99] D.R. Rolison, Science 299 (2003) 1698.

[100] C.T. Campbell, Science 306 (2004) 234.

[101] D.W. Goodman, Catal. Lett. 99 (2005) 1.

[102] S. Lee, C. Fan, T. Wu, S.L. Anderson, Surf. Sci. 578 (2005) 5.

[103] Z.-P. Liu, S.J. Jenkins, D.A. King, Phys. Rev. Lett. 94 (2005) 196102.

[104] N. Lopez, T.V.W. Janssens, B.S. Clausen, Y. Xu, M. Mavrikakis, T. Bligaard, J.K. Norskov, J. Catal. 223 (2004) 232.

[105] F. Shi, Q. Zhang, Y. Ma, Y. He, Y. Deng, J. Am. Chem. Soc. 127 (2005) 4182.

[106] C.C. Chusuei, X. Lai, K. Luo, D.W. Goodman, Top. Catal. 14 (2000) 71.

[107] V. Bondzie, S. Parker, C. Campbell, Catal. Lett. 63 (1999) 143.

[108] D.C. Meier, D.W. Goodman, J. Am. Chem. Soc. 126 (2004) 1892.

[109] M.S. Chen, A.K. Santra, D.W. Goodman, Phys. Rev. B: Condens. Matter 69 (2004) 155404.

[110] M.S. Chen, W.T. Wallace, D. Kumar, Z. Yan, K.K. Gath, Y. Cai, Y. Kuroda, D.W. Goodman, Surf. Sci. 581 (2005) 115.

[111] J.A. Rodriguez, G. Liu, T. Jirsak, J. Hrbek, Z. Chang, J. Dvorak, A. Maiti, J. Am. Chem. Soc. 124 (2002) 5242.

[112] N. Lopez, J.K. Norskov, T.V.W. Janssens, A. Carlsson, A. Puig-Molina, B.S. Clausen, J.D. Grunwaldt, J. Catal. 225 (2004) 86.

[113] G. Mills, M.S. Gordon, H. Metiu, J. Chem. Phys. 118 (2003) 4198.

[114] K. Okazaki, Y. Morikawa, S. Tanaka, K. Tanaka, M. Kohyama, Phys. Rev. B: Condens. Matter 69 (2004) 235404.

[115] A. Sanchez, S. Abbet, U. Heiz, W.D. Schneider, H. Hakkinen, R.N. Barnett, U. Landman, J. Phys. Chem. A 103 (1999) 9573.

[116] E. Wahlstrom, N. Lopez, R. Schaub, P. Thostrup, A. Ronnau, C. Africh, E. Laegsgaard, J.K. Norskov, F. Besenbacher, Phys. Rev. Lett. 90 (2003) 026101.

[117] F. Ample, D. Curulla, F. Fuster, A. Clotet, J.M. Ricart, Surf. Sci. 497 (2002) 139.

[118] V.Y.B. D. Guillemot, V. B. Kazansky, M. Polisset-Thfoin and J. Fraissard, J. Chem. Soc., Faraday Trans. 93 (1997) 3587.

[119] B. Yoon, H. Hakkinen, U. Landman, A.S. Worz, J.-M. Antonietti, S. Abbet, K. Judai, U. Heiz, Science 307 (2005) 403.

[120] H. Hakkinen, S. Abbet, A. Sanchez, U. Heiz, U. Landman, Angew. Chem., Int. Ed. Eng. 42 (2003) 1297.

[121] P. Dumas, R.G. Tobin, P.L. Richards, Surf. Sci. 171 (1986) 579.

[122] J. France, P. Hollins, J. Electron. Spectrosc. Relat. Phenom. 64-65 (1993) 251.

[123] C. Lemire, R. Meyer, S.K. Shaikhutdinov, H.J. Freund, Surf. Sci. 552 (2004) 27.

[124] R.A. Van Santen, M. Neurock, Catalysis Reviews 37 (1995) 557

[125] J. Rodriguez, M. Kuhn, Surf. Sci. 330 (1995) L657.

[126] J.A. Rodriguez, D.W. Goodman, Science 257 (1992) 897.

[127] J.A. Rodriguez, R.A. Campbell, D.W. Goodman, J. Phys. Chem. 95 (1991) 5716.

[128] B. Yoon, H. Hakkinen, U. Landman, J. Phys. Chem. A 107 (2003) 4066.

[129] M.S. Chen, Y. Cai, Z. Yan, D.W. Goodman, J. Am. Chem. Soc. 128 (2006) 6341.

[130] L.H. Dubois, G.A. Somorjai, Surf. Sci. 91 (1980) 514.

[131] R. Linke, D. Curulla, M.J.P. Hopstaken, J.W. Niemantsverdriet, J. Chem. Phys. 115 (2001) 8209.

[132] A.J. Jaworowski, A. Beutler, F. Strisland, R. Nyholm, B. Setlik, D. Heskett, J.N. Andersen, Surf. Sci. 431 (1999) 33.

[133] A. Beutler, E. Lundgren, R. Nyholm, J.N. Andersen, B.J. Setlik, D. Heskett, Surf. Sci. 396 (1998) 117.

[134] I. Nakamura, Y. Kobayashi, H. Hamada, T. Fujitani, Surf. Sci. 600 (2006) 3235.

[135] G. Krenn, I. Bako, R. Schennach, J. Chem. Phys. 124 (2006) 144703.

[136] J.E. Crowell, G.A. Somorjai, Appl. Surf. Sci. 19 (1984) 73.

[137] S. Schwegmann, H. Over, V. De Renzi, G. Ertl, Surf. Sci. 375 (1997) 91.

[138] J. Xu, D.R. Mullins, S.H. Overbury, J. Catal. 243 (2006) 158.

[139] D.W. Goodman, C.H.F. Peden, J. Phys. Chem. 90 (1986) 4839.

[140] S.B. Schwartz, L.D. Schmidt, G.B. Fisher, J. Phys. Chem. 90 (1986) 6194.

[141] P.A. Thiel, J.T. Yates, W.H. Weinberg, Surf. Sci. 82 (1979) 22.

[142] K.D. Gibson, M. Viste, E.C. Sanchez, S.J. Sibener, J. Chem. Phys. 110 (1999) 2757.

[143] L. Kohler, G. Kresse, M. Schmid, E. Lundgren, J. Gustafson, A. Mikkelsen, M. Borg, J. Yuhara, J.N. Andersen, M. Marsman, P. Varga, Phys. Rev. Lett. 93 (2004) 266103.

[144] J. Wider, T. Greber, E. Wetli, T.J. Kreutz, P. Schwaller, J. Osterwalder, Surf. Sci. 417 (1998) 301.

[145] J. Gustafson, A. Mikkelsen, M. Borg, E. Lundgren, L. Kohler, G. Kresse, M. Schmid, P. Varga, J. Yuhara, X. Torrelles, Q. C., J.N. Andersen, Phys. Rev. Lett. 92 (2004) 126102.

[146] H. Gabasch, A. Knop-Gericke, R. Schlogl, M. Borasio, C. Weilach, G. Rupprechter, S. Penner, B. Jenewein, K. Hayek, B. Klotzer, Phys. Chem. Chem. Phys. 9 (2007) 533.

[147] E. Lundgren, J. Gustafson, A. Resta, J. Weissenrieder, A. Mikkelsen, J.N. Andersen, L. Kohler, G. Kresse, J. Klikovits, A. Biederman, M. Schmid, P. Varga, J. Electron. Spectrosc. Relat. Phenom. 144-147 (2005) 367.

[148] C.H.F. Peden, D.W. Goodman, D.S. Blair, P.J. Berlowitz, G.B. Fisher, S.H. Oh, J. Phys. Chem. 92 (1988) 1563.

[149] K.W. Kolasinski, Surface Science:foundations of catalysis and nanoscience. John Wiley & Sons Ltd., 2002.

[150] H. Conrad, G. Ertl, J. Koch, E.E. Latta, Surf. Sci. 43 (1974) 462.

[151] A. Ortega, F.M. Huffman, A.M. Bradshaw, Surf. Sci. 119 (1982) 79.

[152] E. Ozensoy, D.W. Goodman, Phys. Chem. Chem. Phys. 6 (2004) 3765.

[153] J. Szanyi, W.K. Kuhn, D.W. Goodman, J. Vac. Sci. Technol. A-Vac. Surf. Films 11 (1993) 1969.

[154] X.P. Xu, P.J. Chen, D.W. Goodman, J. Phys. Chem. 98 (1994) 9242.

[155] R.J. Behm, K. Christmann, G. Ertl, M.A. Van Hove, P.A. Thiel, W.H. Weinberg, Surf. Sci. 88 (1979) L59.

[156] R.J. Behm, K. Christmann, G. Ertl, M.A. Van Hove, J. Chem. Phys. 73 (1980) 2984.

[157] G. Zheng, E.I. Altman, Surf. Sci. 504 (2002) 253.

[158] G. Ertl, J. Koch, Z. Phys. Chem. 69 (1970) 323.

[159] T.W. Orent, S.D. Bader, Surf. Sci. 115 (1982) 323.

[160] S.L. Chang, P.A. Thiel, J. Chem. Phys. 88 (1988) 2071.

[161] M. Todorova, E. Lundgren, V. Blum, A. Mikkelsen, S. Gray, J. Gustafson, M. Borg, J. Rogal, K. Reuter, J.N. Andersen, M. Scheffler, Surf. Sci. 541 (2003) 101.

[162] J. Rogal, K. Reuter, M. Scheffler, Phys. Rev. B: Condens. Matter 75 (2007) 205433.

[163] E. Lundgren, J. Gustafson, A. Mikkelsen, J.N. Andersen, A. Stierle, H. Dosch, M. Todorova, J. Rogal, K. Reuter, M. Scheffler, Phys. Rev. Lett. 92 (2004) 046101.

[164] F. Gao, M. Lundwall, D.W. Goodman, J. Phys. Chem. C 112 (2008) 6057.

[165] G. Zheng, E.I. Altman, J. Phys. Chem. B 106 (2002) 1048.

[166] M.K. Rose, T. Mitsui, J. Dunphy, A. Borg, D.F. Ogletree, M. Salmeron, P. Sautet, Surf. Sci. 512 (2002) 48.

[167] A.M. Bradshaw, F.M. Hoffmann, Surf. Sci. 72 (1978) 513.

[168] H.H. Kan, R.B. Shumbera, J.F. Weaver, Surf. Sci. 602 (2008) 1337.

[169] J. Mendez, S.H. Kim, J. Cerda, J. Wintterlin, G. Ertl, Phys. Rev. B: Condens. Matter 71 (2005) 13.

[170] A.P. Seitsonen, Y.D. Kim, S. Schwegmann, H. Over, Surf. Sci. 468 (2000) 176.

[171] I. Nakai, H. Kondoh, T. Shimada, A. Resta, J.N. Andersen, T. Ohta, J. Chem.

Phys. 124 (2006) 224712.

[172] P. Salo, K. Honkala, M. Alatalo, K. Laasonen, Surf. Sci. 516 (2002) 247.

[173] C.J. Zhang, P. Hu, J. Am. Chem. Soc. 123 (2001) 1166.

[174] E.E. Tornau, V. Petrauskas, G. Zvejnieks, Catal. Today 116 (2006) 62.

[175] I.Z. Jones, R.A. Bennett, M. Bowker, Surf. Sci. 402-404 (1998) 595.

[176] A. Gaussman, N. Kruse, Surf. Sci. 266 (1992) 46.

[177] A. Gaussmann, N. Kruse, Surf. Sci. 279 (1992) 319.

[178] P. Hu, L.M. de la Garza, R. Raval, D.A. King, Surf. Sci. 249 (1991) 1.

[179] R. Raval, G. Blyholder, S. Haq, D.A. King, J. Phys.: Condens. Matter 1 (1989) SB165.

[180] R. Raval, S. Haq, G. Blyholder, D.A. King, J. Electron. Spectrosc. Relat. Phenom. 54-55 (1990) 629.

[181] R. Raval, S. Haq, M.A. Harrison, G. Blyholder, D.A. King, Chem. Phys. Lett. 167 (1990) 391.

[182] R. Raval, M.A. Harrison, D.A. King, Surf. Sci. 211-212 (1989) 61.

[183] K. Fukui, H. Miyauchi, Y. Iwasawa, J. Phys. Chem. 100 (1996) 18795.

[184] M.A. Chesters, G.S. McDougall, M.E. Pemble, N. Sheppard, Surf. Sci. 164 (1985) 425.

[185] J. Han, D.Y. Zemlyanov, F.H. Ribeiro, Surf. Sci. 600 (2006) 2752.

[186] K.I. Choi, M.A. Vannice, J. Catal. 131 (1991) 1.

[187] S. Ladas, R. Imbihl, G. Ertl, Surf. Sci. 280 (1993) 14.

[188] J. Han, G. Zhu, D.Y. Zemlyanov, F.H. Ribeiro, J. Catal. 225 (2004) 7.

[189] D.W. Goodman, Chem. Rev. 95 (1995) 523.

[190] I.Z. Jones, R.A. Bennett, M. Bowker, Surf. Sci. 439 (1999) 235.

[191] S.C. J. H. Miners, V. Efstathiou, M. Kim, and D. P. Woodruff, J. Chem. Phys. 117 (2002) 12.

[192] R.K. Sharma, W.A. Brown, D.A. King, Surf. Sci. 414 (1998) 68.

[193] T.H. Lindstrom, T.T. Tsotsis, Surf. Sci. 150 (1985) 487.

VITA

Name:	Yun Cai
Address:	Department of Chemistry, Texas A&M University PO Box 30012, College Station, TX 77843
Email Address:	cyunfeier@yahoo.com
Education:	B.S., Chemistry, Xiamen University, China 1999 M.S., Chemistry, Xiamen University, China, 2002 Ph.D., Chemistry, Texas A&M University, 2008